REPORT No. 92

WAVE DRAG IN TRANSONIC AXIAL COMPRESSORS

OLUFEMI OKUROUNMU

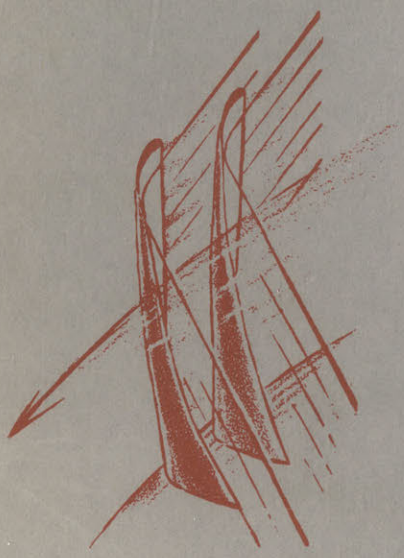

November, 1967

GAS TURBINE LABORATORY
MASSACHUSETTS INSTITUTE OF TECHNOLOGY
CAMBRIDGE, MASSACHUSETTS 02139

WAVE DRAG IN TRANSONIC AXIAL COMPRESSORS

by

OLUFEMI OKUROUNMU

Under the Sponsorship of:
General Electric Company
Allison Division of General Motors Company

GAS TURBINE LABORATORY

REPORT No. 92

November 1967

MASSACHUSETTS INSTITUTE OF TECHNOLOGY

Cambridge, Massachusetts

ABSTRACT

Profiles of fluid properties, including flow angle, static and total pressures have been obtained behind a free wheeling 8" diameter transonic rotor. The latter consists of 40 blades with double circular arc profiles, a hub to tip diameter ratio of 0.80 and a mean solidity of 0.94. The variation of stagger angle along the blade span is such that the local relative velocity is aligned with the blade chord at a design point corresponding to an inlet axial Mach number of 0.6 and a rotor speed of 35,000 RPM.

The profiles show strong evidence of the existence of standing accoustic waves in the flow passage at transonic relative Mach numbers. A strong drag rise is observed at subsonic relative Mach numbers (M_T) close to unity, the slope of the drag curve being negative at $M_T = 1$, but turning positive again shortly after $M_T = 1$. For $M_T < 1$, a remarkably good correlation is observed between the spanwise mean of the measured drag and previous 2-D pressure drag measurements on similar profiles. At low supersonic relative Mach numbers, the drag due to shocks in the blade passages appears to overshadow the wave drag, and as yet, there is no definitive way to isolate the contribution of the wave drag experimentally. Computed values of the wave drag at these speeds, based on McCune's analysis for a non-lifting blade row, are "compared" with the measured drag.

A linearized theory is presented for obtaining the induced drag of an axial compressor blade row subjected to any arbitrary blade loading distribution. The blades are replaced at their leading edges by bound vortex lines of varying strength along the span, and the induced drag obtained from the induced velocity field of the resulting trailing helical vortex sheets. Use of this lifting line approach restricts the useful range of the theory to

relative Mach numbers less than unity, since such a quasi 2-D theory would not be applicable to transonic flows which are believed to be inherently three dimensional.

ACKNOWLEDGEMENTS

The author is very grateful to the entire staff of the Gas Turbine Laboratory who have filled his years at M. I. T. with fond memories, and made his pursuit of knowledge such a memorable experience. In particular, he is heavily indebted to his thesis committee: Prof. Edward S. Taylor, whose soft words and thoughtful guidance provide fresh inspiration at moments of near desperation; Prof. James E. McCune, who energetically followed every stage of the analytical investigation and Prof. Jack L. Kerrebrock, who made significant contributions to this endeavour.

The Mechanical Design staff of the M. I. T. Instrumentation Laboratory, under the supervision of Mr. Roy Euvrard, were of invaluable assistance in the draughting and construction of the test section. Special thanks are due to Mr. Thorvald Christensen and his staff for their painstaking efforts in the construction and maintenance of parts of the experimental setup.

The author also wishes to express his gratitude to Miss Joan Kukolich who helped with the initial stages of the numerical computations, and to Mrs. Madelyn Euvrard and Miss Lotte Wiedman for careful secretarial assistance.

The numerical computations were done with the assistance of the M. I. T. Computation Centre.

TABLE OF CONTENTS

LIST OF FIGURES

NOMENCLATURE

a	Speed of sound
c	Local chord length
C_{ax}	Axial projection of blade chord
C_p	Specific heat at constant pressure
g_o	Newton's gravitational constant
$g(\xi)$	Profile shape function, proportional to blade slope at given radius
h	Hub to tip diameter ratio
h_{nk}	Expansion coefficients of the function $X_n(\rho)$ in a series of the normalised Bessel functions, R_{nB}
k	Ratio of specific heats
$\dot{m}$	Mass flow rate
n	Index of summation over tangential eigen functions
p	Special source strength distribution function
q	Source strength distribution function
r	Radius
s	Local blade spacing
(v_x, v_θ, v_r)	Velocity perturbations in axial, tangential, and radial directions
$(v_x^*, v_\theta^*, v_r^*)$	Induced velocities at the blades
w	Mass flow rate
(x, r, θ)	Rotor fixed co-ordinates
$(x_1, r_1, \theta_1, t_1)$	Space fixed co-ordinates
z	$\omega x/U$
A_{nk}	Expansion coefficients in series of velocity potential

B	Number of blades
D_1	Drag due to skin function
D_2	Pressure drag associated with viscosity
D_3	Pressure drag due to shocks
D_4	Pressure drag due to shock-boundary layer interactions
D_5	Drag associated with stagnation pressure drop across shock
D_6	Induced drag due to lift
D_7	Wave drag
F_T	Local net tangential force on rotor
F_x	Local net axial force on rotor
I_{nB}	Modified Bessel function of 1^{st} kind, of order nB
J	Mechanical equivalent of heat
J_{nB}	Bessel function of 1^{st} kind, of order nB
K_{nBk}	Radial eigen values
L	$2\pi r_T/B$ = blade spacing at the tip
M	Axial Mach number upstream of rotor
M_T	Relative Mach number at rotor tip, based on velocities far upstream of the rotor
N_{nB}	Bessel function of 2^{nd} kind, or Newmann function
P	Static pressure
P_{null}	Pressure of side hole of yaw probe in its null direction
P_o	Stagnation pressure
P_{oi}	Total pressure indicated by yaw probe

Q^*_{nk}	Characteristic coefficients depending on blade geometry
R	Recovery factor; gas constant
R_{nB}	Normalised combination of Bessel and Newmann functions
R_E	Reynolds number
T	Temperature
T_o	Stagnation temperature
U	Axial velocity far upstream of the rotor
V_B	Blade tip speed
W	Work done across rotor
W_u	Local relative velocity far upstream of rotor
W_D	Local relative velocity far downstream of rotor
W_m	Local mean relative velocity based on conditions far upstream and far downstream
X	Measured axial force on rotor
Y	Estimated net tangential force on rotor
$Y_{nB}(K_{nBk}\eta)$	Combination of Bessel and Newmann functions
α	Yaw probe calibration parameter
β	$\sqrt{1-M^2}$; 'discharge coefficient' at station 3
ξ	Co-ordinate in axial direction, measured from blade leading edge
η	r/r_T
ζ	Local blade half thickness; helical co-ordinate = $\theta - z$
τ	Thickness to chord ratio; friction torque on rotor
τ_o	Thickness to chord ratio at the hub

ρ	$\omega r/U$; fluid density
ρ_s	Dimensional radius of sonic cylinder
ω	Angular velocity of rotor
σ_∞	Fluid density far upstream of rotor
σ_n	$nB\rho$
ν	Kinematic viscosity
γ_{nk}	$\sqrt{3}\tan\delta_{nk}$
δ_{nk}	Phase shift angle of cylinder functions with respect to the Bessel functions
λ_{nk}	Axial dependence coefficients of wave functions
$\Phi_1(x_1,r_1,\theta_1,t_1)$	Perturbation velocity potential in space fixed co-ordinates
$\Phi(z,\rho,\theta)$	Perturbation velocity potential in rotor fixed co-ordinates
$\Phi(\rho)$	Local stagger angle = $\tan^{-1}\rho$
Γ	Circulation distribution function
Γ_{nk}	Expansion coefficients of the circulation in a series of the functions R_{nB}

Superscripts and Subscripts

H	Denotes conditions at hub
T	Denotes conditions at tip
∞	Refers to conditions far upstream of rotor
(1,2,3,4,5)	Denotes conditions at stations (1,2,3,4,5)
x	Denotes component in axial direction
θ	Denotes component in tangential direction
f	Frictional

WAVE DRAG IN TRANSONIC AXIAL COMPRESSORS

by

Olufemi Okurounmu

I. BACKGROUND TO THE PROBLEM

I.A Introduction

Interest in transonic axial compressors has grown in the last two decades simultaneously with the desire to build lighter weight, higher capacity turbo jet engines. One of the major factors restricting the performance of subsonic machines is the attempt to avoid high relative Mach numbers at the rotor inlet, and associated reductions in efficiency due to increased compressibility effects. Such consideration usually limits the relative Mach number to values below 0.80. The major effort in the quest for more compact, higher capacity machines has therefore been directed towards the removal of this limitation, and this has led to quite extensive studies of transonic compressors, usually defined as a compressor in which the relative Mach number at the rotor inlet varies from subsonic at the hub to supersonic at the tip. Higher relative velocities at the rotor can usually be obtained in any one of three ways: (a) by initial turning of the air counter to the rotor direction, through use of inlet guide vanes; (b) increasing the axial velocity to the rotor, or (c) increasing the rotational speed of the rotor. In practice, all of these methods are employed. Transonic axial compressors are thus characterised not only by near sonic relative Mach numbers, but also by a slightly higher mass flow per unit of frontal area. The higher Mach numbers at the rotor inlet lead to a much higher pressure rise across each stage, so that for a given overall pressure rise, fewer stages are required in the transonic compressor. With fewer stages to build, the problems of matching one stage to the next become less troublesome, and finally, the slightly higher mass

flow for a given frontal area, combined with the reduced weight, make possible the attainment of a higher thrust to weight ratio for the engine as a whole.

Conventional design procedures, whereby the flow in each elemental compressor annulus is assumed to be two dimensional, and each blade section designed on the basis of correlated 2-D cascade data have proved reasonably satisfactory in both the subsonic and supersonic cases, through use of empirical coefficients to take account of the three dimensional nature of the flow. However, the discrepancies between such simplified theoretical flows and the actual flow become more pronounced as we move into the transonic regime, demonstrating a need for a more detailed understanding of the actual flow process, if transonic compressors are to be rationally designed. One reason for such large departures from two dimensionality is the presence, in the transonic regime, of acoustic waves radiated out from the compressor blades, as has been shown by Rott.[1] These waves do not arise until the relative Mach number at the tip exceeds unity, and their appearance effectively transforms the flow field into an inherently three dimensional one, so that any realistic study of this regime of operation must be made from this point of view.

I.B Previous Experimental Work

Tests conducted on transonic compressor installations have already yielded very promising results. Lieblein, Lewis and Sandercock[2] have tested a transonic compressor inlet stage with a hub to tip diameter ratio of 0.525 and a tip diameter of 17.36." The rotor consisted of 21 blades, with double circular arc profiles, characteristic of most NACA transonic compressor tests. At the design corrected weight flow of 44.5 lbs./sec., they obtained a stage pressure rise of 1.47 and an efficiency of 90%.

Similar tests were conducted by Salvage and Felix,[3] with primary emphasis placed on increasing the specific weight flow of the machine, at no

sacrifice of efficiency or stage pressure rise. Using a rotor with a hub to tip diameter ratio of 0.35, and a tip diameter of 12", they obtained an efficiency of 0.87 and a mass weighted pressure rise of 1.293 at the design specific weight flow of 37.5 lbs./sec./ft.^{2} of frontal area. The tip speeds in the above tests were of the order of 1,000 ft./sec.

The above results show conclusively that transonic compressors can and do operate relatively efficiently and hence motivate the search for rational design methods, through a clearer understanding of the associated three dimensional flow-field. One area that is at present clouded with much uncertainty is the magnitude of the drag associated with the energy transported by the radiated acoustic waves originating from the blades in the transonic regime. This drag is often referred to as the Wave Drag, and is zero in purely subsonic flow. For a clearer understanding of the wave drag, as distinguished from other forms of drag, we may consider an airfoil in a gradually accelerating flow through air. The resistance to motion experienced by such a body consists of:

(1) the skin friction drag, due to the presence of viscosity. This part of the drag depends on the Reynolds number of the motion, being very small in comparison with other drag forces when the Reynolds number is very high (of the order of 10^6 or higher). Its existence would be felt by the body in all Mach number regimes, and its magnitude would undergo relatively little variation as the Mach number varied, for a given Reynolds number.

(2) the pressure drag associated with non-zero viscosity. It must be remembered that the pressure drag on a sphere in a potential flow is zero, although in a viscous flow, the total drag consists of both pressure drag and viscous drag. This pressure drag is, therefore, attributed to the presence of viscosity. Its existence

would be felt in all Mach number regimes, and it would similarly decrease as the Reynolds number increased, but would be relatively independent of Mach number.

(3) the pressure drag due to shocks on the surface of the body. For any finite body, there is a critical Mach number less than unity at which sonic velocity is first reached somewhere on the surface of the body. Beyond this critical Mach number regions of local supersonic flow exist on the surface of the airfoil, usually terminated by a λ shock. The presence of these shocks introduces additional pressure drag on the body, which may simply be referred to as the pressure drag due to shocks. Its magnitude is very much dependent of the Mach number, as this causes the position of the shocks to change.

(4) the pressure drag associated with shock-boundary layer interactions. This would arise if the adverse pressure gradient created by the shock is strong enough to separate the boundary layer on the body. Such a separation would thicken the wake behind the airfoil, and result in additional pressure drag.

(5) the pressure drag associated with the stagnation pressure drop across the shock. This is usually very small if the Mach number at which the shock occurs is not much greater than unity.

(6) the pressure drag due to the energy transported by the trailing vortices shed from the airfoil. This would be zero if the angle of attack were zero, or if the circulation were constant along the span of the airfoil. Otherwise, it would depend on the Mach number. This is referred to as the Induced Drag.

(7) Finally, as the airfoil passed through sonic speed into the supersonic regime, waves would originate from it and propagate to

infinity, and the energy radiated away by such waves would constitute an additional resistance to the body's motion. This resistance will be denoted by the terminology 'Wave Drag.' For easy reference, these various drag components will be subsequently referred to as D_1, D_2, $D_3 \ldots D_7$.

It is apparent from the above breakdown that if a model were placed in a high velocity fluid stream, with Reynolds number high enough so that viscous forces may be entirely neglected and at zero angle of attack, then any net drag experienced by such a body can be attributed to D_3, D_5, and D_7. Furthermore, if the Mach numbers are such that any direct losses across the shocks are negligible, then D_5 is negligible, and only D_3 and D_7 contribute to the drag. Since D_7 is limited to relative Mach numbers, (M_∞) greater than unity, it is then possible to attribute all of the drag for $M_\infty < 1$ to D_3. However, for $M_\infty > 1$, both D_3 and D_7 will make significant contributions to the total drag, and it is difficult to distinguish between these two. Hence, most drag measurements in the transonic regime have usually been concerned with the total pressure drag on the body.

Bryson[5] has made such measurements on two-dimensional biconvex circular arc profiles. Bryson's body consists of the front half of a double biconvex circular arc profile followed by straight parallel sections. The maximum thickness to chord ratio was 8.8%. The body was placed at zero angle of attack and the Reynolds number was assumed high enough to justify neglecting viscous forces. He obtained density distributions over the surface of the body, and hence, local Mach number and pressure distributions. He related such measurements at 3 low supersonic speeds to corresponding values for the front half of a 12% profile, using the transonic similarity rule. To obtain the pressure distributions over the entire profile, he calculated the distrib-

utions over the rearward half by means of a Prandtl-Meyer expansion theory, and matched these with the experimental values over the front half. By combining these results with the data of Liepmann, Ashkenas and Cole[6] for the local Mach number distributions at high subsonic speeds over a 12% biconvex circular arc profile, he was able to obtain the pressure distributions over the surface of the 12% profile throughout the transonic regime, and hence to obtain the variation of the pressure drag with Mach number in this regime. The slope of the drag curve at $M_\infty = 1.0$ was based on the assumption, justified experimentally, that near $M_\infty = 1$, $dM/dM_\infty = 0$. His results are shown in Figure 1.

Maeder and Thommen[7] have made direct measurements of the drag at transonic speeds on slender parabolic bodies of revolution with 20% maximum radius to chord ratio, suspended in a rectangular test section with longitudinally slotted top and bottom walls. Figure 2 is typical of their results. Since all the above measurements were made under two-dimensional flow conditions, the utility of applying them to transonic compressor design is questionable, as a result of the three-dimensional nature of the flow field mentioned earlier. The situation is further complicated by the fact that, in an actual compressor rotor in transonic operation, each radial section of a blade is influenced by other radial sections of the same blade, and also by adjacent blades, all of which effects are absent in a two-dimensional experimental set-up. Hence, while such two-dimensional experiments yield results which serve as a qualitative guide, useful numerical information can only be obtained from an actual transonic rotating device.

I.C Analytical Investigations

Several attempts have been made at an analytical treatment of the transonic flow field in an axial compressor, albeit under highly idealized conditions. Most of these efforts were actually directed towards the problem of the screw propeller, but the same methods are applicable, with slight

modifications, to an axial compressor blade row.

Goldstein[22], and later, Reissner[8,9] developed the theory of the screw propeller applicable when the flow amy be considered as incompressible. Reissner's approach has the advantage of easy adaptability to the axial compressor geometry. He represented the lifting effect of the blades by a periodic, saw-like distribution of source-sink singularities in the spacing between blades, thus obtaining, through appropriate choice of a source distribution function, an arbitrarily prescribable discontinuity of potential across each helical rotor wake, which is then related to the distribution of circulation along the blade span. Davidson[10] modified Reissner's analysis to take account of compressibility, dividing the field of flow into two regimes: the first regime being far downstream of the rotor where a modified Reissner potential is applicable, and the second regime being the entire compressible flow field. The solutions appropriate to the two fields were then matched at the plane of the rotor in such a way that appropriate boundary conditions are satisfied. His choice of boundary conditions were, however, inappropriate, and his solutions did not satisfy the continuity requirements necessary for a compressible flow situation.

McCune[13,14] has carried out an extended analysis of the non-lifting transonic compressor blade row--a study which has, to a very large extent, motivated the present work. His results indicate that three-dimensional effects are beneficial in regards to the wave drag, which is shown to build up gradually as the tip relative Mach number (M_T) exceeds 1.0, in contrast to results from the two-dimensional Ackeret Theory. McCune's results, however, do not include the contributions of the lift to the wave drag, a contribution which will always be present in an actual compressor blade row. His results are shown compared with Bryson's measurements in Figure 1.

The present investigation thus has as its primary objective the setting up of an actual transonic rotor and the measurement of the drag in such a de-

vice as a function of the relative tip Mach number. An attempt will also be made to extend McCune's analysis to include the effect of lift on the blade row at high subsonic relative tip Mach numbers. Since the experimental information will be compared with McCune's analysis, the major assumptions involved in that analysis, and the relevant mathematical results are summarized in Appendix A.

II. ROTOR DESIGN AND CONSTRUCTION

II.A Design Considerations

Several considerations influence the choice of blade shape for compressors designed to operate in the transonic regime. First, since the Mach number at which shocks first appear on the blades is higher for thin blades than for thick ones, the choice of blades with the minimum thickness consistent with adequate aerodynamic strength is suggested. From stress considerations, the blade requires more thickness at the root than at the tip, suggesting some form of a radially decreasing thickness distribution. For analytical convenience, the thickness distribution used in the present investigation has the form:

$$\frac{\tau(\rho)}{\tau_0} = \frac{\rho_H\sqrt{\rho_H^2+1}}{\rho\sqrt{\rho^2+1}} \qquad (2\cdot1)$$

where $\tau(\rho)$ is the thickness to chord ratio at radius ρ

τ_0 = thickness to chord ratio at the hub

and ρ = dimensionless radius = $\frac{\omega r}{U}$

ω = angular velocity of rotor

U = axial velocity of air

r = radius.

This function gives, at the design point, a thickness which varies almost linearly from hub to tip. A thickness to chord ratio of 0.20 at the hub was chosen from structural considerations.

Earlier tests by NACA[19] involving various blade types for use in transonic compressor testing have led to the conclusion that for M_T not exceeding about 1.2 at the tip, the double circular arc profile gave optimum performance. However, the analytical study on which the present investigation is based utilized double parabolic arc profiles, and for purposes of comparison, it would be desirable to employ profiles which are as close as possible to the analytical model. These parabolic profiles have the form:

$$\zeta(\xi) = 2(\xi - \xi^2/C_{ax}) \qquad (2\cdot2)$$

where $\zeta(\xi)$ = blade half thickness at station ξ.

ξ = axial distance measured from blade leading edge

C_{ax} = acial projection of blade chord.

It was thus necessary to make a compromise between the two choices by laying out the appropriate parabolic profiles at each radius, and approximating them with circular arcs of known radii. The geometry of the blade at any radius is thus completely specified by specifying the radius of the circular arc which comprises the surface.

To keep the entire installation within a reasonable size, a tip diameter of 8 inches was selected. Other relevant design assumptions and consequent design parameters are listed below:

(1) Hub-tip ratio, h, = 0.80

(2) A design operating point with

ω = 35,000 RPM

M = 0.60

(3) At the design point, the relative velocity is aligned with the chordwise direction at each spanwise position.

(4) The projection of the chord in the axial direction is constant at each radius.

(5) Number of blades = 40

(6) Blade disc thickness = C_{ax} = 0.35 inches

(7) Solidity at hub = .97,

(8) Solidity at tip = .91 Where solidity is defined as:

$$\text{Solidity} = \frac{C}{S}$$

and C = local chord length

S = local blade spacing.

The distributions of thickness, stagger angle and chord length, together with the radii of the circular arcs comprising the blade surface, are shown in Figure 3. For purposes of actual construction, these curves have been

replaced by straight lines passing through the end points. The finished blade is twisted from root to tip.

II.B Rotor Construction

Because of the small size of the rotor, the large number of blades, and the high rotational speed, it was extremely difficult to securely fasten each individual blade to the rim of the rotor disc. To avoid this problem, it was decided to manufacture the entire rotor as one integral piece.

Since the blade surface at any spanwise position is a circular arc, the radius of the circular arc depending on the spanwise location, it is apparent that the entire half-surface of a blade is part of the surface of a cone whose axis is inclined to the disc. The design problem, therefore, reduces to finding the exact geometrical and spatial relationship between the axis of the cone and the plane of the disc in order to produce the desired blade shape. This is done in three steps, as described below:

In Step 1, (Fig. 4a) the blade profiles at hub and tip are shown, and the line (C_1' C_2') joining the centres of the two arcs is the projection of the cone axis in the plane containing the rim of the rotor. The perpendicular (D D') to this line through the centre 0 of the profiles identifies the mid-plane about which the blade surfaces will be described in order to obtain the required twist from root to tip. Let D D' make the angle α_1 with the rotor edge.

In Step 2 (Fig. 4b), the plane D D' is shown, as well as the views of a blade surface parallel and perpendicular to it. From the perpendicular view, the half thickness of the blade is displayed, and by laying out A C_1 and B C_2 equal, respectively, to the radii of the circular arcs at the tip and root, the inclination of the cone axis C_1 C_2 to the blade midplane (0 - 0) is determined. Let this angle be α_2. The distance X from the edge of the rotor rim to the intersection of the cone axis with the blade mid-plane pro-

duced can then also be determined. The cutter surface is in this configuration assumed to lie along the surface A B, so that the angle α_3 between A B produced and C_1 C_2 gives the inclination of the cutter axis with the cone axis. The angles α_1, α_2 completely fix the geometrical relationship between the disc and the cone axis, while the distance X also fixes the spatial relationship. The angle α_3 determines the geometrical relationship between the cutter axis and the cone axis. The cutter is, of course, free to move back and forth along its axis. Since the cone axis has been used mainly as a reference direction, it may, for convenience, be taken as the vertical direction.

In Step 3 (Fig. 4c) the angles and distance specified in Steps 1 and 2 are used to set up a practical cutting arrangement. The arrangement consists of a rotary table, a dividing head, and two cross-slides, all mounted on a milling machine. The cone axis is taken to be vertical and to pass through the centre of the rotary table. The angles α_1 and α_2 are compounded into two equivalent angles β_1 and β_2, one of which specifies the inclination of the dividing head axis, while the other gives the angle which the horizontal projection of this axis makes with a reference horizontal line in the vertical plane containing the cutter axis. First, the dividing head axis is turned through the angle β_1, and the entire set-up next rotated through β_2 by means of the rotary table. The cutter is set at the angle α_3 to the vertical, and the blade surface is generated by oscillating the table about its axis while feeding the cutter along its axis. However, before this last rotation, the table axis and cone axis must coincide, and this is brought about by use of two cross-slides mounted on each other parallel and perpendicular to the horizontal projection of the cutter axis. By turning on appropriate off-sets on each of these cross-slides, the table axis and cone axis can be brought into coincidence, and the blade surface generated. The set-up is shown in Figure 5. The finished rotor is shown in Figure 6.

III. APPARATUS AND EXPERIMENTAL TECHNIQUE

III.A The Test Section

A schematic of the test section is shown in Figure 7. It consists of an overhung 0.3938" Diam. shaft mounted vertically on two Fafnir ABEC 5 specification ball bearings. The rotor is mounted at the overhanging end. The two bearings are separated by means of spacers, the upper one resting on the shaft shoulder while the lower one is clamped in position with a locknut. The bearings are lubricated by continuous oil circulation. An oil burner pump, with a capacity of 3 gals./hr., and driven by a 1/3 HP motor delivers the oil at about 60 psi. This oil is then converted to a partly mistified jet as it emerges through a .01" diam. orifice located a short distance below the upper bearing, so that this jet is directly squirted upwards to provide upper bearing lubrication. Since the installation is vertical, the oil from the upper bearing descends by gravity through the clearance between the inner and outer spacers, and provides adequate lubrication for the lower bearing. A slinger is mounted between the top bearing and its supporting shoulder in order to return any oil escaping upwards above the bearing to the oil reservoir, through ports in the bearing housing. The reservoir is lcoated directly below the bearing installation. Nevertheless, in spite of the slinger provision, some oil was noticed to escape through the narrow clearance between the shaft and the upper bearing support plate. To eliminate this, an additional plate was interposed between this plate and the rotor, in order to shield the escaping oil from the centrifugal field of the rotor and thus enable it to drop back into the reservoir through ports in the lower plate. This plate proved very effective.

An important feature of the installation is the provision of an automatic dampening mechanism in the case of excessive vibrations being encountered during operation. This is provided by having above the top bearing

support plate, a second plate with a larger inner diameter and resting on a shoulder of the former in such a way that the top surfaces of both plates are roughly flush with each other. The top plate is attached at its rims to the inner casing, and the lateral clearance between the inner diameter of the top plate and the outer diameter of the shoulder of the lower plate is adjusted to be a little less than the diametrical tip clearance of the rotor blades. In this manner, any excessive vibrations of the bearings, and hence of the lower plate, are dampened through its rubbing action with the upper plate. Moreover, should large vibrations ever occur, the upper plate limits the lateral amplitude of these vibrations, so that the blades cannot hit the outer casing.

The shaft is threaded at its lower end to support a steel disc permanet magnet directly below which two blocks of copper windings in series are supported. Each block consists of about 2,000 turns wound on insulating material. The air gap between the windings and the magnet is of the order of .005".

The bearing installation is secured internally to an inner casing which is itself fastened to the outer casing by means of three stream-lined supporting struts, spaced 120° apart circumferentially. These struts are provided with suitable ports through which leads and lubricating tubes are passed.

Directly above the rotor, there is a cone-like inlet, terminating in a 2-1/2" long cylindrical section. This inlet is designed to provide a gradually converging passage to the incoming flow, thus ensuring uniformity of the flow immediately upstream of the blades. The inlet is supported by two sets of streamlined struts: four horizontal ones spaced 90° apart circumferentially, and four inclined ones similarly spaced. The horizontal and inclined ones are staggered with respect to each other. Each of these struts is screwed to the inlet cone at one end and provided with adjustable tightening screws at the free end. By proper manipulation of the adjusting screws, the inlet cone can be properly aligned in the vertical direction, and its

height above the blades can also be adjusted within small limits. In its final assembled position, the axial clearance between the lower surface of the inlet cone and the rotor is about 0.025" while the radial tip clearance of the rotor is of the order of 0.030 to 0.040".

III.B Complete Installation

The test section, as described above, is incorporated into a closed circuit wind-tunnel, as shown in Figure 8a. The air for the tunnel is circulated by means of a 5-stage centrifugal compressor, driven by a variable speed DC motor connected by a 5:1 step-up helical gear to the compressor shaft through a flexible coupling. The compressor has a capacity of up to 15,000 cu ft/min of air at about 5,000 RPM, when sucking air at about 5 psia and 90°F. The pressure ratio under these conditions is about 3. The ambient pressure in the tunnel can be raised by means of an auxiliary compressor or lowered by means of steam ejectors connected to the tunnel passages. The outer casing of the test section has an internal diameter of 8.125", and is joined above to a 12" I.D. inlet pipe by means of a smooth contraction. Ahead of the contraction is a cloth filter to remove any dust particles from the air stream. A 6" long 12" diam. honeycomb section is placed in the settling chamber upstream of the contraction. It is hoped that this will remove any swirl in the approaching flow. A number of radiators at the compressor discharge, some of which may be turned on or off if desired, permit a limited amount of control of the air temperature.

It is apparent that since the rotor is undriven, the sole driving force is the momentum of the tunnel air. Speed variations in the rotor are obtained by varying the pressure ratio across the rotor thus varying the mass flow of air in the tunnel.

III.C Measuring Stations

Five measuring stations are shown in Figure 7. Station 1 is immediately

after the contraction, about 14.25" upstream of the rotor leading edge. Conditions at this station are taken to be representative of conditions at infinity in the upstream direction. Station 2 is 0.46" upstream of the rotor leading edge, while Station 3 is 0.48" downstream of the rotor trailing edge. Stations 4 and 5 are two more stations located about 2" and 4" respectively, downstream of Station 3.

III.D Instrumentation and Measuring Technique

1. Measurements Without the Rotor-Pitot Tube Measurements

Preliminary measurements were made at several stations without the rotor to survey the flow conditions, in order to provide a ready reference for, and also serve as a basis of interpretation of later measurements made with the rotor mounted. For these 'no-rotor' measurements, a dummy disc of diameter equal to the hub diameter of the rotor was substituted for the rotor.

At Station 1, the total and static pressure distributions were obtained using the larger Pitot-Static tube shown in Figure 9. As can be seen in Figure 10a, the total pressure at this station is uniform withing 0.5% of the centre-line total pressure. Hence, in all subsequent measurements with the rotor, it was sufficient to measure the centre-line total pressure. The total temperature was assumed uniform at Station 1, while both the total temperature and pressure were assumed to vary negligibly between Stations 1 and 2.

Four static pressure holes, stationed 90° apart circumferentially, were located on the outer wall at Station 2, and on both the inner and outer walls at Station 3. Preliminary measurements, however, indicated no perceptible variations of the pressures in the tangential direction, and hence subsequent measurements were limited to only one pressure tap at each wall.

The total and static pressure distributions at Station 2 are shown in Figures 10b and 10c. These measurements were taken with the smaller pitot-

static tube shown in Figure 9. They reveal that the flow at this station is uniform up to about 0.05" from the walls, and that the static pressure is uniform throughout the annulus. The same pitot-static tube used above was used to measure the profiles at Stations 4 and 5. The static and total pressures at Station 4 are plotted in Figures 10f and 10g. Unlike at Station 2, an appreciable boundary layer development has occurred on the outer wall. The lack of symmetry in the boundary layers on the annulus walls is probably due to the disturbance effect of the clearance between the inlet cone and the dummy rotor which helps to trip the boundary layer fluid on the inner wall, causing it to become turbulent, while that on the outer wall remains laminar. At Station 5, the boundary layers are virtually fully developed, as seen in Figures 10h and 10i. The same pitot-tube could not be used to traverse the flow at Station 3, since that would place the static pressure holes close to the clearance between the inlet cone and the downstream section, and thus cause faulty readings of the static pressure. The traverse at this station was made with a 3-hole yaw probe.

2. Measurements Without the Rotor-Yaw Probe Measurements

At Station 3, provision was made for a radial traverse with a three-hole yaw probe, shown in Figure 11. Because of the small dimensions of the passage in which the traverse was to be made, the diameter of the probe had to be kept very small (0.125"), and in order to be able to traverse as much of the annulus as possible, the static and total pressure holes were placed a bare 0.030" or 1/4 diameter behind the tip of the probe instead of the conventional 2 diameters or more in commercial probes. The net effect of this is to reduce the insensitivity of the probe to pitch, and in particular, to make it read slightly less than the true total pressure at zero pitch. This defect was, however, corrected for by initial calibration, shown in Figure 12a, in which it may be seen that at zero pitch, the indicated total

pressure is less than the true total pressure by about 4% of the difference between the total pressure and static pressure. Figure 12b shows the direction sensitivity of the probe, while Figure 12c shows the dependence of the indicated total pressure on yaw angle. Thus, ideally, the probe will yield the flow direction to within an accuracy of less than 1/8°, the indicated total pressure being independent of Mach number throughout the Mach number range of interest. The calibrations in Figures 12b and 12c were both obtained under no rotor conditions. Since it was also desired to measure the fluid static pressure with the yaw probe, a calibration was made to relate the pressure on the side holes at the null condition to the fluid static and total pressures. This calibration was put in the form

$$\frac{P_{null} - P_{\infty}}{P_{oi} - P_{\infty}} = \alpha(r, M) \qquad (3.1)$$

where P_{null} = side hole pressure at null condition

P_{∞} = stream static pressure

P_{oi} = total pressure indicated by yaw probe.

For this calibration, use was made of the uniformity of the static pressure at Station 2, since it was then possible to assume that P_{∞} was known, being the same as the wall static pressure. By traversing the probe at this station, measuring P_{null} and P_{oi} at each radial position for different free stream Mach numbers, a calibration curve of $\alpha(r, M)$ was obtained. This is shown in Figure 12d. It can be seen from this curve that α is independent of M, within the relevant range of M, but depends markedly on the radial position. This should be expected, since the pressure coefficient at the hole location would depend on the streamline geometry around the probe, and hence on its radial position.

Using this calibration, the yaw probe was used at Station 3 to measure the static and total pressure distribution. These are shown in Figures 10e

and 10d. The static pressure at Station 3, as obtained from this calibration is correct to within ±3% of the dynamic head.

3. Measurements with the Rotor

With the dummy rotor now replaced by the actual rotor, sets of measurements were made with a view to obtaining drag information at various relative tip Mach numbers. The ambient pressure in the tunnel for most of the runs was of the order of 10psia. The pressure measuring and recording system included a ±1psi differential pressure transducer, two ±2 psi differential pressure transducers, a ±15 psi differential pressure transducer, a mechanical multichannel pressure selecting device, a Sanborn DC amplifier, an X-Y recorder and an AC powered multichannel transducer amplifier-indicator.

The total and static pressures at Station 1, the wall static pressures at Stations 2 and 3, and the total and static pressures at Station 5 were each connected through manometer tubings to separate input arms of the pressure selecting switch, the output arm of which was connected to one port of the 15psi transducer. The signal from the transducer was applied to one channel of the multichannel transducer amplifier indicator, where it was amplified and visually displayed in millivolts. The other port of the transducer was exposed to the atmosphere.

The total pressure at Station 3 was measured with reference to that at Station 1. This was done by connecting the two pressures to opposite ports of one of the 2psi differential pressure transducers, and connecting the signal from the transducer to one channel of the amplifier-indicator to be amplified and displayed.

The yaw probe was traversed at Station 3, and at each radial position, it was yawed until the pressure difference between the two side holes was zero. This pressure difference was measured by connecting the pressure at the side holes to opposite ports of the 1 psi differential transducer, the

signal from which was amplified and displayed through a separate channel of the transducer amplifier-indicator. When the meter indicates that a null position has been reached, the flow angle is indicated directly on a protractor by means of a pointer which rotates with the probe. The zero flow angle is that which corresponds to the 'no rotor' conditions, and the flow angle is regarded as positive when it is in the direction of rotor rotation. In the null position of the yaw probe, the pressure from one of the side holes is led to one port of the other 2 psi-differential transducer, while the wall pressure at Station 3 is led to the other port. The signal from this transducer is amplified by a Sanborn DC amplifier, and the output is used to drive the Y arm of an X-Y recorder. The X arm is driven from a time base voltage. The total pressure is also read in this null position, as previously described. The use of differential pressure transducers with small over-all range made it possible to obtain a higher resolution than would otherwise be possible.

The total temperature at Station 1 was measured with a mercury thermometer, while an Iron-Constantan thermocouple, with its reference junction at 32°F was used to obtain the total temperature at Station 5. In order to measure the rotational speed of the rotor, the leads from the pick-up coils were connected to a Hewlett-Packard electronic pulse counter which was set to read directly in revolutions per second. Most of the equipment described above are shown in Figure 8c.

Since the probe had to be yawed at each radial position, it was not possible to employ a mechanical drive, and a complete set of readings necessarily took of the order of 10 to 15 minutes. It was

therefore essential that steady state conditions should prevail throughout most of a run. The criterion of steadiness employed was to compare the total pressure at Station 1 at the beginning and at the end of a run, and also to check the constancy of the rotor speed. In all of the runs reported, the rotor speed did not vary by more than 1% during a run, while the maximum variation in total pressure did not exceed 1/2%.

III.E Data Reduction Procedure

1. Mathematical Equations

In reducing the measured data, it was necessary to assume a frictionless isentropic flow and, thereafter, to make suitable corrections for any observed departures from this idealised condition. A typical calculation proceeded as follows:

$$M_2 = \sqrt{\frac{2}{k-1}\left[\left(\frac{P_{01}}{P_2}\right)^{\frac{k-1}{k}} - 1\right]} \qquad (3.2)$$

$$T_2 = \frac{T_{01}}{1 + \frac{k-1}{2} M_2^2} \qquad (3.3)$$

$$U_2 = 49.02\sqrt{T_2} \cdot M_2 \qquad (3.4)$$

$$V_B = \omega r_T$$

$$M_T = \frac{\sqrt{U_2^2 + V_B^2}}{49.02\sqrt{T_2}} \qquad (3.5)$$

$$R_E = \frac{U_2 r_T}{\nu(T_2)} \qquad (3.6)$$

$$\rho_2 = \frac{P_2}{RT_2} \qquad (3.7)$$

$$W_2 = \rho_2 U_2 A_2 \tag{3.8}$$

$$P_3(r) = \frac{P_{null}(r) - \alpha P_{o3i}(r)}{1 - \alpha(r)} \tag{3.9}$$

$$\frac{P_{o3i} - P_3}{P_{o3} - P_3} = 0.96 \tag{3.10}$$

$$M_3(r) = \sqrt{\frac{2}{k-1}\left[\left(\frac{P_{o3}}{P_3}\right)^{\frac{k-1}{k}} - 1\right]} \tag{3.11}$$

$$T_3(r) = \frac{T_{o5}}{1 + \frac{k-1}{2} M_3^2(r)} \tag{3.12}$$

$$U_3(r) = 49.02 \sqrt{T_3(r)} \cdot M_3 \tag{3.13}$$

$$U_{3x} = U_3 \cos \theta \tag{3.14}$$

$$U_{3\theta} = U_3 \sin \theta \tag{3.15}$$

$$\rho_3(r) = \frac{P_3(r)}{RT_3} \tag{3.16}$$

$$W_3 = 2\pi \int_{r_H}^{r_T} \rho_3 U_{3x} r dr \tag{3.17}$$

2. Correction for Frictional Effects

A look at Figures 10 shows that the boundary layers on the annulus walls are thin at Stations 1 and 2; so that, to a first approximation, frictional effects at these Stations may be neglected, and the flow properties, in particular the mass flow at Station 2, may be calculated on the basis of the isentropic relations. At Station 3, however, there is a substantial boundary layer on the outer wall,

and we may rightfully expect that the calculated mass flow at this Station, based on the isentropic relations, will be in excess of the true mass flow. This suggests the use of a blockage factor at Station 3, if the integrated mass flow at this Station is to be checked against the mass flow upstream. For a quantitative estimate of this blockage factor, use was made of the static and total pressure distributions at the Station under 'no rotor' conditions. From these curves, the mass flow that would be obtained if the total pressure at the Station were uniform and equal to the free stream total pressure can be calculated, and compared to the mass flow according to the actual total and static pressure distributions. The ratio of these two quantities may then be used as a kind of 'discharge coefficient' applicable to the section. This process is illustrated in Figure 13. Equation (3.17) must therefore be modified to read:

$$W_3 = 2\pi\beta \int_{r_H}^{r_T} \rho_3 U_{3x} r dr \qquad (3.17a)$$

The factor β is approximately 0.97.

3. Determination of $T_{o3}(r)$

Equation (3.12) assumes that the total temperature at Station 3 at every radius is the same as the wall temperature at Station 5. This is at least only a rough approximation, for two reasons: First, a uniform total temperature at Station 3 would imply equal work done across the rotor at each radius, since the total temperature upstream is uniform. Such a situation is not borne out by experimental data. Secondly, if we neglect heat transfer to or from the walls, then the

wall temperature T_{o5} is the adiabatic wall temperature, which is related to the mean total temperature, T_o, at the Station through the expression:

$$\frac{T_{aw}}{T_o} = \frac{1 + R(\frac{k-1}{2} M^2)}{1 + \frac{k-1}{2} M^2} \qquad (3.18)$$

where R is the recovery factor.

At low Mach numbers, $T_{aw} \simeq T_o$. Hence, at a place such as Station 1, where the Mach number is very low, the wall temperature is truly the mean total temperature. However, at Station 5, where M is quite high, the adiabatic wall temperature will be lower than the mean total temperature. Equation (3.12) must therefore be corrected. To do this, we perform an iteration in which, as a first approximation, we assume (3.12) to be true, i.e. the total temperature at Station 3 is uniform and equal to T_{o5}. Values of $U_{3\theta}$ are then calculated as before. Next, Euler's turbine equation is used between Stations 2 and 3, namely:

$$g_o J C_p [T_{o3}(r) - T_{o2}] = \omega r U_{3\theta}(r) \qquad (3.19)$$

Values of $T_{o3}(r)$ obtained from (3.19) are then used in (3.12) instead of T_{o5}, and $U_{3\theta}$ is recalculated. Only one iteration is necessary to obtain convergence.

A check on the accuracy of the measurements may be made by a comparison of the calculated mass flows at Stations 2 and 3. The two values were found to agree within ±3% as illustrated in Figure 14.

4. Axial Force on Rotor

If an annular control volume is taken surrounding the rotor blade, and extending from the upstream to the downstream measuring Station,

the momentum balance may be expressed as:

$$-X + P_2\pi(r_T^2-r_H^2) - 2\pi\int_{r_H}^{r_T} P_3(r)rdr = 2\pi\int_{r_H}^{r_T} \rho_3 U_{3x}^2 rdr - \rho_2 U_2^2\pi(r_T^2-r_H^2)$$

$$\text{or}\quad \frac{X}{\frac{\rho_2 U_2^2}{2}\pi r_T^2} \equiv C_X = \frac{4P_2}{\rho_2 U_2^2}\int_h^1 \left[\frac{P_2-P_3(r)}{P_2}\right]\eta d\eta + 4\int_h^1 \left[1-\frac{\rho_3}{\rho_2}\frac{U_{3x}^2}{U_2^2}\right]\eta d\eta \qquad (3.20)$$

where X = net axial force on the blade

$\eta = r/r_T$

$h = r_H/r_T$

5. The Drag Force

Figure (i) shows the relative velocity vectors upstream and downstream of the blade row, as well as the mean relative velocity vector. The lift vector is perpendicular to the latter, while the drag is parallel to it. The vector sum of the drag force and the lift force must, however, have no tangential component, assuming the net tangential torque on the rotor is zero. (This assumption will be shown later to be true.) Hence, this vector sum must be axial, and is the force denoted by X.

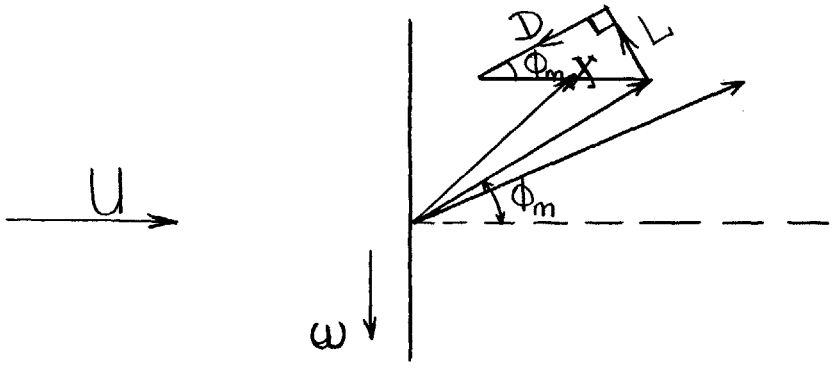

Figure (i)

Thus, $D = X \cos \phi_m$

and the drag coefficient, C_D is given by

$$C_D = C_X \cos \phi_m \tag{3.21}$$

$\cos \phi_m$ is approximately 0.56, if we assume the mean relative velocity direction to coincide with that of the blade chord at mid-span

IV. EXPERIMENTAL RESULTS AND DISCUSSION

IV.A Tangential Velocity Profiles

Fig. 15a illustrates the distribution of tangential velocities for various selected values of relative blade tip Mach numbers. The turning angle across the rotor varies almost sinusoidally with radius. This could have been expected, since, in the absence of any appreciable net torque on the rotor, the net work done by the fluid on the rotor is zero, and hence, the fluid undergoes no net turning across the rotor. It will be shown subsequently, by consideration of the disc friction and the bearing friction, that the net torque on the rotor is indeed negligible.

At the lower relative Mach numbers, the innermost section of the root is compressing the fluid, although immediately neighbouring sections are expanding it. The tip on the other hand is expanding the fluid at these Mach numbers. As the Mach number increases, the tip section acts more and more as a compressor, while the root acts correspondingly as a turbine. Thus, although the total lift on the blade may be zero, there is a change of circulation along the blade, giving rise to a net induced drag on the rotor. The magnitude of this induced will be estimated in a subsequent section.

The performance of each blade section as the Mach number varies is best seen from Fig. 15b. This plot may also be interpreted as showing the amount of turning of a fluid particle at each radius, since U_2 is constant with radius, and U_θ is proportional to $\sin\theta \approx \theta$. It is significant here that the turning at each radius is approximately constant below a tip Mach number of about 0.90. In this range of Mach numbers, very little work is done at any radial section. The section near $r/r_T = \eta = .804$ is slightly compressing, but the radial extent of this compression region is very small, and the entire section between $\eta = .810$ and $\eta = .853$ is an expansion region. Between $\eta = .853$ and $\eta = 1.0$, the sections are either expanding the fluid slightly, or doing relatively little work.

Beyond a tip Mach number of about 0.90, there occurs a sudden increase in the turning at all sections, particularly near the root. Between $M_T = 0.90$ and 1.0, the root sections are actively expanding the fluid, while sections at $\eta = .853$ and higher are compressing it. At $\eta = .853$, the section is doing no work at all, regardless of the tip Mach number. As M_T increases above unity, the expansion at the root becomes less intense, and the magnitude of the turning angle gradually decreases. Simultaneously, the compression near the tip sections increase, giving rise to still higher turning angles.

The sudden increase in the fluid turning angles above $M_T = 0.90$ is evidence of an increase in circulation around the blades, and may thus be expected to result in higher induced drag on the rotor. These large turning angles are probably indicative of the existence of shocks in the blade passages, and of separation of the boundary layer. A three-dimensional plot of the tangential velocity profiles is shown in Fig. 15c.

IV.B Work Done and Total Temperature Rise

In section III.E-5, it was stated that the net tangential torque on the rotor is zero, and on this basis, the drag force was related to the net axial force on the rotor. We shall consider this statement further.

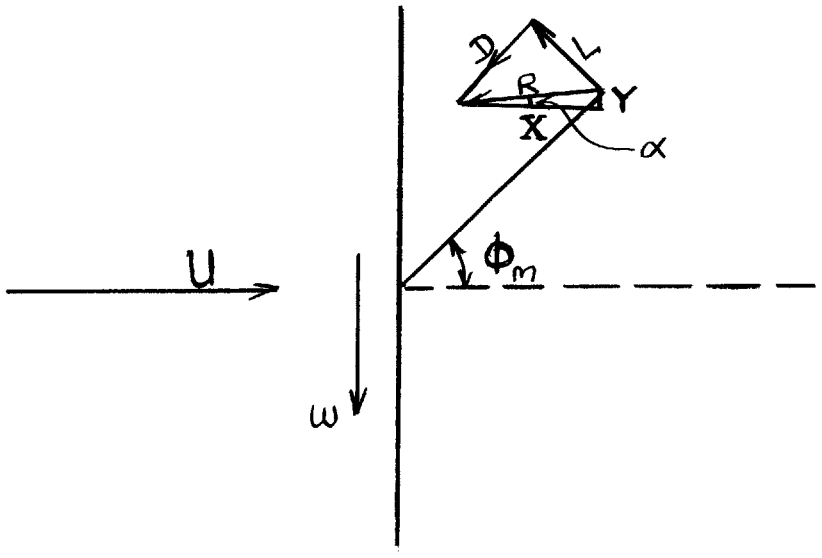

Figure (ii)

In Fig. (ii), ϕ_m is the spanwise mean of the relative velocity directions. L is the lift force, and D the drag force, both having a resultant R which has components X and Y in the axial and tangential directions respectively. α is the angle which this resultant makes with the axial direction. From the figure,

$$\tan \alpha = Y/X \tag{4.1}$$

X is the measured axial force on the rotor, and Y consists of the resistance to the rotor due to disc friction and bearing friction. The magnitudes of these will be estimated independently. We consider first the disc friction force.

In estimating the disc friction torque, use was made of an expression proposed by Ippen[25] for the fluid friction on a thin disc running in a casing, which has the form

$$\tau_f = \frac{0.0418}{(RE_D)^{1/5}} \frac{\rho r_2^3 u_o^2}{2g_o} \tag{4.2}$$

where τ_f = friction torque on one side of disc

RE_D = disc Reynolds number = $\omega r_o^2 \rho / \mu g_o$

ρ = fluid density

r_o = outer diameter of disc

u_o = peripheral speed of disc

At the maximum value of rotor speed encountered during the tests, this torque comes to about .06 ft.lb_f; equivalent to a force of 0.2 lb_f applied to the disc at mid-span.

Next,we consider the bearing torque on the rotor, which was estimated by assuming a radial load on the bearing of about 50 lbs at 30,000 RPM. In addition, a coefficient of friction of 0.001 between the balls and the moving inner race was assumed. The torque under these conditions is about 0.003 ft.lb_f,

which may be imagined as due to a force of 0.01 lb_f acting at the mid-span of the rotor. Thus, adding up the combined resistance of the disc friction and bearing friction, we have:

$$Y = 0.21 \quad lb_f \tag{4.3}$$

The axial force X, as measured experimentally under the same conditions as the above is given by:

$$X = C_x \frac{\rho_2 U_2^2}{2} \pi r_T^2 = 26 \; lb_f \tag{4.4}$$

Thus, $\tan \alpha \approx .0081$

and the angle α is less than 1/2 a degree. We may therefore neglect the force Y, and assume that the resultant of L and D is in the axial direction. This assumption is equivalent to there being no net torque on the rotor, and hence, we may expect that the net work done on the fluid by the rotor is also approximately zero.

The total temperature distribution downstream of the blade row is shown in Fig. 16. From these, it is now possible to calculate the total work done by the blades from the relation:

$$W_{3-2} = 2\pi r_T^2 \beta \int_h^1 (\rho_3 U_{3x} C_p T_{o3} \eta) \, d\eta - \dot{m} C_p T_{o2} \tag{4.5}$$

where β is a discharge coefficient, mentioned earlier,

$\dot{m}$ is the mass flow upstream of the rotor, and

W_{3-2} is the work done by the rotor on the fluid between stations 2 and 3.

This is plotted in Fig. 17. It is apparent here that W_{3-2} is very nearly zero, within the limits of accuracy of the data. From Fig. 16, it is seen that the amount of total temperature rise or fall is in all cases less than

5° except at M_T = 1.11, where a rise of 10° occurs near the blade tips. This clearly demonstrates the extent of the compression near the tips at high relative Mach numbers.

IV.C Total Pressure Profiles

The total pressure distributions behind the blade row are shown in Fig. 18. They may be classified into two distinct categories.

For $M_T \leq .92$, the losses are relatively low, and do not vary appreciably with Mach number. The highest losses occur near the mid-span, closer to the inner half of the annulus. The extreme tip region also appears to have very high losses, most probably due to tip clearance effects associated with shed vorticity and secondary circulation of the fluid within the clearances. For $M_T < .92$, the root section is a relatively low-loss region. However, at M_T = 0.92, the losses at the root become greater, and it is probable that since the blades are thickest at the root, shocks are appearing near the blade roots at this Mach number and interacting with the boundary layer there, causing it to separate.

Between M_T = 0.92 and M_T = 0.99, there is an enormous increase in the total pressure loss everywhere in the annulus. In this Mach number range, and throughout the transonic regime, it is believed that shocks have appeared within the blade passages, creating regions of local adverse pressure gradients. In general the Mach numbers at which these shocks occur are only slightly greater than unity, so that the direct loss attributable to the stagnation pressure change across the shocks is negligible. In all subsequent discussions, it will be assumed that its contribution to the drag, namely D_5 is negligible. However, as disdussed in the introduction, the existence of these shocks in the flow passages results in such a Mach number distribution over the blades as to lead to increased drag, namely D_3. In addition, the possibility exists that the boundary layer may separate from the blades due to the presence of the shocks,

so that D_4 may also be significant in this regime. Also, the increased turning of the fluid associated with this regime leads to increased circulation around the blades, and hence might be expected to result in increased induced drag.

A second important feature of this regime is the wave-like pattern of the total pressure distribution across the annulus. This is suggestive of standing accoustic waves in the annulus, reinforcing the contention that the flow in the transonic regime is primarily three-dimensional. The wave-like pattern becomes more pronounced at the higher transonic relative Mach numbers.

IV.D Static Pressure Profiles

The static pressure distributions, shown in Fig. 19, divide once again into two classes. For $M_T < .92$, the distribution is roughly parabolic, having a minimum near the middle of the annulus. Beyond $M_T = 0.99$, this roughly parabolic profile begins to acquire a wave-like character, which, as we have seen, is characteristic of the transonic regime. The wave-like nature of the profile becomes more pronounced at the higher transonic Mach numbers.

These profiles also illustrate the increasing significance of the radial velocity components as we move into the transonic regime. It is apparent from the form of the profile at, for example, $M_T = .92$, that a fluid particle near the root section is experiencing an outward pull both from the pressure gradient and the centrifugal force. It must therefore move outwards to a higher radius until it experiences a sufficiently positive pressure gradient to balance the centrifugal force. Thus, we would expect an outward displacement of the streamlines to higher radii as the fluid passes through the rotor. This simple picture of the flow would be adequate until M_T reaches about 0.99 and then, the wave-like nature of the profile would be expected to make the exact flow picture rather complicated

IV.E Axial Velocity Profiles

Fig. 20 illustrates the distribution of axial velocity across the flow annulus. For relative Mach numbers below about 0.92, the change in axial velocity across the rotor is of the order of 5 to 10% of the upstream axial velocity. This seems to increase rapidly, however, as M_T approaches unity. At $M_T = 1.0$, there is a change of from 20 to 30% above the upstream value, while at $M_T = 1.11$, the change is as much as 40%. These large increases in axial velocity downstream of the rotor are believed due to a choking of the blade passages, as will be described in a later section.

For $M_T \leq 0.92$, namely, the primarily subsonic regime, higher axial velocities seem to occur at the larger radii, even if we ignore the sections close to the walls, where boundary layer effects might make the calculated velocity unreliable. This tendency is consistent with the radial displacement of the streamlines, mentioned earlier in connection with the static pressure distributions. At higher Mach numbers, however, the radial variation of the axial velocity takes on the characteristic wave-like pattern, expected of the transonic regime.

IV.F Choking of the Rotor Passages

In the course of the experiments, it was found exceedingly difficult to exceed a tip relative Mach number of about 1.1, corresponding to about 510 revolutions per second. Any further lowering of the back pressure downstream of the rotor resulted in little or no increase in rotor speed. Even appreciable ambient fluid density changes failed to produce any significant change in rotor speed at this point. It is believed that at this operating point, both the rotor passages and the flow annulus are choked.

Fig. 21 shows the variation of the rotor tip speed as the axial velocity of the entering air is varied. The variation is roughly linear until the choking condition is reached. In Fig. 22, the rotor tip speed is plotted against the static pressure ratio across the rotor. It is

apparent here that beyond a pressure ratio of about 1.4, substantial increases in the pressure ratio produce very little change in the rotor speed. The axial Mach number upstream of the rotor is shown on the same plot, and is seen to reach a limiting value of about 0.48 at a pressure ratio of about 1.2. At this pressure ratio, it is believed that the blade passages become choked. The choking process may thus be divided into 3 distinct stages:

In the first stage, the blade passages are not choked; the rotor speed is linear with the axial velocity, and only very small changes in the pressure ratio across the rotor are required to cause appreciable changes in rotor speed. These conditions prevail until a pressure ratio of about 1.2 is reached, at which point the blade passages become choked. The relative tip Mach number at which this happens was estimated geometrically, and was found to be approximately $M_T = 0.92$. This was done by laying out the blade passage geometrically and measuring the blade passage inlet width as well as the minimum passage width. Let these be denoted by A_i and A_m respectively. Then, corresponding to each relative Mach number at any given radial location, the corresponding A_i/A^* may be obtained from the isentropic tables, where A^* is the minimum passage area for non-choked flow. Thus, A^* may be evaluated. The area ratio A_m/A^* is then calculated. For $A_m/A^* > 1$, the flow is unchoked, whereas it becomes choked when $A_m/A^* = 1$. The calculation was done at the root and tip radii only, and the results are shown plotted in Fig. 23. It is apparent from here that at both the hub and tip radii, the ratio A_m/A^* approaches unity as M_T approaches about 0.92, confirming that the blade passages do indeed become choked at about $M_T = 0.92$; choking occuring almost simultaneously at all radii.

The second stage persists until the pressure ratio in Fig. 22 reaches about 1.7. In this regime, the variation of rotor speed is no longer linear with the axial velocity. Both the mass flow, and the upstream axial Mach number are constant. Further lowering of the downstream pressure merely

increases the axial velocity downstream, producing at the same time, a small increase in the upstream axial velocity. Very large increases in the pressure ratio are required to produce even a moderate increase in the rotor speed. Because of the large increase in axial velocity downstream, the fractional change in axial velocity across the rotor becomes larger. This explains why, in Fig. 20, beyond $M_T = 0.92$, much larger changes in axial velocity across the rotor occur, as compared to the values at the lower relative Mach numbers. As the downstream pressure is further lowered, a stage is soon reached at which the annulus itself becomes choked. This occurs at a relative tip Mach number of about 1.11.

Once this final operating point is reached, no further increase in rotor speed is possible. At this last relative Mach number the axial Mach number at midspan downstream of the blade row is about 0.75. Considering the ensuing frictional flow downstream, and assuming a mean skin friction coefficient of 0.00025, the maximum length of duct over which the flow can pass before choking occurs is about 12 hydraulic diameters of the annulus. For the channel geometry, this is about 20", which is of the same order of magnitude as the length of the flow annulus downstream of the measuring station.

IV.G Wave Drag

The total measured drag as a function of the relative tip Mach number is shown in Fig. 24. Included here are contributions due to D_1, D_2, D_3, D_4, D_5, D_6, and D_7. In the tests the Reynolds number based on blade tip radius was held approximately constant at 10^6; hence both D_1 and D_2 may be presumed approximately constant. Thus by subtracting from Fig. 24, the constant value of the drag for $M_T \leq 0.80$, we obtain a new drag curve, Fig. 25, consisting of the sum of D_3 through D_7. In Fig. 25 the drag rise prior to $M_T = 1$ is believed predominantly due to D_3, that is, due to the presence of shocks in the blade passages. Of course D_7 is zero for $M_T < 1$, and D_5 is negligible.

It is possible that D_4 also contributes to the drag in this region, but since the boundary layer on the blades is believed turbulent, separation, if ever it occurs, would probably not occur until the shock has moved close to the trailing edge of the blades; and the contribution of the resulting wake to the total drag should be relatively small. The contribution of D_6 to the total drag in this region will be estimated in a later section.

For $M_T > 1$, the drag in Fig. 25 is also made up of D_3 through D_7, where D_7 consists of the wave drag due to thickness, and also due to the lift on the blades. In this regime the drag due to shocks D_3 would be expected to decrease with relative Mach number, while that due to the waves would rise. Thus it might be expected that the drag curve would exhibit a minimum, as shown in Fig. 25.

A plot of the total drag is included in Fig. 22, versus the pressure ratio across the rotor. It exhibits the same behavior as discussed above, although its variation becomes more gradual. Since most of the transonic data were taken in the regime in which the blade passages were choked, it is probable that this may have influenced the drag measurements in this regime; in particular it may have been partly responsible for the minimum displayed by the drag curve at about $M_T = 1.02$, and the rather large drag rise beyond this point.

In subsequent sections these results will be compared with McCune's[13,14] analysis, supplemented by a new analysis which aims at estimating the drag rise due to lift for relative Mach numbers less than unity.

IV.H Accuracy of Measurements

All of the transducers used in the pressure measurements exhibited very good linearity and negligible hysteresis. Because of the use of differential transducers with small overall ranges, it was possible to measure static pressures very accurately with an accuracy of better than one part in a thousand, except at radial stations downstream of the rotor.

The special manner in which the downstream static pressure distributions

were obtained makes them subject to considerably higher errors than the wall static pressures. Fig. 12d shows that the parameter α used in the static pressure calibration depends on the radial position of the probe and hence, on the stream-line pattern around the probe. Hence any phenomenon which may influence the streamline geometry will also influence α. Since the calibration was done under 'no-rotor' conditions, the presence of swirl when the rotor is present may thus influence α. In order to estimate the effect of this on the static pressure distribution, an uncertainty of $\pm$ 5% in α has been assumed. This leads to a possible error of about $\pm$ 1% in the static pressures at Station 3, the highest errors occuring at the higher relative Mach numbers. The error band, at $M_T = 0.99$ is shown in Fig. 26. The corresponding axial velocity profiles are accurate to within $\pm$ 3%, while the tangential velocity profiles are in error by no more than 0.5%. These are also shown in Fig. 26.

The total pressure measurements made with the yaw probe, corrected for its low reading at zero pitch as mentioned in Section III.D-2, are believed accurate to within $\pm$ 0.5%, while the angle measurements are correct to $\pm 1/2^{\circ}$. The corresponding errors in drag coefficient, C_D, due to the uncertainties in static pressures are shown in Fig. 24. The error is greatest at the low Mach numbers, (about $\pm$ 40% at $M_T = .51$) and lowest at the high relative Mach numbers, (about $\pm$ 4% at $M_T = 1.11$). In fact, for $M_T > .92$, the error is of the order 4 to 6%.

The rotor speed could not be measured any more accurately than to within about $\pm$ 2 revolutions per second.

V. THEORETICAL ANALYSIS

V.A Wave Drag Due to Thickness

McCune[13, 14], in a detailed three-dimensional analysis of the axial compressor flow-field, has obtained an expression for the velocity field, from which the wave drag in the transonic regime may be obtained. His analysis, however, is limited to situations involving a non-lifting blade row, so that the wave drag obtained is that due to the finite thickness of the blades. The main features of the analysis, as well as those results from it which are pertinent to the present work are summarised in Appendix A.

Since, in any practical set up, there is always some lift on the compressor blades, McCune's analysis needs to be extended to take account of the contribution of the lift to the wave drag. Because of the complexities of a three-dimensional lifting surface theory, it seems desirable to first obtain some insight into the nature of the drag rise due to lift with the help of a simpler, two-dimensional lifting line theory. The inherent, three-dimensional nature of the transonic regime would necessarily preclude the use of such a theory in this domain; hence, in order to obtain information of sufficient validity, it would have to be restricted to relative Mach numbers which are less than unity. An attempt has therefore been made to obtain analytically, the induced drag up to high subsonic relative Mach numbers in a rotating turbo-machine.

V.B The Induced Drag for $M_T < 1$

1. The Differential Equation

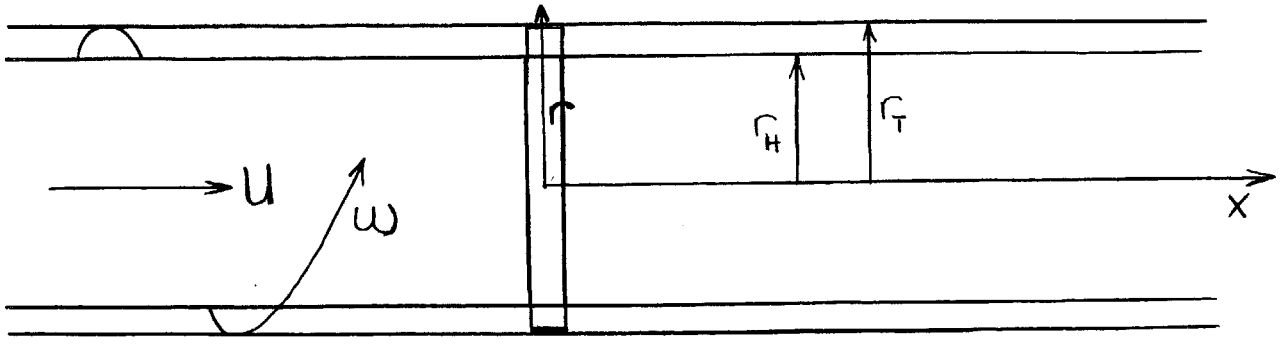

Figure (iii)

Following Reissner[8, 9], Davidson[10] and McCune[13, 14], we consider a blade row advancing with spee U and rotating with angular velocity ω. We let x_1, r_1, θ_1, t_1 be co-ordinates fixed in space. In these space-fixed co-ordinates, the linearized disturbance field produced by the blades satisfies the wave equation:

$$\frac{\partial^2\phi_1}{\partial r_1^2} + \frac{1}{r_1}\frac{\partial\phi_1}{\partial r_1} + \frac{1}{r_1^2}\frac{\partial^2\phi_1}{\partial\theta_1^2} + \frac{\partial^2\phi_1}{\partial x_1^2} = \frac{1}{a^2}\frac{\partial^2\phi_1}{\partial t_1^2} \tag{5.1}$$

Implicit in (5.1) is the assumption of frictionless, irrotational flow with small perturbations. If we transform into co-ordinates (r, θ, x) which advance and rotate with the rotor, through the transformation:

$$\begin{aligned} x &= x_1 + Ut_1 \\ r &= r_1 \\ \theta &= \theta_1 + \omega t_1 \end{aligned} \tag{5.2}$$

Equation (5.1) becomes

$$\left(1 - \frac{U^2}{a^2}\right)\phi_{xx} + \phi_{rr} + \frac{1}{r}\phi_r + \frac{1}{r^2}\left(1 - \frac{\omega^2 r^2}{a^2}\right)\phi_{\theta\theta} - \frac{2\omega U}{a^2}\phi_{x\theta} = 0 \tag{5.3}$$

It is assumed that in the rotor-fixed co-ordinates, the motion becomes steady after a sufficient length of time.

Further, if we use the notation:

$$\begin{aligned} M &= U/a \\ \beta^2 &= 1 - M^2 \\ z &= \omega x/U \\ \rho &= \omega r/U \end{aligned} \tag{5.3a}$$

Then, $$\beta^2\phi_{zz} + \phi_{\rho\rho} + \frac{1}{\rho}\phi_\rho + \frac{1}{\rho^2}(1 - M^2\rho^2)\phi_{\theta\theta} - 2M^2\phi_{\theta z} = 0 \tag{5.4}$$

If, as introduced by Goldstein[22], and later adopted by Reissner[8], and Kawada[23], we use the helical co-ordinate ζ, defined by:

$$\zeta = \theta - z \tag{5.5}$$

Then, (5.4) may be written as:

$$\beta^2\phi_{zz} + \phi_{\rho\rho} + \frac{1}{\rho}\phi_\rho + (1 + \frac{1}{\rho^2})\phi_{\zeta\zeta} - 2\phi_{z\zeta} = 0 \tag{5.6}$$

It may be expected that, far downstream of the rotor, the solution would depend only on the wake co-ordinate ζ and ρ, and not explicitly on z. At other regions, however, it would depend explicitly on all 3 co-ordinates ρ, θ and z.

The solution to (5.4) may therefore be split into two parts, the first, ϕ_1, the far wake solution, obtained by solving (5.6) with all the explicit derivatiives in z set equal to zero, and the second, ϕ_2, consisting of particular solutions of (5.4).

2. The Velocity Potential in the Far-Wake

The appropriate differential equation in the far-wake is obtained from (5.6) as:

$$\phi_{\rho\rho} + \frac{1}{\rho}\phi_\rho + (1 + \frac{1}{\rho^2})\phi_{\zeta\zeta} = 0 \tag{5.7}$$

Equation (5.7) is Laplace's equation, expressed in the helical co-ordinates (ζ,ρ). The far-wake solution thus has the same form as the incompressible solution. The solution to (5.7) has been obtained by Reissner[8], for a propeller in free air. Reissner's solution therefore only needs to be modified to account for the presence of a hub and a shroud.

We want a solution of (5.7) which leads to prescribable discontinuities in ϕ accross each helical wake surface, a discontinuity which may then be related to $\Gamma(\rho)$, the bound circulation distribution on the blades. Reissner obtained this solution by introducing a source-sink distribution of strength

$q(\rho,\zeta)$ per unit volume into the flow field. Equation (5.7) then is modified into:

$$\frac{1}{\rho}\frac{d}{d\rho}\left(\rho\frac{\partial\phi}{\partial\rho}\right) + \left(1+\frac{1}{\rho^2}\right)\frac{\partial^2\phi}{\partial\zeta^2} = \frac{-U^2}{\omega^2}\,q(\rho,\zeta) \tag{5.8}$$

The procedure thereafter is to choose a special form of $q(\rho,\zeta)$ which leads to the required discontinous solution $\phi^{(o)}$ at the helical sheets, and then to substract from this solution, the continuous solution $\phi^{(1)}$ due to whatever special form of $q(\rho,\zeta)$ is chosen. In this manner, the sources are removed from the flow field, leaving only the discontinuities at the helical surfaces.

Reissner used the special distribution of sources:

$$\frac{U^2}{\omega^2}\,q(\rho,\zeta) = -\left(\zeta - \frac{2\ell\pi}{B}\right)p(\rho) = -\zeta_\ell p(\rho) \tag{5.9}$$

where ζ_ℓ is taken to be zero midway between blades, and ℓ is a designation number of a blade, running from $\ell = 0$ to $\ell = (B-1)$. B is the number of blades.

(5.9) is a periodic distribution with ζ, linear in the spacing between blades as shown in Fig. (iv).

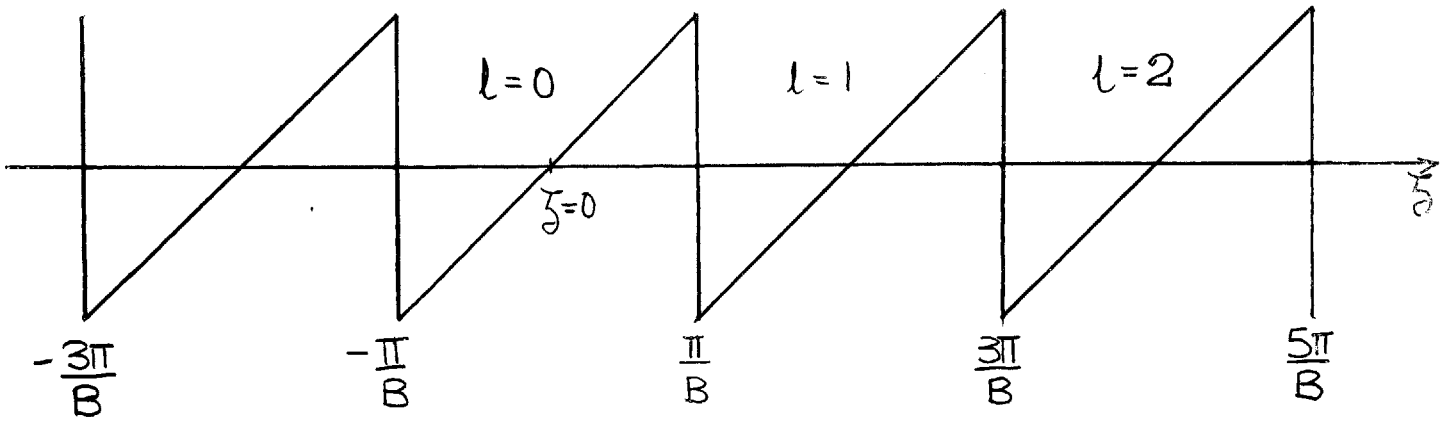

Figure (iv)

With this choice of $q(\rho,\zeta)$, the solution to (5.8) is

$$\phi^{(o)} = \zeta_\ell R^{(o)}(\rho) \tag{5.10}$$

provided $R^{(o)}(\rho)$ satisfies:

$$\frac{1}{\rho}\frac{d}{d\rho}\left(\rho\frac{dR^{(o)}}{d\rho}\right) = p(\rho) \tag{5.11}$$

With this form of $\phi^{(o)}$, the discontinuity in potential at the helical sheet is

$$\Delta\phi^{(o)} \text{ at } \zeta_\ell = \frac{\pi}{B}$$

$$= \frac{2\pi}{B} R^{(o)}(\rho) \equiv \Gamma(\rho) \tag{5.12}$$

where $\Gamma(\rho)$ is the bound circulation distribution on each blade or "lifting line".

Furthermore, the strength of the trailing vortex sheet is given by

$$E = \frac{d\Gamma}{dr} = \frac{2\pi}{B}\frac{\omega}{U}\frac{dR^{(o)}}{d\rho} \tag{5.13}$$

From (5.11) and (5.12) it follows that

$$p(\rho) = \frac{1}{\rho}\frac{d}{d\rho}\left(\rho\,\frac{B}{2\pi}\frac{d\Gamma}{d\rho}\right) = \frac{B}{2\pi\rho}\frac{d}{d\rho}\left(\rho\,\frac{d\Gamma}{d\rho}\right) \tag{5.14}$$

and from (5.10) and (5.12), we have

$$\phi^{(o)} = \frac{B\Gamma(\rho)}{2\pi}\zeta_\ell \tag{5.15}$$

The solution (5.15) was obtained by the introduction of the special source sink distribution (5.9). Therefore, in order to have the true solution to the original problem (5.7), we must subtract from $\phi^{(o)}$, the continuous solution due to the source distribution we have introduced.

If this solution, $\phi^{(1)}$ is written as

$$\phi^{(1)} = \sum_{n=1}^{\infty} R_n(\rho) \sin(nB\zeta) \tag{5.16}$$

and this, together with (5.9) is substituted into (5.8), we obtain, after

multiplying each term by sin $(nB\zeta)$ and integrating from $-\pi/B$ to $+\pi/B$, the differential equation:

$$\frac{1}{\sigma_n}\frac{d}{d\sigma_n}\left(\sigma_n \frac{dR_n}{d\sigma_n}\right) - \left(1 + \frac{n^2B^2}{\sigma_n^2}\right) R_n = -\frac{(-1)^n\, 2p}{(nB)^3} \tag{5.17}$$

where $\sigma_n = nBp$

The general solution of (5.17) is given in Reference 8, as

$$R_n = -\frac{(-1)^n 2}{(nB)^3}\left[f_n^{(1)}\, I_{nB}(\sigma_n) + f_n^{(2)}\, K_{nB}(\sigma_n) + I_{nB}(\sigma_n)\int_o^{\sigma_n} K_{nB}(\tau_n)\tau_n p d\tau_n - K_{nB}(\sigma_n)\int_o^{\sigma_n} I_{nB}(\tau_n)\tau_n p d\tau_n\right] \tag{5.18}$$

I_{nB} and K_{nB} are solutions of the homogenous equation, and are modified Bessel Functions of the first and second kinds respectively. $f_n^{(1)}$ and $f_n^{(2)}$ are arbitrary constants which may be determined by requiring that the complete far wake solution satisfies the conditions of vanishing radial velocity at hub and shroud. This complete far wake solution has the form

$$\phi = \phi^{(o)} - \phi^{(1)} \tag{5.19}$$

so that we may write:

$$\phi = \frac{B\Gamma(\rho)}{2\pi}\zeta_\ell - \sum_{n=1}^{\infty} R_n(\rho)\sin(nB\zeta) \tag{5.20}$$

Applying the above condition, and assuming that the circulation distribution has zero derivative at the shroud, the constants $f_n^{(1)}$ and $f_n^{(2)}$ may be determined, and $R_n(\rho)$ expressed in the form:

$$R_n = -\frac{(-1)^{n_2}}{nB}\frac{B}{2\pi}\left\{\frac{K'(\rho_T)I'(\rho_H)K(\rho) - K'(\rho_T)K'(\rho_H)I(\rho)}{Z(\rho_H,\rho_T)}\int_{\rho_H}^{\rho_T} I(\xi)\frac{d}{d\xi}(\xi\frac{d\Gamma}{d\xi})d\xi\right.$$

$$+\frac{I'(\rho_T)K'(\rho_H)I(\rho)-I'(\rho_H)I'(\rho_T)K(\rho)}{Z(\rho_H,\rho_T)}\int_{\rho_H}^{\rho_T} K(\xi)\frac{d}{d\xi}(\xi\frac{d\Gamma}{d\xi})\,d\xi \qquad (5.21)$$

$$+ I(\rho)\int_{\rho_H}^{\rho} K(\xi)\frac{d}{d\xi}(\xi\frac{d\Gamma}{d\xi})d\xi - K(\rho)\int_{\rho_H}^{\rho} I(\xi)\frac{d}{d\xi}(\xi\frac{d\Gamma}{d\xi})\,d\xi$$

$$\left.-\left[\frac{K(\rho)I'(\rho_T) - I(\rho)K'(\rho_T)}{Z(\rho_H,\rho_T)}\right]\Gamma'(\rho_H)\right\}$$

where $Z(\rho_H,\rho_T) = K'(\rho_T)I'(\rho_H) - K'(\rho_H)I'(\rho_T)$ (5.22)

and for brevity, the following notation has been used:

$$K_{nB}(nB\rho) \equiv K(\rho)\ , \quad I_{nB}(nB\rho) \equiv I(\rho)$$

$$\frac{d}{d\rho}K_{nB}(nB\rho) \equiv K'(\rho)\ , \quad \frac{d}{d\rho}I_{nB}(nB\rho) \equiv I'(\rho) \qquad (5.23)$$

It is necessary to make use of (5.14) in obtaining (5.21).

Substituting for $R_n(\rho)$ in (5.20), we obtain the far wake solution in the form:

$$\phi = \frac{B}{2\pi}\left[\Gamma(\rho)\zeta_\ell + \sum_{n=1}^{\infty}\frac{(-2)(-1)^n}{nB}\chi_n(\rho)\sin(nB\zeta)\right] \qquad (5.24)$$

$$\text{where } \chi_n(\rho) \equiv \chi_{nB}(nB\rho) = -\frac{K'(\rho_T)I'(\rho_H)K(\rho)-K'(\rho_T)K'(\rho_H)I(\rho)}{Z(\rho_H,\rho_T)}\int_{\rho_H}^{\rho_T} I(\xi)\frac{d}{d\xi}(\xi\frac{d\Gamma}{d\xi})d\xi$$

$$-\frac{I'(\rho_T)K'(\rho_H)I(\rho) - I'(\rho_H)I'(\rho_T)K(\rho)}{Z(\rho_H,\rho_T)}\int_{\rho_H}^{\rho_T} K(\xi)\frac{d}{d\xi}(\xi\frac{d\Gamma}{d\xi})\,d\xi$$

$$-I(\rho)\int_{\rho_H}^{\rho} K(\xi)\frac{d}{d\xi}(\xi\frac{d\Gamma}{d\xi})\,d\xi + K(\rho)\int_{\rho_H}^{\rho} I(\xi)\frac{d}{d\xi}(\xi\frac{d\Gamma}{d\xi})\,d\xi \qquad (5.24a)$$

$$+\frac{K(\rho)I'(\rho_T) - I(\rho)K'(\rho_T)}{Z(\rho_H,\rho_T)}\Gamma'(\rho_H)$$

The expression for $\chi_n(\rho)$ may be simplified if we integrate each of the terms by parts, still keeping the assumption that $\Gamma'(\rho_T) = 0$. Thus, we have:

$$\chi_n(\rho) = \frac{K'(\rho_T)I'(\rho_H)K(\rho) - K'(\rho_T)K'(\rho_H)I(\rho)}{Z(\rho_H,\rho_T)}\int_{\rho_H}^{\rho_T} I'(\xi)\xi\frac{d\Gamma}{d\xi}\,d\xi$$

$$+\frac{I'(\rho_T)K'(\rho_H)I(\rho) - I'(\rho_H)I'(\rho_T)K(\rho)}{Z(\rho_H,\rho_T)}\int_{\rho_H}^{\rho_T} K'(\xi)\xi\frac{d\Gamma}{d\xi}\,d\xi \qquad (5.25)$$

$$+I(\rho)\int_{\rho_H}^{\rho} K'(\xi)\xi\frac{d\Gamma}{d\xi}\,d\xi - K(\rho)\int_{\rho_H}^{\rho} I'(\xi)\xi\frac{d\Gamma}{d\xi}\,d\xi$$

3. The General 3-D Compressible Flow-Field

It now remains to obtain particular solutions to (5.4) which may be superposed on the far-wake solution. These particular solutions have the form

$$\phi_{nk} = A_{nk} \exp(inB\theta) \exp\left(\frac{inBM^2}{\beta^2} \pm \lambda_{nk}\right)z \quad R_{nB}\left(K_{nk}\frac{\rho}{\rho_T}\right) \tag{5.26}$$

where

$$\lambda_{nk} = \frac{1}{\beta}\sqrt{\frac{K_{nk}^2}{\rho_T^2} - \frac{n^2B^2M^2}{\beta^2}} \tag{5.27}$$

R_{nB} is a normalised combination of Bessel and Neumann functions of the first kind. The condition that each particular solution has zero radial velocity at hub and shroud gives K_{nk} as the solution of the eigenvalue equation:

$$J'_{nB}(hK_{nk})N'_{nB}(K_{nk}) = J'_{nB}(K_{nk})N'_{nB}(hK_{nk}) \tag{5.28}$$

where $h = \dfrac{\rho_H}{\rho_T}$

The sign of λ_{nk} in (5.26) is chosen so that ϕ_{nk} tends to zero at large distances upstream and downstream.

However, in compressible flow, density changes are necessarily accompanied by velocity changes, and hence, the axial velocity perturbation far downstream of the rotor must remain finite. This is accomplished by adding to ϕ_{nk} downstream, a term proportional to z, which is a special solution of (5.4). With these considerations, the complete solution for the velocity

potential takes the form:

$$\phi^u = R\,P\,\frac{B}{2\pi\beta^2}\left\{\sum_{k=1}^{\infty} A^u_{ok}\, e^{\lambda_{ok} z}\, R_o(K_{ok}\eta) + \sum_{n=1}^{\infty}\sum_{k=1}^{\infty} A^u_{nk}\, e^{inB\theta}\, e^{(\frac{inBM^2}{\beta^2} + \lambda_{nk})z}\, R_{nB}(K_{nk}\eta)\right\}$$

$$\phi^d = R\,P\,\frac{B}{2\pi\beta^2}\left\{C_1 z + \beta^2\Gamma(\eta)\zeta_\ell + \sum_{k=1}^{\infty} A^d_{ok}\, e^{-\lambda_{ok} z}\, R_o(K_{ok}\eta) + \beta^2\sum_{n=1}^{\infty}\sum_{k=1}^{\infty}\frac{(-2)(-1)^n}{nB}(-i)h_{nk}\, e^{inB\zeta}\, R_{nB}(K_{nk}\eta) + \sum_{n=1}^{\infty}\sum_{k=1}^{\infty} A^d_{nk}\, e^{inB\theta}\, e^{(\frac{inBM^2}{\beta^2} - \lambda_{nk})z}\, R_{nB}(K_{nk}\eta)\right\} \qquad (5.29)$$

where $\eta = \frac{\rho}{\rho_T}$

and the functions $\chi_n(\eta)$ have been expanded in a series of the orthonormal characteristic functions $R_{nB}(K_{nk}\eta)$ of the form:

$$\left.\begin{aligned}\chi_n(\eta) &= \sum_{k=1}^{\infty} h_{nk}\, R_{nB}(K_{nk}\eta)\\ \text{so that}\quad h_{nk} &= \int_h^1 \eta\,\chi_n(\eta)\, R_{nB}(K_{nk}\eta)\, d\eta\end{aligned}\right\} \qquad (5.30)$$

The following expansions will also be used subsequently:

For $n \neq 0$

$$\left.\begin{aligned}\Gamma(\eta) &= \sum_{k=1}^{\infty} \Gamma_{nk}\, R_{nB}(K_{nk}\eta)\\ \Gamma_{nk} &= \int_h^1 \eta\,\Gamma(\eta)\, R_{nB}(K_{nk}\eta)\, d\eta\end{aligned}\right\} \qquad (5.31)$$

For n = 0, the functions $R_o(K_{ok}\eta)$ do not form a complete set. This follows from the differential equation for $R_o(K_{ok}\eta)$, which is:

$$\rho R_o'' + R_o' + \frac{\rho K_{ok}^2}{\rho_T^2} R_o = 0 \tag{5.32}$$

Integrating term by term from ρ_H to ρ_T, and noting that $R_o' = 0$ at both end points, we obtain:

$$\int_h^1 \eta R_o(K_{ok}\eta)\, d\eta = 0 \tag{5.33}$$

Hence, any constant fuction is orthogonal to all the $R_o(K_{ok}\eta)$, which therefore is not a complete set. If a constant is added to the set however, then it becomes complete, and we may write,

For n = 0,

$$\left.\begin{aligned} \Gamma(\eta) &= C + \sum_{k=1}^{\infty} \Gamma_{ok}\, R_o(K_{ok}\eta) \\ \text{where} \quad C &= \frac{2}{1-h^2}\int_h^1 \Gamma(\eta)\, d\eta \\ \text{and} \quad \Gamma_{ok} &= \int_h^1 \eta\Gamma(\eta)\, R_o(K_{ok}\eta)\, d\eta \end{aligned}\right\} \tag{5.34}$$

* See note at the end of this section.

Finally, the function ζ_ℓ may be expanded in a Fourier series as

$$\zeta_\ell = R\, P \sum_{n=1}^{\infty} \frac{(-2)(-1)^n}{nB}(-i)\, e^{inB\zeta} \tag{5.35}$$

The unknown coefficients in (5.29) must be determined by requiring that the velocity potential be continuous at the matching plane z = 0, other than at points on the blade surfaces, and also, that no additional mass be

introduced into the flow at this plane.

For brevity, we write equations (5.29) in the form:

$$\phi^u = R\ P\ \frac{B}{2\pi\beta^2}\ \{\phi_1^u + \phi_2^u\}$$

$$\phi^d = R\ P\ \frac{B}{2\pi\beta^2}\ \{\phi_1^d + \phi_2^d + \phi_3^d + \phi_4^d + \phi_5^d\}$$

where the terms are numbered consecutively in each case.

Since ϕ_1^u, ϕ_1^d and ϕ_3^d are θ independent:
We require that

$$(\phi_1^u)_{z=o} = (\phi_1^d + \phi_3^d)_{z=o} \tag{5.36}$$

and consequently, that,

$$[\phi_2^u]_{z=o} = [\phi_2^d + \phi_4^d + \phi_5^d]_{z=o} \tag{5.37}$$

In the expression for ϕ_2^d to be used in (5.37), both $\Gamma(\eta)$ and ζ_ℓ are to be expanded as in (5.31) and (5.35).

The change in mass flow from upstream to downstream is:

$$[\Delta m] = \beta^2 \Delta V_x - \frac{\omega M^2}{U}\,\Delta(rV_\theta)$$

Hence, we require that:

$$\beta^2[\frac{\partial}{\partial x}(\phi_1^d + \phi_2^d + \phi_3^d) - \frac{\partial}{\partial x}(\phi_1^u)]_{z=o} - \frac{\omega M^2}{U}[\frac{\partial}{\partial\theta}(\phi_1^d + \phi_2^d + \phi_3^d) - \frac{\partial}{\partial\theta}(\phi_1^u)]_{z=o} = 0 \tag{5.38}$$

and

$$\beta^2[\frac{\partial}{\partial x}(\phi_4^d + \phi_5^d) - \frac{\partial}{\partial x}(\phi_2^u)]_{z=o} - \frac{\omega M^2}{U}[\frac{\partial}{\partial\theta}(\phi_4^d + \phi_5^d) - \frac{\partial}{\partial\theta}(\phi_2^u)]_{z=o} = 0 \tag{5.39}$$

In (5.38), use must be made of (5.34).

Finally, we obtain the coefficients in the forms:

$$A^u_{ok} = A^d_{ok} = -\frac{\Gamma_{ok}}{2\lambda_{ok}} \tag{5.40}$$

$C_1 = C$

$$\left.\begin{aligned} A^u_{nk} &= -i\beta^2 \frac{(-2)(-1)^n}{nB} \frac{(\Gamma_{nk} + h_{nk})}{2} + (-1)^n \frac{h_{nk}}{\lambda_{nk}} \\ A^d_{nk} &= i\beta^2 \frac{(-2)(-1)^n}{nB} \frac{(h_{nk} + \Gamma_{nk})}{2} + \frac{(-1)^n h_{nk}}{\lambda_{nk}} \end{aligned}\right\} \tag{5.41}$$

The complete solution (5.29) now takes the form:

$$\phi^u = R\,P\,\frac{B}{2\pi\beta^2}\left\{\sum_{k=1}^{\infty}\frac{-\Gamma_{ok}}{2\lambda_{ok}} e^{\lambda_{ok}z} R_o(K_{ok}\eta)\right.$$

$$\left. + \sum_{n=1}^{\infty}\sum_{k=1}^{\infty}\left[\frac{(-1)^n}{\lambda_{nk}}h_{nk} - i\beta^2\frac{(-2)(-1)^n}{nB}\frac{(h_{nk}+\Gamma_{nk})}{2}\right] e^{inB\theta}\, e^{(\frac{inBM^2}{\beta^2}+\lambda_{nk})z}\, R_{nB}(K_{nk}\eta)\right\}$$

$$\phi^d = R\,P\,\frac{B}{2\pi\beta^2}\left\{Cz + \beta^2\Gamma(\rho)\zeta_\ell - \sum_{k=1}^{\infty}\frac{\Gamma_{ok}}{2\lambda_{ok}} e^{-\lambda_{ok}z} R_o(K_{ok}\eta)\right. \tag{5.42}$$

$$+ \sum_{n=1}^{\infty}\sum_{k=1}^{\infty}\beta^2\frac{(-2)(-1)^n}{nB}(-i)h_{nk}\, e^{inB\zeta}\, R_{nB}(K_{nk}\eta)$$

$$\left. + \sum_{n=1}^{\infty}\sum_{k=1}^{\infty}\left[\frac{(-1)^n}{\lambda_{nk}}h_{nk} + i\beta^2\frac{(-2)(-1)^n}{nB}\frac{(h_{nk}+\Gamma_{nk})}{2}\right] e^{inB\theta}\, e^{(\frac{inBM^2}{\beta^2}-\lambda_{nk})z}\, R_{nB}(K_{nk}\eta)\right\}$$

With this solution it may be verified by direct evaluations at z=o, that:

$$\phi^d - \phi^u = \frac{B}{2\pi}\left\{\Gamma(\rho)\ (\theta - \frac{2\ell\pi}{B}) - \sum_{n=1}^{\infty} \frac{(-2)(-1)^n}{nB}\Gamma(\rho)\ \sin nB\theta\right\}$$

which is identically zero, by virtue of (5.35), if $\theta \neq \pm \frac{\pi}{B}$.

If $\theta = \pm \frac{\pi}{B}$, ie, at the helical surface, then the series converges to zero, and

$$[\phi^d - \phi^u]_{\frac{\pi}{B}-}^{\frac{\pi}{B}+} = \Gamma(\rho)$$

Since ϕ^u is a continuous function of ρ, θ, z, it follows that

$$[\phi^d]_{\zeta=\frac{\pi}{B}-}^{\frac{\pi}{B}+} = \Gamma(\rho) \quad \text{as should be expected.}$$

Similarly, $[r\Delta V_\theta]_{z=o} = \frac{B}{2\pi}\left\{\Gamma(\rho) + \sum_{n=1}^{\infty}(-1)^n\, 2\Gamma(\rho)\cos nB\theta\right\} = \Gamma(\rho)\delta[\theta_\ell - \frac{\pi}{B}]$

Hence, $\int_{\pi/B-}^{\pi/B+} (r\Delta V_\theta)d\theta_\ell = \Gamma(\rho)$, also as should be expected.

Furthermore, $[\Delta V_r]_{z=o} = \frac{B}{2\pi}\Gamma'(\rho)\left\{\theta_\ell - \sum_{n=1}^{\infty}\frac{(-2)(-1)^n}{nB}\sin nB\theta\right\}$

Thus, for $\theta \neq (2\ell + 1)\frac{\pi}{B}$, $\Delta V_r \equiv 0$

and for $\theta = (2\ell + 1)\frac{\pi}{B}$, the second term converges to zero, and we have:

$$[\Delta V_r]_{\zeta=\frac{\pi}{B}-}^{\frac{\pi}{B}+} = \Gamma'(\rho)$$

We may also demonstrate that, with the solution (5.42) the mass flow is conserved between far upstream and far downstream conditions:

$$[\Delta\dot{m}]_{-\infty}^{\infty} = 2\pi\int_{r_H}^{r_T} (\sigma_\infty V_x + \sigma' U)\ r dr \qquad (5.43)$$

where σ_∞ denotes the free stream density, and σ' is the density perturbation.

From (5.42)

$$\left|V_x\right|_{z \to \infty} = \frac{\omega B}{2\pi\beta^2 U}\left[C - \beta^2\Gamma(\rho)\right] \tag{5.44}$$

$\sigma' = -(\sigma_\infty/a^2)\left[UV_x + \omega r V_\theta\right]$, so that

$$\left[\sigma'\right]_{z\to\infty} = \frac{-\sigma_\infty}{a^2}\frac{\omega BC}{2\pi\beta^2} \tag{5.45}$$

$$\left[\Delta\dot{m}\right]_{-\infty}^{\infty} = \frac{\omega B\sigma_\infty}{U}\int_{r_H}^{r_T}(C - \Gamma)\, r dr = \frac{\omega B\sigma_\infty r_T^2}{U}\int_h^1 (C - \Gamma)\eta d\eta$$

$$= \frac{\omega B\sigma_\infty r_T^2}{U}\left[\frac{C(1-h^2)}{2} - \int_h^1 \Gamma(\eta)\eta d\eta\right]$$

= 0 by virtue of (5.34) and (5.41)

The solution (5.42) therefore satisfies all of the necessary conditions of the problem.

*Note to equations (5.31) and (5.34)

It must be remarked here that the expansions of the function Γ as in (5.31) and (5.34) are strictly valid only if its derivative vanishes at both hub and tip. This however does not constitute a major restriction in practice since for any actual Γ that does not satisfy this requirement, it can be replaced by another function which is identical with it everywhere except at the hub and tip, and which satisfies the necessary requirements at these regions.

4. The Induced Velocities

The induced velocities at the blades are calculated by taking the mean of the upstream and downstream velocities. Thus, differentiating (5.42) at $z = 0$, and $\zeta = \theta = \frac{\pi}{B}$, we obtain the induced velocities in the forms:

$$V_x^* = \left[\frac{1}{2}(V_x^u + V_x^d)\right]_{\substack{z=o \\ \theta=\frac{\pi}{B}}} = RP\ \frac{\omega B}{4\pi\beta^2 U}\left\{\sum_{n=1}^{\infty}\sum_{k=1}^{\infty}\left(\frac{2inBM^2}{\lambda_{nk}\beta^2} + \frac{2i\beta^2}{nB}\lambda_{nk} + 2\beta^2\right) h_{nk}R_{nB}\right.$$

$$\left. + \sum_{n=1}^{\infty}\sum_{k=1}^{\infty}\left(\frac{2i\beta^2\lambda_{nk}}{nB}\right)\Gamma_{nk}R_{nB} + C - \beta^2\Gamma(\rho)\right\} \tag{5.46}$$

$$V_\theta^* = \left[\frac{1}{2}(V_\theta^u + V_\theta^d)\right]_{\substack{z=0 \\ \theta=\frac{\pi}{B}}} = RP\ \frac{B\omega}{4\pi\beta^2 U\rho}\left\{\sum_{n=1}^{\infty}\sum_{k=1}^{\infty}\left(\frac{2inB}{\lambda_{nk}} - 2\beta^2\right)h_{nk}R_{nB} + \beta^2\Gamma(\rho)\right\} \tag{5.47}$$

As already noted, in applying a "lifting-line" approximation we limit ourselves to $M_T < 1$. It can be shown that for such cases λ_{nk} is real. That is from equation (5.27).

$$\lambda_{nk} = \frac{1}{\beta}\sqrt{\frac{K_{nk}^2}{\rho_T^2} - \frac{n^2B^2M^2}{\beta^2}}$$

For imaginary λ_{nk}, we must have:

$$\frac{n^2M^2B^2}{\beta^2} > \frac{K_{nk}^2}{\rho_T^2}$$

i.e.
$$\frac{\beta^2}{M^2} < \frac{n^2\rho_T B^2}{K_{nk}^2} \tag{5.48}$$

At the sonic cylinder (ρ_s), namely the radius where the relative Mach number

is unity;

$$U^2 + \omega^2 r_s^2 = a^2$$

or $$M^2 + \rho_s^2 M^2 = 1$$

$$\text{i.e.} \quad \rho_s^2 = \frac{\beta^2}{M^2} \tag{5.49}$$

Thus for λ_{nk} imaginary, we must have, combining (5.48) and (5.49);

$$\rho_s^2 < \frac{n^2}{K_{nk}^2} \rho_T^2 B^2 \tag{5.50}$$

In general, $K_{nk} > nB$ [24]; so that (5.50) implies

$$\rho_T > \rho_s \tag{5.51}$$

Thus, for imaginary λ_{nk} to occur, the sonic cylinder must lie within the flow annulus, or, equivalently, M_T must be greater than unity.

Hence, if we limit consideration then to cases for which $M_T < 1$, and take the real parts of (5.46) and (5.47), remembering that λ_{nk} is real, we obtain:

$$V_x^* = \frac{\omega B}{4\pi\beta^2 U} \left\{ \sum_{n=1}^{\infty} \sum_{k=1}^{\infty} 2\beta^2 h_{nk} R_{nB} + C - \beta^2 \Gamma(\rho) \right\}$$

$$= \frac{\omega B}{4\pi\beta^2 U} \left\{ 2\beta^2 \sum_{n=1}^{\infty} \chi_n(\rho) + C - \beta^2 \Gamma(\rho) \right\} \tag{5.52}$$

$$V_\theta^* = \frac{B\omega}{4\pi\beta^2 U\rho} \left\{ \sum_{n=1}^{\infty} \sum_{k=1}^{\infty} - 2\beta^2 h_{nk} R_{nB} + \beta^2 \Gamma(\rho) \right\}$$

$$= \frac{B\omega}{4\pi U\rho} \left\{ \Gamma(\rho) - 2 \sum_{n=1}^{\infty} \chi_n(\rho) \right\} \tag{5.53}$$

5. The Induced Drag

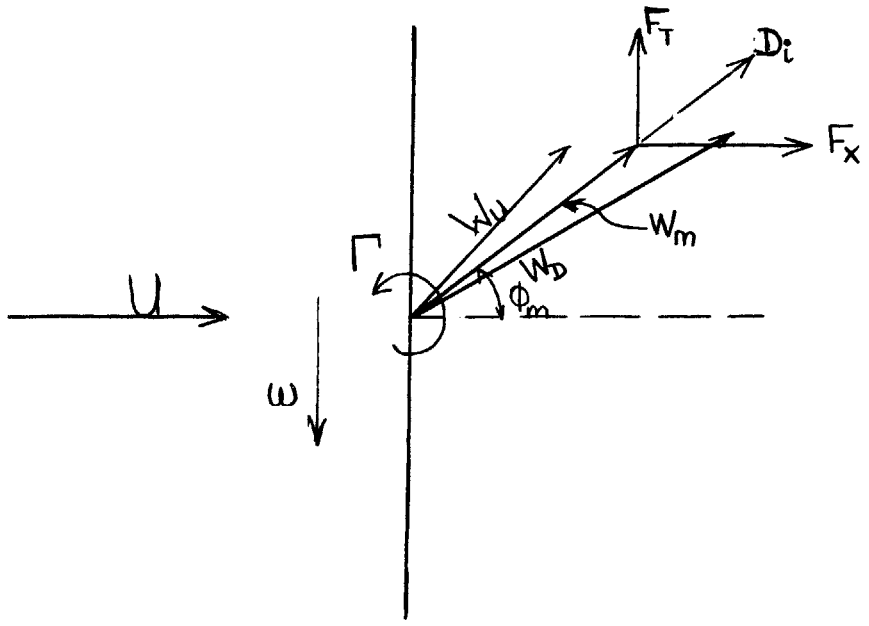

Figure (v)

Let W_u and W_D represent the relative velocities far upstream and far downstream of the rotor respectively, and let W_m be the mean of these relative velocities. We shall denote by the Drag, that component of the resultant force on the rotor which acts parallel to W_m.

The tangential and axial forces acting on the rotor can be obtained from the induced velocities at the blades.

Thus, if F_T denotes the tangential force, and F_x the axial force,

$$F_T = -(\sigma_\infty + \sigma^*)(U + V_x^*)\Gamma \tag{5.54}$$

and

$$F_x = (\sigma_\infty + \sigma^*)(\omega r + V_\theta^*)\Gamma \tag{5.55}$$

Remembering that

$$\sigma^* = \frac{-\sigma_\infty}{a^2}[UV_x^* + \omega r V_\theta^*]$$

and substituting for V_x^* and V_θ^* from (5.52 and (5.53) we obtain:

$$F_T = -\sigma_\infty U\Gamma + \frac{\sigma_\infty \omega B\Gamma}{4\pi U}\left\{\Gamma - C - 2\sum_{n=1}^{\infty} \chi_n(\rho)\right\} \tag{5.56}$$

$$F_x = \sigma_\infty U\rho\Gamma + \frac{\sigma_\infty \omega B\Gamma}{4\pi U}\left\{\frac{\Gamma}{\rho} - \frac{2}{\rho}\sum_{n} \chi_n(\rho) - \frac{M^2\rho C}{\beta^2}\right\} \tag{5.57}$$

If ϕ_m denotes the angle which the mean relative velocity makes with the axial direction, then we may define the mean relative velocity as corresponding to

$$\cos \phi_m = \frac{U + \frac{\langle V_x \rangle}{2}}{W_m} \tag{5.58}$$

$$\text{where } W_m^2 = [U + \frac{\langle V_x \rangle}{2}]^2 + [\omega r + \frac{\langle V_\theta \rangle}{2}]^2 \tag{5.59}$$

$\langle V_x \rangle$ and $\langle V_\theta \rangle$ denote the circumferential mean of the axial and tangential velocity perturbations far downstream of the rotor. It can be directly verified from the general solution that:

$$\langle V_x \rangle = \frac{\omega B}{2\pi\beta^2 U}\left\{C - \beta^2\Gamma\right\} \tag{5.60}$$

$$\langle V_\theta \rangle = \frac{B\omega\Gamma}{2\pi U\rho} \tag{5.61}$$

Thus expanding and retaining only terms up to the first order, we have:

$$\cos \phi_m = \frac{1}{\sqrt{1+\rho^2}}\left\{1 + \frac{\omega B}{4\pi U^2\beta^2}\left(\frac{C\rho^2}{1+\rho^2} - \beta^2\Gamma\right)\right\} \tag{5.63}$$

and

$$\sin \phi_m = \frac{\rho}{\sqrt{1+\rho^2}}\left\{1 - \frac{\omega B}{4\pi U^2 \beta^2 \rho^2}\left(\frac{C\rho^2}{1+\rho^2} - \beta^2\Gamma\right)\right\} \tag{5.64}$$

From Fig. (v), the induced drag is then obtained as

$$D_i(\rho) = F_T \sin \phi_m + F_x \cos \phi_m \tag{5.65}$$

Substituting the appropriate quantities from (5.56), (5.57), (5.63) and (5.64), we have finally,

$$D_i(\rho) = \frac{-\sigma_\infty \omega B\Gamma}{2\pi U \sqrt{1+\rho^2}}\left(\rho + \frac{1}{\rho}\right) \sum_{n=1}^{\infty} \chi_n(\rho) \tag{5.66}$$

keeping only terms up to second order.

If either $\Gamma(\rho) \equiv 0$, or $\Gamma(\rho) =$ constant, then the induced drag is zero, as might be expected.

The induced drag coefficient is given by

$$C_{Di}(\rho) = \frac{D_i(\rho)}{\frac{\sigma_\infty U^2}{2} C_{ax}} = \frac{-\omega B\Gamma(\rho)}{\pi U^3 C_{ax}\sqrt{1+\rho^2}}\left(\rho + \frac{1}{\rho}\right) \sum_{n=1}^{\infty} \chi_n(\rho) \tag{5.67}$$

and the total drag coefficient per blade is

$$C_{DW_i} = \frac{D_i}{\frac{\sigma_\infty U^2}{2} C_{ax} r_T} = \int_{\rho_H}^{\rho_T} \frac{C_{Di}(\rho)}{\rho_T}\, d\rho \tag{5.68}$$

6. Numerical Evaluation of C_{DW_i}

In the numerical evaluation of (5.67), use was made of the approximate expressions for the functions $I_m(x)$ and $K_m(x)$ given by Nicholson[26]. These have the form:

$$I_m(x) = (2\pi x \cosh \beta)^{-1/2} e^{x(\cosh \beta - \beta \sinh \beta)} \tag{5.69}$$

$$K_m(x) = \pi (2\pi x \cosh \beta)^{-1/2} e^{-x(\cosh \beta - \beta \sinh \beta)} \tag{5.70}$$

where $\sinh \beta = \frac{m}{x}$

In particular, we find that

$$I_{nB}(nB\rho) = \frac{1}{(2nB\pi)^{1/2}} \frac{1}{\tau^{1/2}} \left[e^{\tau} \left(\frac{\tau-1}{\tau+1}\right)^{1/2} \right]^{nB} \tag{5.71}$$

$$K_{nB}(nB\rho) = \left(\frac{\pi}{2nB}\right)^{1/2} \frac{1}{\tau^{1/2}} \left[e^{\tau} \left(\frac{\tau-1}{\tau+1}\right)^{1/2} \right]^{-nB} \tag{5.72}$$

where $\tau = (1+\rho^2)^{1/2}$ (5.73)

In evaluating $\chi_n(\rho)$ numerically, it must be noticed that, for any reasonable values of ρ_H and ρ_T, and for nB greater than about 10,

$$|K'(\rho_H)I'(\rho_T)| >> |K'(\rho_T)I'(\rho_H)| \tag{5.74}$$

Thus, we may write

$$Z(\rho_H, \rho_T) \sim - K'(\rho_H)I'(\rho_T) \tag{5.75}$$

Using these assumptions, the expression for $\chi_n(\rho)$ may be written in the simplified form:

$$\chi_n(\rho) = K'(\rho_T)I(\rho) \int_{\rho_H}^{\rho_T} \frac{I'(\xi)}{I'(\rho_T)} \xi \frac{d\Gamma}{d\xi} d\xi + I'(\rho_H)K(\rho) \int_{\rho_H}^{\rho_T} \frac{K'(\xi)}{K'(\rho_H)} \xi \frac{d\Gamma}{d\xi} d\xi$$
$$- \int_{\rho}^{\rho_T} I(\rho)K'(\xi)\xi \frac{d\Gamma}{d\xi} d\xi - \int_{\rho_H}^{\rho} K(\rho)I'(\xi)\xi \frac{d\Gamma}{d\xi} d\xi \tag{5.76}$$

In evaluating (5.76), it is assumed that the distribution $\Gamma(\rho)$ is known. For the purpose of the present calculations, a reasonable expression for $\Gamma(\rho)$ was developed from the experimental tangential velocity profiles. The

circulation around each blade is given by:

$$\Gamma(r) = \frac{2\pi r}{B}(V_{\theta 3} - V_{\theta 2}) = + \frac{2\pi r}{B} V_{\theta 3} \qquad (5.77)$$

assuming that $V_{\theta 2} = 0$.

From the experimental plots of the tangential velocity profiles at station 3, it seems reasonable, at relative Mach numbers below unity, to assume for computational purposes, the simple distribution shown in Fig. (vi).

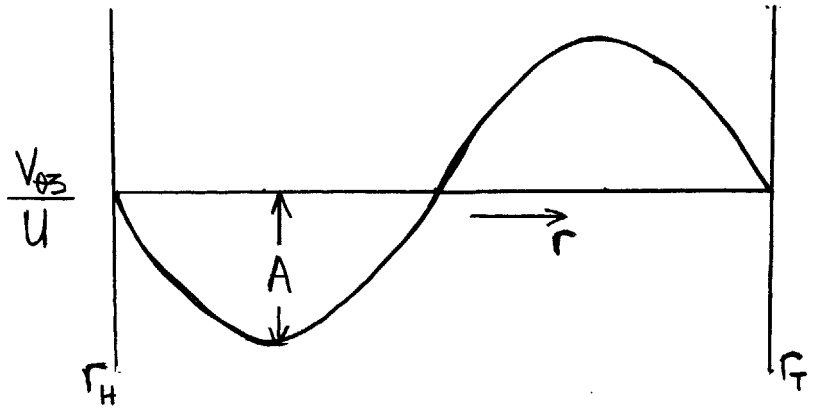

Figure (vi)

It must be noted that the convention used in plotting the data assumes that $V_{\theta 3}$ is positive in the direction of rotation of the rotor, whereas the opposite convention is used in the present analysis. Thus, for consistency with the analytical convention, we shall represent the distribution in Fig. (vi) by the expression

$$\frac{V_{\theta 3}}{U} = A \sin 2\pi \frac{(r-r_H)}{(r_T-r_H)} \quad , \qquad A > 0 \qquad (5.78)$$

where A may be a function of the relative Mach number.

Combining (5.77) and (5.78)

$$\Gamma(\rho) = \frac{2\pi U^2 \rho A}{B\omega} \sin 2\pi \frac{(\rho-\rho_H)}{(\rho_T-\rho_H)} \qquad (5.79)$$

Using this in (5.67), we obtain:

$$C_{Di}(\rho) = \frac{-2\rho A}{UC_{ax}\sqrt{1+\rho^2}} \sin 2\pi \frac{(\rho-\rho_H)}{(\rho_T-\rho_H)} \left\{ \sum_{n=1}^{\infty} (\rho + \frac{1}{\rho}) \chi_n(\rho) \right\} \qquad (5.80)$$

The circulation distribution represented by (5.79) has the form shown in Fig. (vii).

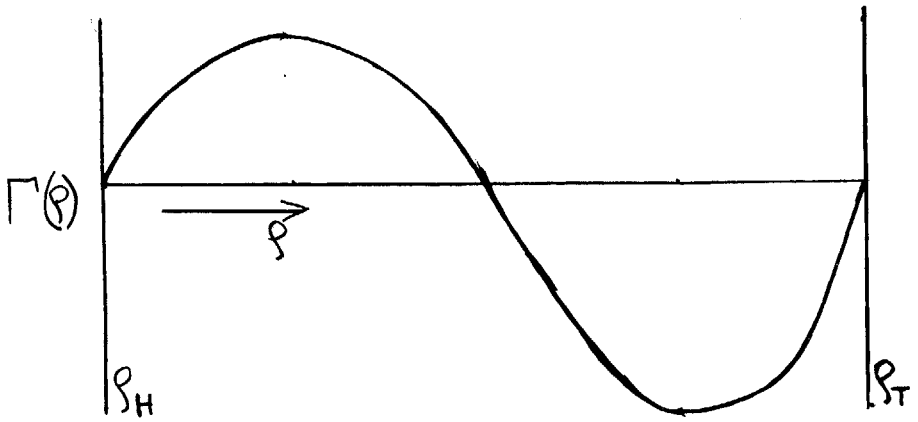

Figure (vii)

In all the calculations, a value of A = 0.05 was used corresponding to a maximum change in tangential velocity across the rotor of 5% of the upstream axial velocity.

7. Behavior of the Series $\chi_n(\rho)$

The convergence of the series for $\chi_n(\rho)$ depends markedly on the value of ρ. The convergence is very rapid for values of ρ not too close to the root and tip regions, where it converges much less rapidly. Fortunately, however, this is not of much consequence in the present case, since for the particular choice of $\Gamma(\rho)$, the drag vanishes at the root and tip, as may be seen from (5.80). Table 2 shows the values of successive terms in $\chi_n(\rho)$ at 5 radial positions corresponding to η = .8, .85, .90, .95 and 1.00. This table was

obtained for a tip relative Mach number of 0.51, $\frac{\omega}{U} = 5.16$, and $\rho_T = 1.756$.

From the table, the accuracy obtained by terminating the series after n terms can easily be estimated. If only the first ten terms are used, then the accuracy everywhere except at the root and tip is 1% or better, being only between 3% and 4% at these regions. Extension of the series to 15 terms improves the accuracy at the root and tip to about 2% while that at other regions is now better than 1/2 %. In the calculations, 15 terms of the series were used.

VI. COMPARISON OF ANALYSIS AND EXPERIMENT

A. Analytical Results--Wave Drag

The analytical techniques for evaluating the wave drag at relative Mach numbers greater than unity are discussed in Appendix A. All of the results discussed here are for a blade row with 40 blades, having double parabolic arc profiles, a hub-tip ratio of 0.80, and L/Cax = 1.82. The blade thickness in the axial direction, Cax is 0.352", while the tip radius of the blades is 0.34'. The blades have the thickness distribution described by equation (A7), with the thickness to chord ratio at the hub being 0.23. For this geometry, the relevant coefficients Q^*_{nk} which appear in equation (A5) are given in Table 1.

The convergence properties of the series in (A5) may be seen by a reference to Table 3, which shows the values of the quantity under the summation sign for different values of n and k. Also included in the table are the partial sums over k for each n. The table is for $M_T = 0.98$, x/Cax = 0.5, and η =0.80; 1.00; i.e., at the root and tip. The convergence of the series is slowest near $M_T = 1.0$, so that the convergence at other values of M_T may be assumed to be at least as good as that at $M_T = .98$. It is seen from the partial sums that at this Mach number the convergence at the root is much better than at the tip, the estimated error in terminating the series after 10 terms in n being of the order of 1% at the root and 2% at the tip. Further evidence of the adequacy of the convergence is also given by the fact that doubling the number of terms in n to 20 does not result in any appreciable difference in either the pressure distribution over the blades or in the wave drag at this Mach number.

Fig. 27 shows the pressure distribution over the blades at $M_T = 0.98$, this being typical of the subsonic regime. It is symmetrical with respect to the blade mid-chord and exhibits singularities at both the

leading and trailing edges. Because of its symmetry, the resulting wave drag is zero. The waviness of the pressure distributions near the leading and trailing edges is of interest. Its similarity of shape at all radii suggests that it cannot be attributed to insufficient convergence of the series, since, as was mentioned above, the accuracy at the hub is slightly better than 1%. Moreover, the same curve is preserved if 20 terms of the series are used instead of 10. Secondly, the waviness is noticeable only at the higher subsonic relative tip Mach numbers. This is evident from Fig. 28, which shows the pressure distribution at the hub and tip for $M_T = 0.75$. It appears that at this Mach number the waviness is just beginning. This suggests that it is most probably associated with 3-D compressibility effects.

A possible conjecture is that as the relative Mach number approaches unity, three dimensional effects come increasingly into play, with pressure waves originating from the leading and trailing edges of the blades. Because of the singularities at these locations, it would be expected that such waves would have their largest amplitudes there. However, since for $M_T < 1$, all the λ_{nk}'s are real, i.e., the amplitudes of the disturbances approach zero at large distances from their source in both the upstream and downstream directions, the amplitudes of these waves decrease very rapidly as they travel out from the leading and trailing edges, the decay being exponential. Thus since no wave energy travels out to infinity, no wave drag is associated with them. The waves may be thought of as cancelling out each other. As soon as M_T exceeds unity sufficiently, some of the λ_{nk}'s become imaginary, and it is now possible for such wave modes to propagate to infinity, and thus lead to wave drag.

The drag rise with tip Mach number is shown in Fig. 29. The shape of this curve confirms the earlier conjectures of McCune[13]. Successive bumps

in the drag curve correspond to the "resonance" of various wave modes. It is explained in Appendix A that the amplitude of each wave mode varies as $e^{\pm\lambda_{nk}z}$, and that λ_{nk} is given by

$$\lambda_{nk} = \frac{nB}{\beta\rho_T}\sqrt{\frac{K_{nBk}^2}{n^2B^2} - \frac{\rho_T^2}{\rho_s^2}} \tag{6.1}$$

For given B, M, h, n and k, both ρ_s, and K_{nBk}/nB are fixed, and ρ_T/ρ_s depends on M_T. Thus λ_{nk} depends only on M_T. It has been shown elsewhere that $\frac{K_{nBk}}{nB} \to 1$, so that for $\frac{\rho_T}{\rho_s} < 1$, i.e., for $M_T < 1$, the λ_{nk}'s are all real, and all the wave mode amplitudes decay exponentially, and there is no wave drag. As M_T increases above unity, ρ_T/ρ_s also increases above 1, and it is possible for λ_{nk} to become very small, and eventually become imaginary. For as long as λ_{nk} is real, the amplitude of the wave mode would decay exponentially far away from the blades and no net energy is radiated away by it. There is thus no wave drag. As M_T increases, however, λ_{nk} would eventually become imaginary. The associated wave mode would then radiate outwards undiminished in intensity, and there would be a net wave drag associated with it. In particular, when λ_{nk} is very nearly zero but imaginary, the amplitude of the associated wave mode would become very large, as may be inferred from equation (A.5), and it will then contribute very strongly to the wave drag. This phenomenon is usually referred to as "resonance". Different wave modes would thus become resonant at different tip relative Mach numbers, and the manner in which this takes place would determine the nature of the wave drag rise. The drag rise computed from McCune's analysis is shown in Fig. 29, with the radial distribution at $M_T = 1.07$ shown in Fig. 30.

B. Analytical Results - Induced Drag for $M_T < 1$

Fig. 31 is typical of the radial distribution of the induced drag. The distribution of circulation giving rise to this drag is also shown on the

same figure. It is a sine curve with radially increasing amplitude. It is significant that, except for a small region near the tip and hub, the drag is everywhere positive. Both the regions of positive and negative circulation have positive drag associated with them. Thus even in a blade row in which the net torque is exactly zero, there will be an induced drag, as long as the circulation changes with radial position along the span. Although the circulation function used here does not have zero derivatives at the root and tip as the theory requires, nevertheless, consistent with earlier remarks, this is no limitation to the applicability of the theory, since the function can be modified slightly at these regions in such a manner that its derivative vanishes there while leaving the function itself unchanged at all other points. However, since the function may be thus deformed in an infinite number of ways without affecting the resulting drag distribution, it must be concluded that for any circulation distribution which does not satisfy these "natural" boundary conditions, there is some uncertainty as to the accuracy of the theory near the root and tip regions.

The induced drag coefficient, as a function of tip relative Mach number, is shown in Fig. 32. At each Mach number, a tangential velocity distribution of the form shown in Fig. (vi) is assumed, with A = .05. Under these conditions the induced drag appears relatively independent of tip Mach number.

C. Comparison with Experiment

In comparing the present theories with the experiment, it will be desirable to break the Mach number range under consideration into two distinct regimes, namely, $M_T < 1$ and $M_T > 1$.

Fig. 25 shows the total drag, exclusive of the skin friction drag, throughout the Mach number range. Also shown here is the calculated wave drag due to thickness from McCune's theory. First, for $M_T < 1$, it will be desirable to see how much of the drag is due to the circulation on the blades. This

is shown in Fig. 32. To convert the values of C_D in Fig. 32 so as to compare them with Fig. 25, it is only necessary to multiply the values in Fig. 32 by 1.1, since

$$\frac{D_{Total}}{\frac{\rho U^2}{2}\pi r_T^2} = \frac{(D_{Total}/B)}{\frac{\rho U^2}{2} C_{ax} r_T} \left(\frac{BC_{ax}}{\pi r_T}\right) = \frac{(D_{Total}/B)}{\frac{\rho U^2}{2} C_{ax} r_T} \left(\frac{2C_{ax}}{L}\right) \tag{6.2}$$

Thus, the drag coefficient due to lift for $M_T < 1$ is approximately constant, and equal to about $.3 \times 10^{-3}$. This is much smaller than the total drag, and hence, it is obvious that the induced drag in this region may be neglected. This means that all of the drag in Fig. 25 for $M_T < 1$ must be attributed to the presence of shocks in the blade passages. To check this, it will be necessary to compare the drag values in Fig. 25 for $M_T < 1$ with Bryson's two dimensional pressure drag data on the 12% biconvex circular arc profiles, refered to earlier. Such a comparison is legitimate, since for $M_T < 1$, three dimensional effects are not too important, except when M_T is very close to 1, say of the order of 0.98. Hence, for M_T less than this value, if the flow over the blade span is appropriately averaged, it may be compared with a corresponding 2-D flow, at least to first order approximation. The averaging procedure used for purposes of comparison is as follows:

Bryson's definition of C_D is of the form:

$$C_{DB} = \frac{D}{\frac{\sigma_\infty U_\infty^2 C}{2}} \tag{6.3}$$

where U_∞ is the 2-D free stream velocity

C is the blade chord

and σ_∞ is the free stream density.

We may define a corresponding drag coefficient for the compressor blade row in the form:

$$\overline{C_{DB}} = \frac{\overline{D}(r_T - r_H)}{\frac{\sigma_\infty U_R^2}{2}\overline{C}(r_T - r_H)} = \frac{D_{Total}}{\frac{\sigma_\infty U^2}{2}\pi r_T^2} \quad \frac{\pi r_T}{BC_{ax}(1-h)\ \overline{(1+\rho^2)^{3/2}}} \tag{6.4}$$

where $\overline{D}$ is the mean drag per unit span dimension

ρ is the dimensionless radius, $= \omega r/U$

h is the hub-tip ratio

and $\overline{(1+\rho^2)^{3/2}}$ is the mean of that quantity over the span.

For h = 0.80, and L/Cax = 1.82, equation (6.4) becomes simply

$$\overline{C_{DB}} = \frac{4.55}{\overline{(1+\rho^2)^{3/2}}} \quad \frac{D_{Total}}{\frac{\sigma_\infty U^2}{2}\pi r_T^2} \tag{6.5}$$

Thus, to compare the experimental values in Fig. 25 with Bryson's data, the quantity $\overline{(1+\rho^2)^{3/2}}$ must be evaluated for each M_T, and the data multiplied by the factor shown in (6.5). Secondly since Bryson's data apply to an airfoil with 12% thickenss ratio, while the data of Fig. 25 apply to blades with a mean thickness ratio of 17.6%, the transonic similarity law must be used to correlate the two sets of data. In the transonic range, the pressure drag coefficient varies as $\delta^{5/3}$ where δ is the thickness ratio. Thus, the experimental values in Fig. 25 must be further multiplied by a thickness factor (T.F) where

$$T\ F = \left(\frac{.12}{.176}\right)^{5/3} = .52 \tag{6.6}$$

Finally, corresponding to each M_T, and the associated $\overline{C_{DB}}$, we must define a corresponding mean free stream relative Mach number, given by

$$\overline{M_\infty} = M\ \overline{(1+\rho^2)^{1/2}} \tag{6.7}$$

where M is the axial Mach number, and $\overline{(1+\rho^2)^{1/2}}$ is the mean of the quantity

over the span. As before, ρ is the dimensionless radius, $= \omega r/U$.

With these considerations, it is now possible to compare Fig. 25 with Bryson's data. This comparison is shown in Fig. 33, and agreement is remarkably good, considering the various approximations involved. This seems to confirm the earlier remarks that the drag rise before $M_T = 1$ is mostly due to the effect of shocks.

For $M_T > 1$ greater difficulties arise in comparing the data with the theory, since the drag shown in Fig. 25 comprises the drag due to shocks, possibly due to shock-boundary layer interactions, the induced drag, and also the wave drag due to thickness and due to the lift on the blades. If we assume that the wave drag build-up does not begin until about $M_T = 1.02$ (the theoretical results justify this assumption), we may regard all of the drag at $M_T = 1.02$ in Fig. 25 as due to the combined effect of shocks and their interaction with the boundary layer, and superpose on this value the calculated values of the wave drag due to thickness shown in Fig. 29. If we also assume that to first order, the variation of this shock and shock-boundary layer drag with Mach number over the Mach number range between 1.02 and 1.11 is negligible compared with the variation of wave drag (a questionable assumption!), then such a plot would represent the total drag build-up in the range $M_T > 1$, provided the only additional drag source in this regime is the wave drag due to thickness. This is also shown in Fig. 25, where it is seen to depart quite markedly from the total measured pressure drag.

A number of remarks must be made about this plot, however. First, as mentioned previously, the data in this regime may have been influenced by the choking of the blade passages mentioned earlier. Since the blade is free wheeling, the pressure field downstream of it differs from what would

be expected in a conventionally driven rotor, and in particular when the passages are choked, the large suction prevailing downstream of the rotor makes it very different from an actual compressor, so that one may expect the drag rise in this regime to be much higher than one would normally obtain in a compressor. Secondly, the induced drag due to lift, which was shown to be relatively negligible in the subsonic regime, might take on increased importance in the low supersonic regime, because of increased three-dimensional effects and the much higher turning angles across the rotor. Finally, the presence of lift on the blades would also result in additional wave drag which must also be taken into account in this regime. Thus a meaningful comparison of the linearised theory cannot be made until the contribution of the lift to both the induced drag and the wave drag are known. Both of the latter can be obtained through further development of the linearised theory.

VII. SUMMARY AND CONCLUSIONS

1. Both static and total pressure measurements behind a free wheeling rotor have demonstrated that the passage from the subsonic to the transonic regime is marked by the occurrence of waves originating from the rotor blades and radiating energy away from the rotor. The interaction of these waves gives rise to a standing wave pattern behind the rotor, and their existence makes three dimensional effects of considerable importance in considerations of transonic flow.

2. It is possible that waves actually do begin to originate at the leading and trailing edges of the blades even before the tip Mach number reaches unity, but since these waves decay very rapidly, no net energy is lost, and the wave drag is zero until the tip Mach number exceeds unity, at which point some of the wave modes can actually propagate outwards to infinity, resulting in wave drag.

3. For tip Mach numbers less than unity, a method has been developed that predicts the induced drag for any given loading distribution, provided this distribution satisfies certain simple boundary conditions at the root and tip. Even for distributions that do not satisfy these conditions, the method still gives satisfactory results except possibly very near the root and tip.

4. The above method shows the induced drag to be finite even in a case when the total lift on the blade is zero, provided only that the circulation changes along the span. Applied to the present experimental rotor, for which the total lift is very nearly zero, it shows that for $M_T < 1.0$, the induced drag is very small compared with the other drag components, and is relatively independent of tip relative Mach number. The measured drag rise for $M_T < 1$, exclusive of the viscous contribution, is shown by comparison with 2-D pressure drag data, to be mostly attributable to the effect of shocks in the passages.

5. The remarkable correlation between the averaged drag measurements for

$M_T < 1$, and Bryson's pressure drag measurements suggests that this might be a suitable means of obtaining pressure drag information from corresponding information obtained from similar two-dimensional profiles, at least in the subsonic regime. Such a correlation may also be used to isolate the effect of shocks from the total measured pressure drag of a blade row in the transonic regime, if information is available on the pressure drag of the isolated airfoil in the same regime.

6. The situation for $M_T > 1$ is complicated by the difficulty of separating the drag due to shocks from the wave drag. In addition to the wave drag due to thickness, there is now both an additional wave drag, and an induced drag due to lift, both of which have not yet been estimated from the linear theory. Although the induced drag was shown to be relatively small for $M_T < 1$, this is not necessarily so for $M_T > 1$ as a result of the increased turning of the fluid. The choking of the blade passages at these Mach numbers also raises some questions as to the relationship of the drag values here to those in an actual unchoked compressor operating in the same range. Comparison of the data with theory in this regime will therefore have to wait until further information can be obtained theoretically as regards the contribution of the lift to the wave drag and the induced drag.

VIII. RECOMMENDATIONS FOR FURTHER WORK

It would be desirable to be able to perform similar experiments with a rotor that would be able to run through the transonic regime without choking the blade passages. This can be achieved with a rotor of lower solidity, or alternately, retaining the same solidity as in the present experiments, but using much thinner blades. To offset the resulting stress problems at the root of the rotor, the scale of the apparatus could be doubled, thereby reducing the rotational speed of the rotor.

It would also be of interest to obtain experimental demonstration of the resonance of the various wave modes by measuring the transient pressures on the walls downstream of the rotor. In this manner, it should be possible to pick up the pressure fluctuations, and thus determine what modes become resonant as the tip relative Mach number is varied.

Analytically, the next logical step is to develop a 3-D lifting surface theory for the transonic regime. Such a theory would be necessary in order to estimate the contribution of the lift to both the induced drag and the wave drag in this region.

REFERENCES

1. Rott, Nicholas - "On Wave Radiation in Compressible Flow through an Axial Compressor" - (Presented at the American Physical Society Meeting at Cornell University in 1951) - American Physical Society, The Physical Review, 84, (1951) Page 613.

2. Lieblein, Lewis and Sandercock - Experimental investigation of an Axial Flow Compressor Inlet Stage Operating at Transonic Relative Inlet Mach Numbers - Over-all Performance of Stage with Transonic Rotor and Subsonic Stator up to Rotor Relative Inlet Mach Number of 1.1 - N. A. C. A. RM E52 A24 (1952).

3. Savage, Melvin, and Felix, Richard A. - Investigation of a High Performance Axial Flow Compressor Transonic Inlet Rotor designed for 37.51bs/sec/ft^2 of frontal area - N. A. C. A. RM L55A05 (1955).

4. Serovy, George K.; Robbins, William H.; and Glaser, Frederick W. - Experimental investigation of a 0.4 Hub Tip Diameter Ratio Axial Flow Compressor Inlet Stage at Transonic Inlet Relative Mach Numbers - I - Rotor Design and Over-all Performance at Tip Speeds From 60 to 100 Percent of Design - N. A. C. A. RM E53 I 11 (1953).

5. Bryson, Jr., A. E. - An Experimental investigation of Transonic Flow past two dimensional Wedge and Circular-arc sections using a Mach-Zehnder Interferometer - N. A. C. A. TN 2560 (1951).

6. Liepmann, Hans Wolfgang; Ashkenas, Harry; and Cole, Julian D - "Experiments in Transonic Flow" - Tech. Rep. No. 5667 - Air Material Command, U. S. Air Force - Feb., 1948.

7. Maeder, P. F. and Thommen, H. U. - "Linearised Transonic Flow About Slender Bodies of Revolution at Zero Incidence" - AFOSR TN 57-384 - July, 1957.

8. Reissner, H. - "On the Relation Between Thrust and Torque Distribution and the Dimensions and the Arrangement of Propeller Blades" - Phil. Magazine - Series7,vol. 24, No. 163 - Nov., 1937.

9. Reissner, H. - "On the Vortex Theory of the Screw Propeller - J. A. S. Vol. 5, No. 1 - Nov., 1937.

10. Davidson, Robert E. - "Linearised Potential Theory of Propeller Induction in a Compressible Flow" - N. A. C. A. TN 2983 (1953).

11. Lepilkin, A. M. - "Vortex Theory of a Lifting Propeller and Mutual Influence of Propellers" - Izv Akad Nank SSSR.

12. Buseman, Adolf - "Theory of the Propeller in Compressible Flow" - Paper presented at the Third Midwestern Conference on Fluid Mechanics - March, 1953.

13. McCune, J. E. - "The 3-D Flow Field of an Axial Compressor Blade Row - Subsonic, Transonic and Supersonic" - Ph.D. Thesis - Cornell University - Feb., 1958.

14. McCune, J. E. - "The Transonic Flow Field of an Axial Compressor Blade Row" - Journal of Aeronautical Sciences - 25, 616-626 (1958)

15. Thommen, H. U. - "On Transonic Flow About Three Dimensional Bodies" - AFOSR TN 58-714 (1958).

16. Ferrari, Carlo - "On Non-Steady Transonic Flows Past Symmetrical Airfoils" - AFOSR TN 58-321.

17. Herzig, H. Z. and Hansen, A. G. - "Three-dimensional Compressor Flow Theory and Real Flow Effects - N. A. C. A. RM E56B03b (1956).

18. Swan, W. C. - "An Experiment with Aspect Ratio as a Means of Extending the Useful Range of a Transonic Inlet Stage of an Axial Flow Compressor" - Trans. ASME - 86A (Journal of Engineering Power) - 243-246 - July, 1964.

19. Wennerstrom, Arthur J. - "Simplified Design Theory for Highly Loaded Axial Compressor Rotors and Experimental Study of Two Transonic Examples" - Thesis for Doctor of Tech. Sci. - Swiss Federal Inst. of Tech., Zurich - (1965).

20. Andrews, S. J. - "Tests Related to the Effects of Profile Shape and Camber Line on Compressor Cascade Performance" - Rep. No. R60 - British N. G. T. E. Oct., 1949.

21. Kaplan, C. - "The Flow of a Compressible Fluid Past a Circular Arc Profile" - N. A. C. A. Rep. No. 994 - (1944).

22. Goldstein, Sydney - "On the Vortex Theory of Screw Propellers" - Proceedings, Royal Soc. (London) - Ser. A, Vol. 123, No. 792 - April 6, 1929 - pp. 440-465.

23. Kawada, Sandi - "Induced Velocity by Helical Vortices" - Journal of Aeronautical Sciences - Vol. 3, No. 3 - January, 1936 - Page 86.

24. Watson, G. N. - A Treatise on the Theory of Bessel Functions - second ed. - The MacMillan Company - (1944).

25. Ippen, Arthur T. - "The Influence of Viscosity on Centrifugal Pump Performance" - Annual Meeting ASME in New York - November 27, 1945.

26. Nicholson, J. W. - "The Approximate Calculation of Bessel Functions of Imaginary Argument" - Phil. Mag. - Series 6, Vol. 20 - pp. 938-943.

APPENDIX A - WAVE DRAG DUE TO THICKNESS - McCunes Results

The basic differential equation (5.4) has particular solutions of the form:

$$\phi^{u,d}_{nk} = A^{u,d}_{nk} \exp\left\{inB\theta + \left(\frac{inBM}{\beta^2} \pm \lambda^{o,e}_{nk}\right) z\right\} R_{nB}\left(K_{nBK} \frac{\rho}{\rho_T}\right) \qquad (A.1)$$

where B = number of blades

and

$$\lambda_{nk} = \frac{1}{\beta}\sqrt{\frac{K^2_{nk}}{\rho^2_T} - \frac{n^2B^2M^2}{\beta^2}}$$

The superscripts e, o denote real and imaginary values of λ_{nBk} respectively, and R_{nB} are normalized linear combinations of Bessel and Newmann functions. The superscripts u, d refer to upstream and downstream solutions respectively. The choice of sign for $\lambda^{o,e}_{nk}$ is made differently upstream and downstream in such a manner that (i) the perturbation velocities are bounded at infinity in both directions, and (ii) in the case of imaginary values of λ_{nk}, the waves have a higher frequency in the axial direction upstream than downstream. The eigenvalues K_{nBk} are obtained from the condition that the radial velocities vanish at the hub and shroud, and are the solutions of the equation:

$$\frac{J'_{nB}(K_{nBk}h)}{N'_{nB}(K_{nBk}h)} = \frac{J'_{nB}(K_{nBk})}{N'_{nB}(K_{nBk})} \qquad (A.2)$$

The functions R_{nB} are defined by

$$R_{nB}(x) = \frac{1}{N_{nBk}}\left[J_{nB}(x) - \frac{Y_{nBk}}{\sqrt{3}} N_{nBk}(x)\right] \equiv \frac{Y_{nB}(x)}{N_{nBk}} \qquad (A.3)$$

where J_{nB} is the Bessel Function of the first kind of order nB, N_{nB} is the

corresponding Bessel Function of the second kind, or the Newmann Function; and γ_{nBk} is the shift in phase of the function J_{nB} with respect to the cylinder function R_{nB}.

The normalizing factor N_{nBk} ensures that the set of functions R_{nB} are orthonormal, and is given by

$$N_{nBk} = \frac{1}{\sqrt{2}} \left[Y_{nB}^2(K_{nBk})(1 - \frac{n^2B^2}{K_{nBk}^2}) - h^2 Y_{nB}^2(hK_{nBk})(1 - \frac{n^2B^2}{h^2K_{nB}^2}) \right]^{1/2} \qquad (A.4)$$

while the phase shifts are given by:

$$\gamma_{nBk} = \sqrt{3} \frac{J'_{nB}(K_{nBk})}{N'_{nB}(K_{nBk})}$$

From these particular solutions, elemental source singularities of strength $q(r)$ are built up in such a way that the mass introduced by the singularities at $z = o$ equals the mass discontinuity resulting from the upstream and downstream solutions. In this manner, the coefficients A^{u}_{nk} are related to the source strength distribution $q(\rho)$. These elemental singularities themselves are then distributed over the approximately helical surfaces of the blades, and the blade profile related to the local discontinuity in velocity normal to each helical sheet approximating the blades. The final expression for the solution has the form:

$$\phi^i - \phi^i_o = - \frac{UB\tau_o h^2}{\pi\beta^2 \sin \phi_H} \sum_{n=1}^{\infty} \sum_{k=1}^{\infty} \frac{Q^*_{nBk} R_{nB}(K_{nBk}\eta)}{\lambda^{o,e}_{nBk}} S_{nBk}(z, \theta; C_{ax}) \qquad (A.5)$$

where $S_{nBk}(z,\theta;C_{ax}) = e^{inB(\theta + \frac{z}{\rho_s^2})} \int_o^{C_{ax}} \frac{g(\xi)}{2U} \exp\{-\frac{inB\omega\xi}{U\beta^2}\} e^{-\lambda_{nBk}\left|z - \frac{\omega\xi}{U}\right|} d\xi$

and ϕ^i_o is the term corresponding to $n = 0$.

The superscript i denotes the region between blade rows, and Q^*_{nk} are coefficients, depending only on the geometry of the blade row. For a blade row with 40 blades of double parabolic arc profiles, and a hub-tip ratio of 0.80, these coefficients are listed in Table 1. The function $g(\xi)$ is related to the slope of the blade surface in the chordwise direction, and is given as:

$$g(\xi) = 4U(1 - \frac{2\xi}{C_{ax}}) \tag{A.6}$$

The thickness distribution of the blades is assumed to be of the form:

$$\tau(\rho) = \frac{\tau_o h \sqrt{1+\rho_H^2}}{\eta \sqrt{1+\eta^2\rho_T^2}} \tag{A.7}$$

where τ_o is the thickness to chord ratio at the hub.

In evaluating (A.5), we are primarily interested in the pressures on the blades. Thus, if we assume the blade chord to lie in the direction of the helix of advance of the air (i.e. zero angle of attack) we may in (A.5) set $\theta = z$ and evaluate $(\phi_i - \phi_o^i)$ on the blades. The velocities on the blades are then obtained by numerical differentiation of ϕ along the blade chord. The local pressure coefficient on the blade is then given by

$$C_p(\eta,x) = -\frac{2}{U}\sqrt{1+\rho^2}\,\frac{\partial \phi^i}{\partial X} \tag{A.9}$$

where x is distance measured in the axial direction and X is distance measured in direction of blade chord. The value of C_p includes a contribution due to ϕ_o^i which may be evaluated in the approximate form:

$$\phi^i_{ox} = \frac{1}{2L\beta^2}\left\{ \int_o^x f(\rho,\xi)\,\frac{d\xi}{\cos\phi} - \int_x^{C_{ax}} f(\rho,\xi)\,\frac{d\xi}{\cos\phi} \right\} \tag{A.10}$$

where $L = \frac{2\pi r_T}{B}$

and $f(\rho,\xi) = g(\xi)\,\tau(\rho)$

Thus, using (A.6) and (A.7), and integrating (A.10), we may express ϕ^i_{ox} in the form

$$\phi^i_{ox} = \frac{2BU\,\tau_o \rho_H \sqrt{1+\rho_H^2}}{\pi\beta^2 r_T \rho}\,(x - \frac{x^2}{C_{ax}}) \tag{A.11}$$

and hence,

$$C_{po}(\eta,x) = -\frac{4B}{\pi\beta^2 r_T}\,\tau(\eta)\sqrt{1+\eta^2\rho_T^2}\,(x - \frac{x^2}{C_{ax}}) \tag{A.12}$$

The drag on the blade is obtained by integrating the pressures over the blade surface:

$$C_D(\eta) = \frac{D(\eta)}{\frac{\sigma_\infty U^2 C_{ax}}{2}} = \int_o^1 C_p(\eta,x)\,\frac{f(\eta,x)}{U}\,d(\frac{x}{C_{ax}}) \tag{A.13}$$

It may be verified directly by integration of (A.12) over the blade surface that, for blades of the form specified in (A.6) the ϕ^i_o term does not contribute to the drag on the blades.

The total wave drag coefficient per blade is finally obtained by spanwise integration:

$$C_{DW} = \int_h^1 C_D(\eta)\,d\eta \tag{A.14}$$

In evaluating the Bessel Functions and their derivatives, use is made of assymptotic expansions for these functions valid in the transitional regions. The formulae for these functions may be found in reference 13.

APPENDIX B: COMPUTER PROGRAMS

Part I - Programs used in Parts II and III

```
C     SUBROUTINE TO INTEGRATE.ADJUSTS INTEGRATION STEP SIZE
C     TO KEEP FRACTIONAL ERROR TO WITHIN SPECIFIED TOLERANCE.
C
C
      SUBROUTINE  RUNGE(N, X, Y, TOL, YMIN, H, XOUT, MARK)
      DIMENSION  Y(1), YMIN(1), TOL(1), SUB(50), XOUT(1), MARK(1)
      DIMENSION  DY(50), YA(50), FA(50), FB(50), FC(50), YKEEP(50)
      KBTWN = 1
      KBIG = 1
      KLOW = 1
      NCOUNT = 15
      J = MARK(1)
      MAX = MARK(2)
230   DO 250  I = 1, N
250   SUB(I) = TOL(I)/32.0
10    IF (MAX - J)  20, 30, 30
20    RETURN
30    A = XOUT(J) - X
      B=ABSF(1.E-6*X)
      IF (A + B)  40, 35, 35
35    IF (A - B)  50, 50, 60
40    J = J + 1
      GO TO 10
50    CALL PRINT(N, XOUT, Y, DY, J)
      J = J + 1
      GO TO 10
60    IF (A - 1.5*H)  70, 70, 80
70    H = A
      GO TO 1000
80    IF (A - 3.*H)  90, 1000, 1000
90    H = .5*A
C
C          DO RUNGE-KUTTE-MERSON INTEGRATION
C
1000  XA = X + H/3.
      XB = X + .5*H
      CALL DIFFEQ(N, X, Y, DY)
      X = X + H
      DO 1030  I = 1, N
      YKEEP(I) = Y(I)
      FA(I) = H*DY(I)
1030  YA(I) = Y(I) + FA(I)/3.
      CALL DIFFEQ(N, XA, YA, DY)
      DO 1040  I = 1, N
1040  YA(I) = Y(I) + FA(I)/6. + H*DY(I)/6.
      CALL DIFFEQ(N, XA, YA, DY)
      DO 1050  I = 1, N
      FB(I) = H*DY(I)
1050  YA(I) = Y(I) + .125*FA(I) + .375*FB(I)
      CALL DIFFEQ(N, XB, YA, DY)
```

```
      DO 1060  I = 1, N
      FC(I) = H*DY(I)
1060  YA(I) = Y(I) + .5*FA(I) - 1.5*FB(I) + 2.*FC(I)
      CALL DIFFEQ(N, X, YA, DY)
      DO 1130  I = 1, N
      Y(I) = Y(I) + FA(I)/6. + .666666667*FC(I) + H*DY(I)/6.
1061  U = Y(I)
      IF (ABSF(U) - YMIN(I))  1130, 1090, 1090
1090  KLOW = 2
      E = .2*ABSF(U - YA(I) )
      IF ( E - ABSF(TOL(I)*U) )  1110, 1100, 1100
1100  KBIG = 2
      GO TO 1130
1110  IF ( E - ABSF(SUB(I)*U) )  1130, 1120, 1120
1120  KBTWN = 2
1130  CONTINUE
      GO TO (100, 1135), KLOW
1135  GO TO (1180, 1140), KBIG
1140  NCOUNT = NCOUNT - 1
      IF (NCOUNT) 1150, 1150, 1170
1150  PRINT 1160,  X, H
      PRINT 1165, (I, Y(I), DY(I),  I = 1, N)
      RETURN
1160  FORMAT (58H4STEP SIZE HALVED 15 TIMES CONSECUTIVELY SINCE LAST PRI
     1NT  /29H PROGRAM TERMINATED AT   X =  , E16.8, 8H,   H = , E16.8,
     2//3H  I , 13X, 4HY(I), 16X, 5HDY(I),//)
1165  FORMAT (I3, 7X, 2(F16.8, 4X))
1170  KBIG = 1
      IF (H - B)  1176, 1172, 1172
1172  X = X - H
      H = .5*H
      DO 1174  I = 1, N
1174  Y(I) = YKEEP(I)
      KBTWN = 1
      KLOW = 1
      GO TO 1000
1176  M = 15 - NCOUNT
      PRINT 1178, M, X, H
      PRINT 1165, (I, Y(I), DY(I), I = 1, N)
      RETURN
1178  FORMAT (41H4STEP SIZE BECAME TOO SMALL FOR COMPUTER./20H IT HAS BE
     1EN HALVED , I2, 21H TIMES CONSECUTIVELY./29H PROGRAM TERMINATED AT
     2   X =  , E16.8, 8H,   H = , E16.8,//3H  I, 13X, 4HY(I), 16X,
     35HDY(I),//)
1180  NCOUNT = 15
      GO TO (1190, 1200), KBTWN
1190  H = 2.*H
1200  KBTWN = 1
      KLOW = 1
C
C          CHECK FOR INTERMEDIATE PRINT OUT
C
 100  GO TO 10
 130  FORMAT (5H X = , F16.8, 4X, 4HH = , E16.8, 11X, 1HI, 13X, 4HY(I),
```

```
     116X, 5HDY(I)/)
140   FORMAT (55X, I3, 7X, 2(E16.8, 4X))
      END



      SUBROUTINE PRINT (L,XOUT,Y,DY,J)
      DIMENSION XOUT(2),Y(5),DY(5),B(10),B2(10)
      RETURN
      END



      FUNCTION ABSF (X)
      ABSF=X
      IF (X) 1,1,2
1     ABSF=-X
2     RETURN
      END
```

Part II - Wave Drag Due to Thickness

```
C       SUBROUTINE TO COMPUTE BESSEL FUNCTIONS OF ORDER 1/3
        SUBROUTINE BESS3 (X,B)
        DIMENSION B(10),G(10)
C      B1= J 1/3,  B2 = J -1/3,  B3 = I 1/3,  B4 = I -1/3,
C      B5 = CAP H,  B6 = CAP D,  B7 = H,  B8 = D
C       CAP H=I-1/3 +I1/3 ,  CAP D=I-1/3 -I1/3
C       H=J-1/3+J1/3  , D=J-1/3-J1/3
C       FOR ARG LESS THAN OR EQUAL TO 3.4,USE POWER SERIES
C       EXPANSION, TAKING FIRST 10 TERMS. FOR ARG GREATER THAN
C       3.4, USE ASSYMPTOTIC EXPANSION.
   10   IF(X-3.4)2,2,3
 2      FX=(.5*X)**.3333333
        G(1)=FX/.8934
        G(2)=1./(FX*1.3525)
        G(3)=G(1)
        G(4)=G(2)
        DO 20 K=1,4
 20      B(K)=G(K)
        DO 21 K=1,10
        FAC1=(X*.5)**2/(K*(K+ .333333))
        FAC2 =(X*.5)**2/(K*(K-.3333333))
        G(1)=-FAC1*G(1)
        G(2)=-FAC2*G(2)
        G(3)=FAC1*G(3)
        G(4)=FAC2*G(4)
        IF (G(4)-1.E-10) 40,40,30
 30     DO 21 L=1,4
 21     B(L)=B(L)+G(L)
        GO TO 40
 3      PIE=3.14159
        AA=1.-(4./9.-1.)*(4./9.-9.)/(128.*X**2)+(4./9.-1.)*(4./9.-9.)
       1*(4./9.-25.)*(4./9.-49.)/(24.*4096.*X**4)
        AB=(4./9.-1.)/(8.*X)-(4./9.-1.)*(4./9.-9.)*(4./9.-25.)/(3072.
       1*X**3)
        AC =SQRT (2/(PIE*X))
        XX=X-5./12.*PIE
        B(1)=AC*(AA*COS(XX)-AB*SIN(XX))
        XX=X-1./12.*PIE
        B(2)=AC*(AA*COS(XX)-AB*SIN(XX))
        AD=1.-(4./9.-1.)/(8.*X)+(4./9.-1.)*(4./9.-9.)/(128.*X**2)
       1-(4./9.-1.)*(4./9.-9.)*(4./9.-25.)/(3072.*X**3)
       2+(4./9.-1.)*(4./9.-9.)*(4./9.-25.)*(4./9.-49.)/(24.*4096.*X**4)
        B(3)=AC*AD*EXP(X)/2.
        B(4)=B(3)
 40      B(5)=B(4)+B(3)
        B(6)=B(4)-B(3)
```

```
      IF(X-3.4) 13,15,14
   13 IF(X-2.)14,14,15
   15 B(6)=B(6)*(4.8-X)/2.8
   14 CONTINUE
      B(7)=B(2)+B(1)
      B(8)=B(2)-B(1)
      RETURN
      END



C     SUBROUTINE TO COMPUTE BESSEL FUNCTIONS OF ORDER N AND
C     ARG R IN THE TRANSITIONAL REGIONS.
      SUBROUTINE BESSEL (N,R,XA,XB,ALA,ALB,B)
      DIMENSION B(10),BA(10),BB(10)
C     B(1)=JN(R), B(2)=NN(R), B(3)=JNP(R), B(4)=NNP(R)
      S3=SQRT(3.)
      IF (R-N) 1,1,2
 1    SECHA =R/N
      SECHB=R/(N+1)
      PI=3.14159
      TANHA=SQRT(-SECHA**2+1.)
      TANHB=SQRT(-SECHB**2+1.)
      XA=N/3.*TANHA**3
      XB = (N+1)/3.*TANHB**3
      CALL BESS3 (XA,BA)
      CALL BESS3 (XB,BB)
      ALA=ALOG(1./SECHA*(1.+TANHA))
      ALB=ALOG(1./SECHB*(1.+TANHB))
      IF((N*(TANHA-ALA)+XA)**2-500.) 3,3,4
    4 PRINT5,N,R
    5 FORMAT(20H OVERFLOW IN BESSEL  ,I5,F15.2)
      RETURN
    3 EXPA=EXP(N*(TANHA-ALA)+XA)
      EXPB = EXP((N+1)*(TANHB-ALB)+XB)
      B(1)=TANHA/3*EXPA*BA(6)
      B(2)=-TANHA/(S3*EXPA)*BA(5)
      B(3)=EXPA/(SECHA*3)*BA(6)*TANHA-TANHB/3.*EXPB*BB(6)
      B(4)=-BA(5)/(SECHA*S3*EXPA)*TANHA+TANHB*BB(5)/(S3*EXPB)
      RETURN
C     FOR R GREATER THAN N
 2    SECA =R/N
      TANA=  SQRT(SECA**2-1)
      SECB=R/(N-1)
      TANB =   SQRT(SECB**2-1)
      XA=N/3.*TANA**3
      XB=(N-1)/3.*TANB**3
      BETA =ATAN(TANA)
      BETB =ATAN(TANB)
      ALA=BETA
      ALB=BETB
```

```
      ARGA=N*(TANA-BETA)-XA
      ARGB=(N-1)*(TANB-BETB)-XB
      NA=ARGA/(2.*PI)
      NB=ARGB/(2.*PI)
         ARGA=ARGA-NA*2.*PI
         ARGB=ARGB-NB*2.*PI
      SINA=SIN(ARGA)
      COSA=COS(ARGA)
      SINB=SIN(ARGB)
      COSB=COS(ARGB)
      CALL BESS3 (XA,BA)
      CALL BESS3 (XB,BB)
      B(1)=TANA/3*COSA*BA(7)        +TANA/S3*SINA*BA(8)
      B(2)=TANA/3.*SINA*BA(7)-TANA/S3*COSA*BA(8)
      B(3)=TANA/SECA*(-COSA*BA(7)/3.-SINA*BA(8)/S3)
     1 +TANB/3.*COSB*BB(7)+TANB/S3*SINB*BB(8)
      B(4)=TANA*SECA*(-SINA*BA(7)/3.+COSA*BA(8)/S3)
     1 +TANB/3.*SINB*BB(7)-TANB/S3*COSB*BB(8)
      RETURN
      END
```

```
C     SUBROUTINE TO COMPUTE INTEGRANDS
      SUBROUTINE DIFFEQ (L,X,Y,DY)
      COMMON N,R,M
      DIMENSION Y(5),DY(5),B(10)
      CALL BESS3 (X,B)
      S3=SQRT(3.)
      DO 4 I=1,5
    4 DY(I)=0.
      TAN=(3.*X/N)**.3333333
      GO TO (1,2),M
    1 AL=ATAN(TAN)
      ARG1=N*TAN-N*AL-X
      DY(1)=(B(7)/S3*COS(ARG1)+B(8)*SIN(ARG1))/(1.+TAN**2)
      DY(2)=(B(7)/S3*SIN(ARG1)-B(8)*COS(ARG1))/(1.+TAN**2)
      RETURN
    2 SECH=SQRT(-TAN**2+1.)
      ALH=ALOG(1./SECH*(1.+TAN))
      ARG2=N*TAN-N*ALH+X
      DY(3)=EXP(ARG2)*B(6)/(1.-TAN**2)
      DY(4)=-EXP(-ARG2)*B(5)/(1.-TAN**2)
    8 RETURN
      END
```

```
C       PROGRAM TO EVALUATE RADIAL EIGENVALUES KNK AND CHARACTERISTIC
C       BLADE COEFFICIENTS QNK*
        COMMON N,R,Z,HUB
        DIMENSION B(10),B2(10)
        READ 5,NB,HUB
    4   READ 20,MM,XSTART,XEND,DX
        N=MM*NB
        L=0
        DIF=0
        PRINT 20,N,XSTART,XEND,DX
        M=(XEND-XSTART)/DX+2
        DO45 I =1,M
        DIFH=DIF
        X=XSTART+(I-1)*DX
        X2=HUB*X
        CALL BESSEL (N,X2,XA2,XB2,ALA2,ALB2,B2)
        CALL BESSEL (N,X,XA,XB,ALA,ALB,B)
        DIF=B(4)*B2(3)-B2(4)*B(3)
        IF(DIF*DIFH) 40,45,45
   40   L=L+1
        R=X-DIF*DX/(DIF-DIFH)
        CALL INT
C       FIND ONLY THE FIRST 20 SOLUTIONS LESS THAN UPPER
C       VALUE OF X
        IF(L-20)45,4,4
   45   CONTINUE
        GO TO 4
   20   FORMAT(I5,5X,3F10.3)
    5   FORMAT(I5,3X,F4.2)
        END
```

```
C       SUBROUTINE TO EVALUATE INTEGRALS RELEVANT TO QNK*
        SUBROUTINE INT
        COMMON N,R,M,HUB
        DIMENSION B(10),Y1(5),Y2(5),MARK(5),YMIN(5),TOL(5),XOUT(2)
       1,B2(10) ,DY(5)
        S3=1.732
        PRINT11,N,R
        SECB=R/N
        TANB=SQRT(SECB**2-1.)
        M=1
        XOUT(1)=N/3.*TANB**3
    2   MARK(1)=1
        MARK(2)=1
        MARK(3)=0
        MARK(4)=1
        H=.01
        X1=.001
        X2=.001
```

```
      CALL DIFFEQ (4,X1,Y1,DY)
      PRINT19,X1,DY
      DO 3 I=1,5
      YMIN(I)=.0001
      TOL(I)=.0001
      Y1(I)=0.
3     Y2(I)=0.
      CALL RUNGE (4,X1,Y1,TOL,YMIN,1,XOUT,MARK)
      PRINT12,X1,Y1
      TAN2=HUB**2*SECB**2-1.
      IF (TAN2)  4,4,5
4     TAN2=-TAN2
      M=2
5     XOUT(1)=N/3.*TAN2**1.5
      H=.01
      CALL DIFFEQ (4,X2,Y2,DY)
      PRINT19,X2,DY
      CALL RUNGE (4,X2,Y2,TOL,YMIN,H,XOUT,MARK)
      PRINT13,X2,Y2
      CALL BESSEL (N,R,XA,XB,ALA,ALB,B)
      SECA=HUB*SECB
      R2=SECA*N
      CALL BESSEL (N,R2,XA2,XB2,ALA2,ALB2,B2)
      TAND=B2(3)/B2(4)
      GAMMA=S3*TAND
      YNB=B(1)-GAMMA/S3*B(2)
      YNB2 =B2(1)-GAMMA/S3*B2(2)
      FACN=((YNB**2*(1.-1./SECB**2)+HUB**2*YNB2**2*(1./SECA**2-1.))
     1 /2.)**.5
      GO TO (6,7),M
6     YINT=(Y1(1)/S3-GAMMA*Y1(2)/3.-Y2(1)/S3+GAMMA*Y2(2)/3.)/N
      GO TO 10
7     YINT=(Y1(1)/S3-GAMMA*Y1(2)/3.+Y2(3)/3.-GAMMA/3.*Y2(4))/N
10     Q=YINT/FACN
      PRINT14,Q,YINT,FACN
      PRINT 15,GAMMA,B(3),B(4),B2(3),B2(4)
      RETURN
   11 FORMAT(4H N =,I5,21X,4H R =,E16.5 )
12     FORMAT (5H X1 =,E15.4,10X,7H S(I) =,E13.4,4E15.4 )
13     FORMAT (5H X2 =,E15.4,10X,7H S(I) =,E13.4,4E15.4 )
14     FORMAT (4H Q =,E16.4,10X,5H INT ,E15.4,10X,6H NNK =,F14.4,///)
19     FORMAT (7H AT X =,F10.3,5H DY =,5E15.4)
   15 FORMAT(5F12.4)
      END
```

```
C     SUBROUTINE TO COMPUTE AXIAL DEPENDENCE FUNCTION SNK
C     L=1, LAMBDA REAL,   L=2, LAMBDA IMAGINARY
      SUBROUTINE INT(ALPHA,DELTA,Z,W,U,AL,F1,F2,F6,CAX,SNK,L)
      GO TO (42,43),L
```

```
42 F3=AL**2+F2**2
   F4=EXP(-AL*Z)
   IF(ABSF(F4)-1.0E-60)46,46,47
46 F4=0.
47 F5=EXP(-AL*(W*CAX/U-Z))
   IF(ABSF(F5)-1.0E-60)48,48,49
48 F5=0.
49 A1=((COS(F1)-F4)*AL+F2*SIN(F1))/F3
   B1=(F2*(COS(F1)-F4)-AL*SIN(F1))/F3
   ALPH2=F5*COS(F6)-COS(F1)
   GAM2=SIN(F1)-F5*SIN(F6)
   A2=(AL*ALPH2+F2*GAM2)/F3
   B2=(AL*GAM2-ALPH2*F2)/F3
   ALPH3=2.*U*Z/W*COS(F1)-2.*U*AL*COS(F1)/(W*F3)
  1-2.*U*F2*SIN(F1)/(W*F3)+2.*F4*U*AL/(W*F3)
   GAM3=-2.*U*Z*SIN(F1)/W+2.*U*AL*SIN(F1)/(W*F3)
  1-2.*U*F2*COS(F1)/(W*F3)+2.*F4*U*F2/(W*F3)
   A3=(AL*ALPH3-GAM3*F2)/(CAX*F3)
   B3=(AL*GAM3+ALPH3*F2)/(CAX*F3)
   ALPH4=2.*F5*COS(F6)*(CAX+U*AL/(W*F3))
  1-2.*F5*SIN(F6)*U*F2/(W*F3)-2.*U*Z*COS(F1)/W
  2-2.*U*AL*COS(F1)/(W*F3)+2.*U*F2*SIN(F1)/(W*F3)
   GAM4=-2.*F5*COS(F6)*U*F2/(W*F3)-2.*F5*SIN(F6)*(CAX+U*AL/(W*F3))
  1+2.*U*F2*COS(F1)/(W*F3)+2.*SIN(F1)*(U*Z*1./W+U*AL/(W*F3))
   A4=(AL*ALPH4+GAM4*F2)/(CAX*F3)
   B4=(GAM4*AL-ALPH4*F2)/(CAX*F3)
   SNK=ALPHA*(A1-A2-A3+A4)-DELTA*(B1-B2-B3+B4)
   GO TO 41
43 ALPH1=COS(F1)-COS(AL*Z)
   GAM1=SIN(AL*Z)-SIN(F1)
   F7=AL-F2
   A1=GAM1/F7
   B1=-ALPH1/F7
   F8=AL*(W*CAX/U-Z)+F6
   ALPH2=COS(F8)-COS(F1)
   GAM2=SIN(F1)-SIN(F8)
   F9=AL+F2
   A2=GAM2/F9
   B2=-ALPH2/F9
   ALPH3=2.*U*Z/W*COS(F1)+2.*U*SIN(F1)/(W*F7)
  1-2.*U*SIN(AL*Z)/(W*F7)
   GAM3=2.*U*COS(F1)/(W*F7)-2.*U*Z*SIN(F1)/W-2.*U*COS(AL*Z)/(W*F7)
   A3=GAM3/(CAX*F7)
   B3=-ALPH3/(CAX*F7)
   ALPH4=2.*CAX*COS(F8)-2.*U*SIN(F8)/(W*F9)
  1-2.*U*Z*COS(F1)/W+2.*U*SIN(F1)/(W*F9)
   GAM4=-2.*U*COS(F8)/(W*F9)-2.*CAX*SIN(F8)+2.*U*COS(F1)/(W*F9)
  1+2.*U*Z*SIN(F1)/W
   A4=GAM4/(CAX*F9)
   B4=-ALPH4/(CAX*F9)
   SNK=ALPHA*(B1-B2-B3+B4)+DELTA*(A1-A2-A3+A4)
41 RETURN
   END
```

```
C       MAIN PROGRAM FOR PHI AND CD
        DIMENSION N(10),KEND(20),R(10,20),Q(10,20),ALAM(10,20),
       1L(10,20),X(81),SNK(10,20,81),ETA(21),B(10),B2(10),RNK(10,20,
       221),PHI(21,81),TAU(21),G(81),CP(21,81),DCD(21,81),CD(21),
       3DPHI(21,81),CPO(21,81),PRODH(10,20),PRODT(10,20)
        READ8, HUB, BLADE
        READ 51,RE
        PRINT 11, HUB, BLADE
        PRINT 52, RE
C       READ N R AND Q
        DO 3 I=1,10
        READ 2,N(I),KEND(I),(R(I,J),Q(I,J),J=1,20)
        PRINT4
    3   PRINT 2,N(I),KEND(I),(R(I,J),Q(I,J),J=1,20)
        READ20,NN,DETA,NX,DX
        PRINT22,NN,DETA,NX,DX
  100     CONTINUE
        READ1,AM,RPS,RT,TEMP,CAX,TAU0,AMT
        PRINT40,AM,RPS,RT,TEMP,CAX,TAU0,AMT
        TAU0=TAU0
        BETA=SQRT(1.-AM**2)
        RHOS=BETA/AM
        T=TEMP/(1.+.2*AM**2)
        U=1.
        PHIT=ATAN(SQRT(AMT**2-AM**2)/AM)
        RHOT=TAN(PHIT)
        PHIH=ATAN(HUB*RHOT)
        W=RHOT/RT
        EPSI=1.3333*RHOT/(RHOS*RE)
C       CALC LAMDA AND L
        DO 6 I=1,10
        KE=KEND(I)
        DO 6 J=1,KE
        GNK=(R(I,J)/N(I))**2-(RHOT/RHOS)**2
        IF (GNK) 7,9,9
C       LAMDA IMAG
    7   ALAM(I,J)=N(I)/(BETA*RHOT)*SQRT(-GNK)
        L(I,J)=2
        GO TO 6
C       LAMDA REAL
    9   ALAM(I,J)=N(I)/(BETA*RHOT)*SQRT(GNK)
        L(I,J)=1
    6   CONTINUE

C       CALCULATE SNL/LAMDA
        DO 10 K=1,NX
        X(K)=-DX+DX*K
        Z=W*X(K)/U
        DO 10 I=1,10
```

```
      KE=KEND(I)
      F1=N(I)*Z/BETA**2
      F2=N(I)/BETA**2
      ALPHA=2.*U/W*COS(F1)
      F6=N(I)*W*CAX/(U*BETA**2)
      DELTA=2.*U/W*SIN(F1)
      DO 10 J=1,KE
      CALL INT(ALPHA,DELTA,Z,W,U,ALAM(I,J),F1,F2,F6,CAX,SNK(I,J,K),
     1L(I,J))
   10 SNK(I,J,K)=SNK(I,J,K)/ALAM(I,J)

C     COMPUTE RN
      DO 12 I=1,10
      KE=KEND(I)
      DO 12 J=1,KE
      CALL BESSEL (N(I),R(I,J),XA,XB,ALA,ALB,B)
      ETAR=HUB*R(I,J)
      CALL BESSEL (N(I),ETAR,XA,XB,ALA,ALB,B2)
      TAND=B2(3)/B2(4)
      YNB=B(1)-TAND*B(2)
      YNB2=B2(1)-TAND*B2(2)
      ENNK=((YNB**2*(1.-(N(I)/R(I,J))**2)+HUB**2*((N(I)/(HUB*R(I,J)))
     1**2-1.)*YNB2**2)/2.)**.5
      DO 12 K=1,NN
      ETA(K)=HUB-DETA+DETA*K
      ETAR=ETA(K)*R(I,J)
      CALL BESSEL (N(I),ETAR,XA,XB,ALA,ALB,B2)
      YNB2=B2(1)-TAND*B2(2)
   12  RNK(I,J,K)=YNB2/ENNK
C     COMPUTE PHI
      PHIFAC=-U*BLADE*TAUO*HUB**2/(3.14159*BETA**2*SIN(PHIH))
      DO 13 KN=1,NN
      DO 13 KX=1,NX
      PHI(KN,KX)=0.
      DO 121 I=1,10
      KE=KEND(I)
      DO 121J=1,KE
  121  PHI(KN,KX)=PHI(KN,KX)+Q(I,J)*RNK(I,J,KN)*SNK(I,J,KX)
   13  PHI(KN,KX)=PHI(KN,KX)*PHIFAC
      PRINT 55,X(5)
      KE=KEND(10)
      PRINT 53,(SNK(10,J,5),RNK(10,J,1),J=1,KE)
      PRINT 54,(SNK(I,1,5),RNK(I,1,1),I=1,20)
      DO 57 I=1,10
      KE=KEND(I)
      DO 57 J=1,KE
      PRODH(I,J)=Q(I,J)*RNK(I,J,1)*SNK(I,J,5)
   57 PRODT(I,J)=Q(I,J)*RNK(I,J,21)*SNK(I,J,5)
      DO 59 I=1,10
      PRINT 58,I
      KE=KEND(I)
      PRINT 56,(PRODH(I,J),J=1,KE)
   59 PRINT 60,(PRODT(I,J),J=1,KE)
C     COMPUTEDPHI   CP   TAU   G
```

```
      DO 15 KN=1,NN
      DCAPX=2.*DX*SQRT(1.+(W*ETA(KN)*RT/U)**2)
      DO 14 KX=1,NX
   14  DPHI(KN,KX)=(PHI(KN,KX+1)-PHI(KN,KX-1))/DCAPX
      DPHI(KN,1)=2.*(PHI(KN,2)-PHI(KN,1))/DCAPX
   15  DPHI(KN,NX)=2.*(PHI(KN,NX)-PHI(KN,NX-1))/DCAPX

      PRINT29
C     COMPUTE CP          TAU     G
      RHOH=HUB*RHOT
      DO 16 KN=1,NN
      DO 16 KX=1,NX
      TAU(KN)=TAU0*HUB/ETA(KN)*SQRT((RHOH**2+1.)
     1  /((ETA(KN)*RHOT)**2+1.) )
      G(KX)=4.*U*(1.-2.*X(KX)/CAX)
      CP(KN,KX)=-2./U*SQRT(1.+(ETA(KN)*RHOT)**2)*DPHI(KN,KX)
      CP0(KN,KX)=-4.*BLADE*TAU(KN)*SQRT(1.+(ETA(KN)*RHOT)**2)*(X(KX)
     1-X(KX)**2/CAX)/(3.1416*BETA**2*12.*RT)
      CP(KN,KX)=CP(KN,KX)+CP0(KN,KX)
      DCD(KN,KX)=CP(KN,KX)*G(KX)*TAU(KN)/(U*CAX)
   16  CONTINUE
      DO 161 KN=1,NN,5
      DO 161 KX=1,NX
  161 PRINT 28,X(KX),ETA(KN),PHI(KN,KX),DPHI(KN,KX),DCD(KN,KX),CP(KN,KX)
C     COMPUTE  CD
      DO 17 KN=1,NN
      CD(KN)=0.
      DO 18 KX=1,NX
   18  CD(KN)=CD(KN)+DCD(KN,KX)
   17  CD(KN)=(CD(KN)-.5*(DCD(KN,1)+DCD(KN,NX)))*DX
      PRINT30,(CD(I),I=1,NN)

C     COMPUTE CDW
      CDW=0.
      DO 19 KN=1,NN
   19  CDW=CDW+CD(KN)
      CDW=(CDW-.5*(CD(1)+CD(NN)))*DETA
      PRINT31,CDW
      GO TO 100
    2 FORMAT(2I5,10X,4F10.4,/6F10.4,/6F10.4,/6F10.4,/6F10.4,/6F10.4,/
     16F10.4)
   29  FORMAT (//75H          X                ETA             PHI
     1 DPHI            DCD                              ,/)
   28  FORMAT (2F13.5,4E15.4)
   30  FORMAT (//9H CD(ETA) ,7E15.4,/8E15.4,/8E15.4)
   31  FORMAT (//6H CDW =,F15.4)
    1  FORMAT (7F10.4)
    4  FORMAT (//15H N,R,QNK VALUES,/)
   40  FORMAT (//70H1     M          RPS        RT         TEMP       CAX
     1  TAU0     MT                ,/7F10.4,/)
   20 FORMAT(I5,5X,F10.4,I5,5X,F10.6)
   22 FORMAT(/14H NN,DETA,NX,DX,I5,F10.4,I5,F10.6)
    8 FORMAT(2F5.1)
   11 FORMAT(5X,15HHUB-TIP RATIO =,F5.1,18HNUMBER OF BLADES =,F5.1,//)
```

```
51 FORMAT(E12.1)
52 FORMAT(18H REYNOLDS NUMBER =,E12.4)
53 FORMAT(25H SNK(10,J,5), RNK(10,J,1),6E15.5,/8E15.5,/8E15.5,/
  18E15.5,/8E15.5,/2E15.5)
55 FORMAT(4H X=,F13.5)
54 FORMAT(23H SNK(I,1,5), RNK(I,1,1),6E15.5,/8E15.5,/8E15.5,/8E15.5,/
  18E15.5,/2E15.5)
58 FORMAT(3H I=,I5,/)
56 FORMAT(17H QNK*RNK   AT  HUB,6E15.5,/8E15.5,/6E15.5)
60 FORMAT(17H QNK*RNK   AT  TIP,6E15.5,/8E15.5,/6E15.5)
   END
```

Part III - Induced Drag

```
C       SUBROUTINE TO COMPUTE BESSEL FUNCTIONS OF THE SECOND
C       KIND OF ORDER NB.
C       LEND=1,BZ=KP(RHO1)*I(RHO2)
C       LEND=2,BZ=K(RHO1)*IP(RHO2)
C       LEND=3,BZ=KP(RHO1)/KP(RHO2)
C       LEND=4,BZ=IP(RHO1)/IP(RHO2)
        SUBROUTINE BEZZEL(N,B,AN,LEND,RHO1,RHO2,BZ)
        DIMENSION  BZ(4)
        TAU1=SQRT(1.+RHO1**2)
        TAU2=SQRT(1.+RHO2**2)
        X=AN*B
        TAU3=((TAU1**2-1.)/(TAU1*TAU2))**0.5
        TAU4=((TAU1**2-1.)*TAU2/((TAU2**2-1.)*TAU1))**0.5
        TAU5=(TAU1-1.)*(TAU2+1.)/((TAU2-1.)*(TAU1+1.))
        EXPO=-X*(TAU1-TAU2)
        IF(EXPO+100.)16,10,12
   16 GO TO (7,7,7,8),LEND
    7 BZ(1)=0.
        GO TO 25
    8 BZ(1)=1.0E+60
        GO TO 25
   12 IF(EXPO-100.)10,10,28
   28 GO TO (29,29,29,30),LEND
   29 BZ(1)=1.0E+60
        GO TO 25
   30 BZ(1)=0.
        GO TO 25
   10 EXPA=EXP(EXPO)
   26 GO TO (18,19,20,21),LEND
   18 BZ(1)=-TAU3/(2.*X)*EXPA/TAU1*(1./TAU5)**(X/2.)
     1*(X/(TAU1**2-1.)+0.5/TAU1+X)
        GO TO 25
   19 TAU6=((TAU2**2-1.)/(TAU1*TAU2))**0.5
        BZ(1)=TAU6/(2.*X)*EXPA/TAU2*(1./TAU5)**(X/2.)*
     1(X/(TAU2**2-1.)-0.5/TAU2+X)
        GO TO 25
   20 BZ(1)=TAU4*TAU2/TAU1*EXPA*TAU5**(-X/2.)*(X/(TAU1**2-1.)
     1+0.5/TAU1+X)/(X/(TAU2**2-1.)+0.5/TAU2+X)
        GO TO 25
   21 BZ(1)=TAU4*TAU2/(TAU1*EXPA)*TAU5**(X/2.)*(X/(TAU1**2-1.)
     1-0.5/TAU1+X)/(X/(TAU2**2-1.)-0.5/TAU2+X)
   25 RETURN
        END
```

```
C       SUBROUTINE TO EVALUATE INTEGRANDS FOR INDUCED DRAG PROGRAM.
        SUBROUTINE DIFFEQ(M,X,Y,DY)
        COMMON N,AN,B,LEND,OMU,A,RHOH,RHOT,GAMO,RHOI,L
        DIMENSION ABZ1(4),ABZ2(4),BBZ1(4),GBZ(4),DY(2)
        ARG1=6.2832*(X-RHOH)/(RHOT-RHOH)
        ARG2=6.2832*X/(RHOT-RHOH)
        GAMP=GAMO*(ARG2*COS(ARG1)+SIN(ARG1))
        GO TO (1,2,3),L
    1   LEND=4
        CALL BEZZEL(N,B,AN,LEND,X,RHOT,ABZ1)
        IF(ABSF(ABZ1(1))-1.0E-15)22,21,23
   22   ABZ1(1)=0.
   23   CONTINUE
        LEND=3
        CALL BEZZEL(N,B,AN,LEND,X,RHOH,ABZ2)
        IF(ABSF(ABZ2(1))-1.0E-15)24,24,25
   24   ABZ2(1)=0.
   25   CONTINUE
        DY(1)=ABZ1(1)*X*GAMP
        DY(2)=ABZ2(1)*X*GAMP
        RETURN
    2   LEND=2
        CALL BEZZEL(N,B,AN,LEND,RHOI,X,BBZ1)
        DY(1)=BBZ1(1)*X*GAMP
        RETURN
    3   LEND=1
        CALL BEZZEL(N,B,AN,LEND,X,RHOI,GBZ)
        DY(1)=GBZ(1)*X*GAMP
        RETURN
        END
```

```
C       MAIN INDUCED DRAG PROGRAM.
C       INDUCED  DRAG COEFFICENTS
        COMMON N,AN,B,LEND,OMU,A,RHOH,RHOT,GAMO,RHOI,L
        DIMENSION  RHO(41),CD(41)
        DIMENSION S1(4),CBZ2(4),CBZ3(4),MARK(4),YMIN(2),TOL(2),XOUT(2),
       1Y1(2),Y2(1),Y3(1),DXI(41,20),XI(41)
        READ 1,RT,B,HUB,CAX,A
        READ 19,ANU
        READ 2,NRHO
        READ 4, NTERM
        ANRHO=NRHO
   80   READ 70,AM,RPS,U
        OMEGA=6.2832*RPS
        RE=U*RT/ANU
        CS=U/AM
```

```
      UB=OMEGA*RT
      AMT=(SQRT(UB**2+U**2))/CS
      PRINT 18,AMT,RE
      BETA=SQRT(1.-AM**2)
      RHOS=BETA/AM
      RHOT=OMEGA*RT/U
      OMU=OMEGA/U
      RHOH=HUB*RHOT
      GAMO=A*6.2832*U/(B*OMU)
      DRHO=(RHOT-RHOH)/(ANRHO-1.)
      DO 13 N=1,NTERM
      AN=N
      XOUT(1)=RHOT
      MARK(1)=1
      MARK(2)=1
      MARK(3)=0
      MARK(4)=0
      DO 22 IX=1,2
      YMIN(IX)=1.0E-06
      TOL(IX)=.001
   22 Y1(IX)=0.
      X1=RHOH
      H=.01
      L=1
      CALL RUNGE(2,X1,Y1,TOL,YMIN,H,XOUT,MARK)
      S1(1)=Y1(1)
      S1(2)=Y1(2)
      DO 13 I=1,NRHO
      AI=I-1
      RHO(I)=RHOH+AI*DRHO
      RHOI=RHO(I)
      XOUT(1)=RHOI
      X2=RHOH
      Y2(1)=0.
      H=.01
      L=2
      CALL RUNGE(1,X2,Y2,TOL,YMIN,H,XOUT,MARK)
      S2=Y2(1)
      XOUT(1)=RHOT
      X3=RHOI
       Y3(1)=0.
      H=.01
      L=3
      CALL RUNGE(1,X3,Y3,TOL,YMIN,H,XOUT,MARK)
      S3=Y3(1)
      LEND=1
      CALL BFZZEL(N,B,AN,LEND,RHOT,RHO(I),CBZ2)
      IF(ABSF(CBZ2(1))-1.0E-15)32,32,33
   32 CBZ2(1)=0.
   33 CONTINUE
      LEND=2
      CALL BFZZEL(N,B,AN,LEND,RHO(I),RHOH,CBZ3)
      IF(ABSF(CBZ3(1))-1.0E-15)34,34,35
   34 CBZ3(1)=0.
```

```
35 CONTINUE
   XIB=CBZ2(1)*S1(1)
   XIC=CBZ3(1)*S1(2)
   XIN=XIB+XIC-S2-S3
13 DXI(I,N)=XIN
   DO 3 I=1,NRHO
   XI(I)=0.
   DO 30 N=1,NTERM
30 XI(I)=XI(I)+DXI(I,N)
   F1=(RHO(I)+1./RHO(I))*XI(I)
   F3=2.*RHO(I)*A/(U*CAX*SQRT(1.+RHO(I)**2))
   F3=-F3
   ARG=6.2832*(RHO(I)-RHOH)/(RHOT-RHOH)
 3 CD(I)=F3*SIN(ARG)*F1
   PRINT 16
   DO 42 I=1,21,5
   PRINT 43,I
42 PRINT 41,(DXI(I,N),N=1,NTERM)
43 FORMAT(3H I=,I5)
41 FORMAT(9H DXI(I,N),8E12.4,/8E12.4)
   DO 44 I=1,NRHO
44 PRINT 40,RHO(I),CD(I)
40 FORMAT(F10.3,E10.3)
   CDWI=0.0
   DO 50 I=1,NRHO
   CD(I)=CD(I)/RHOT
50 CDWI=CDWI+CD(I)
   CDWI=(CDWI-0.5*(CD(1)+CD(NRHO)))*DRHO
   PRINT 60,CDWI
   GO TO 80
60 FORMAT(5X,4HCDW=,E10.3)
18 FORMAT(4H1MT=,F5.2,5X,17HREYNOLDS NUMBER =,E12.3)
16 FORMAT(5X,3HRHO,8X,2HCD/)
 1 FORMAT(5F8.3)
19 FORMAT(E10.3)
 2 FORMAT(I5)
 4 FORMAT(I5)
70 FORMAT(3F8.3)
   END
```

TABLE I

Q^*_{nBk} for B = 40, h = 0.80

$$\tau(\rho) = \tau_o \frac{\rho_H}{\rho} \sqrt{\frac{\rho_H^2 + 1}{\rho^2 + 1}}$$

m \ k	1	2	3	4	5	6	7	8	9	10
1	.4075	.3211	.0639	.0187	.0036					
2	.3170	.3116	.2521	.1099	.0246	.0103	-.0031			
3	.2732	.2646	.2418	.2281	.1320	.0432	-.0128	.0066	-.0025	-.0022
4	.2484	.2357	.2129	.2115	.2035	.1485	.0593	.0210	-.0078	.0045
5	.2295	.2167	.1944	.1907	.1854	.1849	.1560	.0808	.0286	-.0123
6	.2150	.2027	.1818	.1768	.1705	.1701	.1687	.1574	.0964	.0408
7	.2046	.1922	.1711	.1668	.1604	.1583	.1561	.1563	.1521	.1131
8	.1954	.1839	.1624	.1578	.1526	.1500	.1472	.1476	.1462	.1451
9	.1875	.1751	.1554	.1512	.1451	.1430	.1403	.1384	.1370	.1378
10	.1804	.1686	.1495	.1457	.1398	.1368	.1341	.1325	.1312	.1298

Continued on next page

TABLE I (continued)

Q^*_{nBk} for B = 40, h = 0.80

$$\tau(\rho) = \tau_o \frac{\rho_H}{\rho} \sqrt{\frac{\rho_H^2 + 1}{\rho^2 + 1}}$$

m \ k	11	12	13	14	15	16	17	18	19	20
1										
2										
3										
4	-.0020									
5	-.0052	-.0033								
6	.0157	-.0077	.0037	-.0026						
7	.0538	.0222	-.0096	-.0053	.0027	-.0020				
8	.1226	.0695	.0292	.0132	-.0064	.0038	-.0021			
9	.1376	.1269	.0822	.0391	.0170	-.0086	-.0045	.0029	-.0017	.0013
10	.1298	.1304	.1265	.0956	.0502	.0227	.0107	-.0059	.0033	.0023

TABLE II

Behavior of $\chi_n(\rho)$

$B = 40$, $h = 0.80$, $w/U = 5.163$, $\rho_T = 1.756$, $M_T = .51$

n \ ρ/ρ_T	.8	.85	.90	.95	1.00
1	.2002	-.07508	-.007549	.08741	-.2480
2	.1084	-.02134	-.002378	.02535	-.1390
3	.07314	-.009671	-.001110	.01151	-.09506
4	.05505	-.005476	-.000648	.006522	-.07199
5	.04410	-.003515	-.000422	.004187	-.05788
6	.03676	-.002445	-.000297	.002913	-.04837
7	.03153	-.001798	-.000221	.002143	-.04154
8	.02759	-.001377	-.000183	.001641	-.03639
9	.02453	-.001088	-.000149	.001297	-.03238
10	.02208	-.000882	-.000124	.001051	-.02916
11	.02007	-.000729	-.000106	.000869	-.02652
12	.01840	-.000612	-.000092	.000730	-.02433
13	.01698	-.000522	-.000081	.000622	-.02246
14	.01578	-.000450	-.000074	.000536	-.02086
15	.01473	-.000392	-.000071	.000467	-.01948

TABLE III

$\frac{10^3 \times Q^*_{nk} \times R_{nk} \times S_{nk}}{\lambda_{nk}}$ B = 40, h = 0.80 M_T = .98 $\frac{X}{C_{ax}}$ = .05

Top figures denote values at the root; bottom figures denote values at the tip.

Error Estimates: Root - .8%; Tip - 2%

n \ k	1	2	3	4	5	6	7	8	9	10
1	.0067 .0614	.1653 -.1208	.0460 .0328	.0119 -.0096	.0019 .0016					
2	0 .1083	.0105 -.0543	.0409 .0331	.0260 -.0153	.0052 .0036	.0019 -.0015	.0005 .00041			
3	0 .0527	0 -.0237	.0032 .0172	.0136 -.0135	.0142 .00763	.0045 -.00277	.0012 .00083	.00056 -.00042	.00020 .00015	.00016 -.00013
4	0 .0222	0 -.0124	0 .0093	.0012 -.0081	.0053 .0069	.0086 -.0047	.0038 .0021	.0012 -.00077	.00041 .00029	.00022 -.00016
5	0 .0140	0 -.0079	0 .0059	0 -.0051	.00050 .0045	.0023 -.0041	.0052 .0031	.0035 -.0017	.0011 .00066	.00045 -.00029
6	0 .0106	0 -.0055	0 .0040	0 -.0035	0 .0031	.00023 -.0028	.0011 .0026	.0030 -.0022	.0029 .00137	.0012 -.00063
7	0 .0077	0 -.0040	0 .0029	0 -.0025	0 .0022	0 -.0021	.00011 .0019	.00056 -.0018	.0017 .0016	.0024 -.0012
8	0 .00576	0 -.00308	0 .0022	0 -.0019	0 .0017	0 -.0016	0 .00144	.00013 -.00137	.00032 .00130	.00097 -.00121
9	0 .0046	0 -.0024	0 .00176	0 -.0015	0 .0013	0 -.0012	0 .00112	0 -.00106	0 .0010	.00017 -.00097
10	0 .0037	0 -.00195	0 .00142	0 -.00123	0 .00107	0 -.00098	0 .00091	0 -.00085	0 .00081	0 -.00077

TABLE III (continued)

$\frac{10^3 \times Q^*_{nk} \times R_{nk} \times S_{nk}}{\lambda_{nk}}$ B = 40, h = 0.80 M_T = .98 $\frac{X}{C_{ax}}$ = .05

Top figures denote values at the root; bottom figures denote values at the tip.

Error Estimates: Root - .8%; Tip - 2%

n \ k	11	12	13	14	15	16	17	18	19	20	10^3 x partial sums
1	—	—	—	—	—	—	—	—	—	—	.2318 -.0346
2	—	—	—	—	—	—	—	—	—	—	.085 .0743
3	—	—	—	—	—	—	—	—	—	—	.0376 .0380
4	.000092 .000071	—	—	—	—	—	—	—	—	—	.0208 .0147
5	.00018 .00012	.00011 -.000077	—	—	—	—	—	—	—	—	.0133 .0091
6	.00042 .00025	.00019 -.00013	.000087 .000060	.000058 -.000042	—	—	—	—	—	—	.0092 .0072
7	.0012 .00060	.00047 -.00026	.00019 .00011	.000096 -.000064	.000047 .000032	.000033 -.000024	—	—	—	—	.0068 .0051
8	.0018 .00096	.0013 -.00057	.00050 .00026	.00021 -.00012	.000094 .000059	.000053 -.000035	.000028 .000019	—	—	—	.0054 .0038
9	.00055 .00092	.00122 -.00079	.00116 .00052	.00055 -.00027	.00022 .00012	.00010 -.000062	.000051 .000033	.000032 -.000021	.000018 .000012	.000013 -.000009	.0041 .0031
10	.000091 .00074	.00032 -.00071	.00080 .00065	.0010 -.00048	.000598 .00027	.00025 -.00013	.00011 .000062	.000057 -.000034	.000030 .000019	.000020 -.000014	.0033 .0025

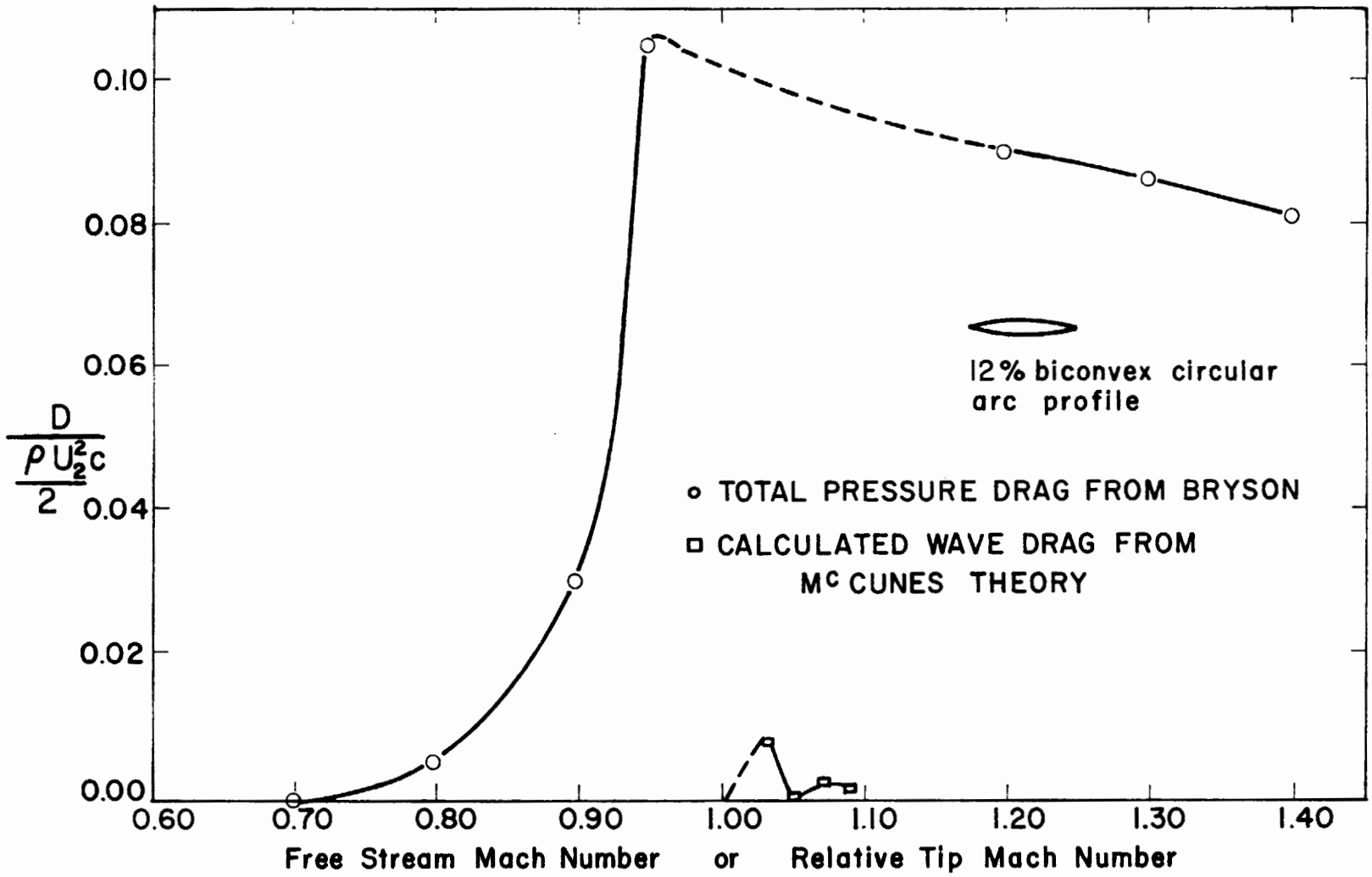

FIG. 1: McCUNE'S WAVE DRAG COEFFICIENT COMPARED WITH BRYSON'S 2-D PRESSURE DRAG MEASUREMENTS

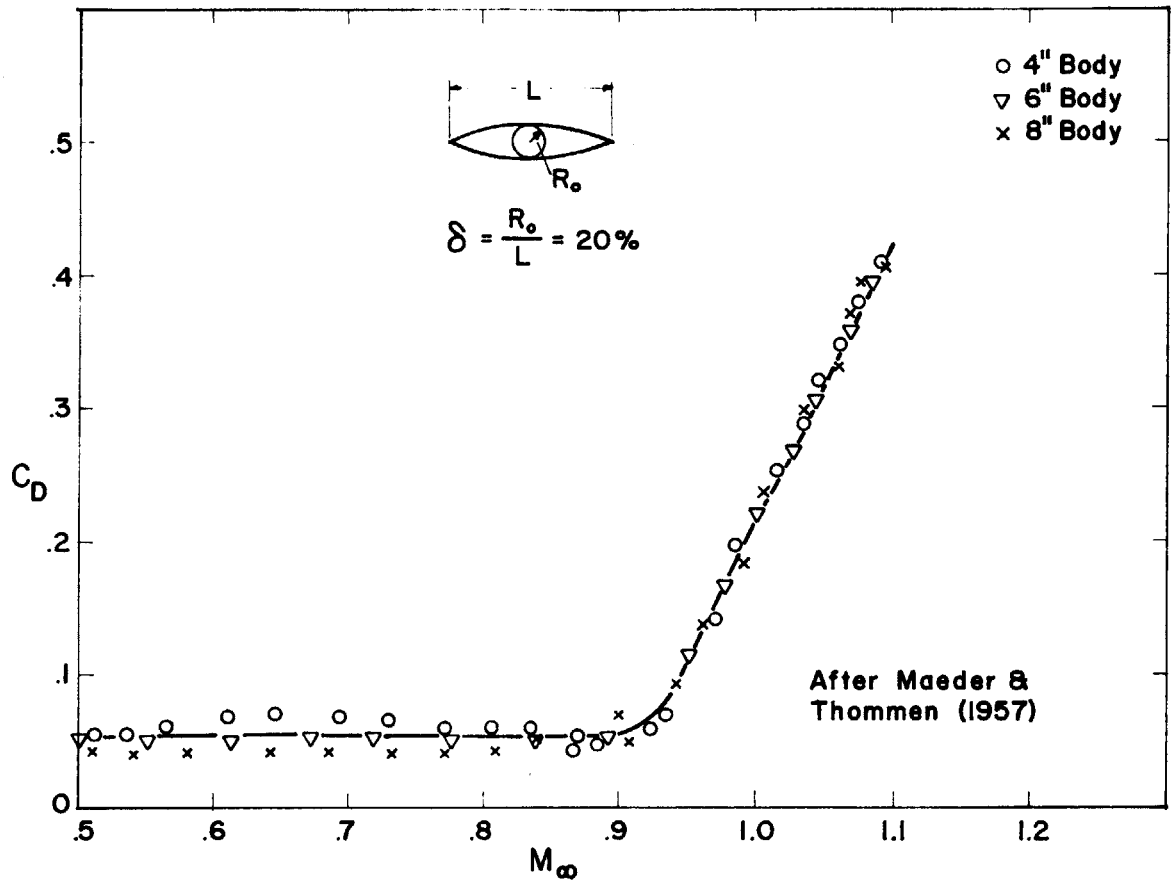

FIG. 2: VARIATION OF DRAG COEFFICIENT WITH FREE STREAM MACH NUMBER - PARABOLIC BODY OF REVOLUTION

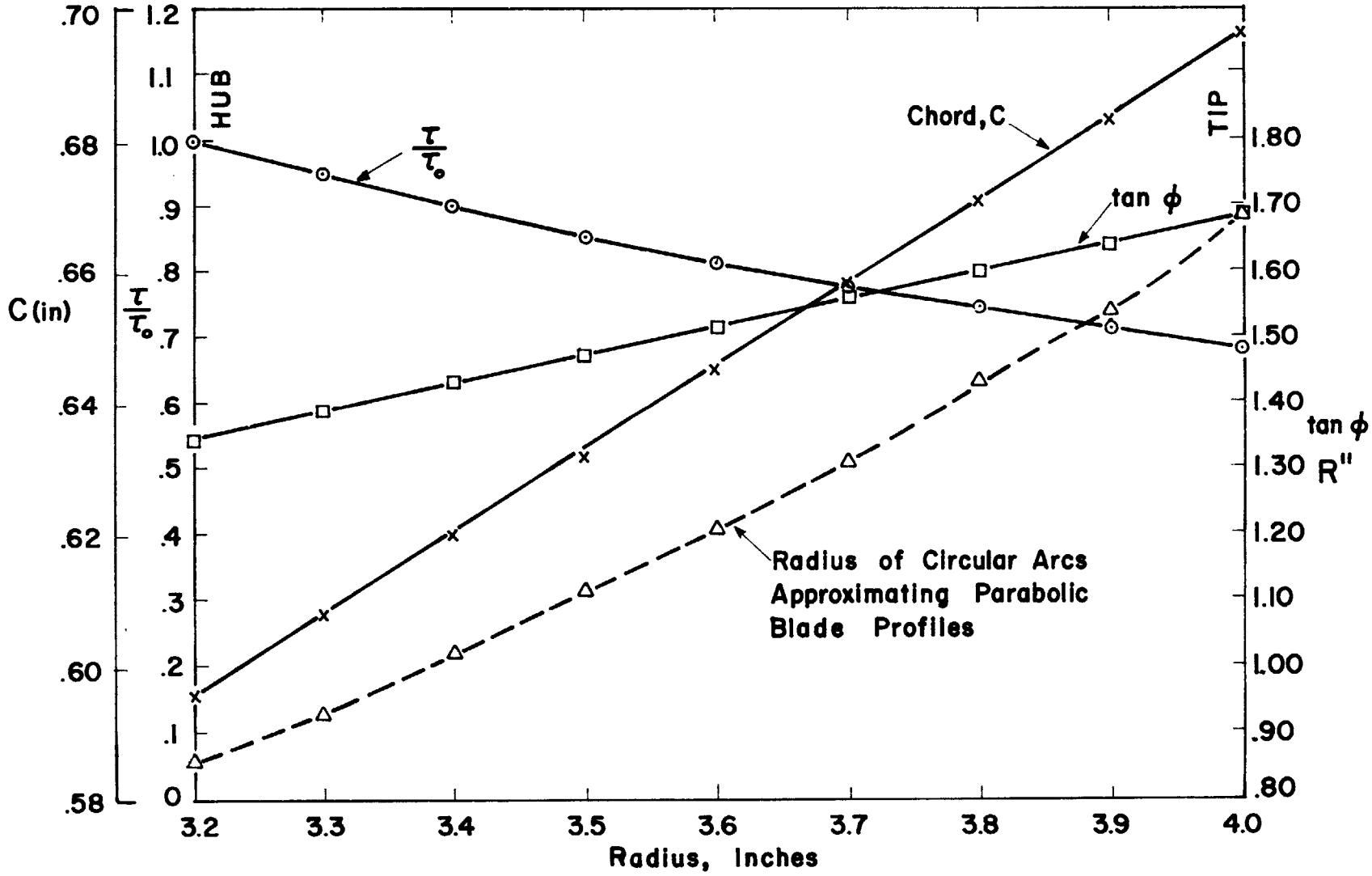

FIG. 3: BLADE PARAMETERS – RADIAL DISTRIBUTIONS

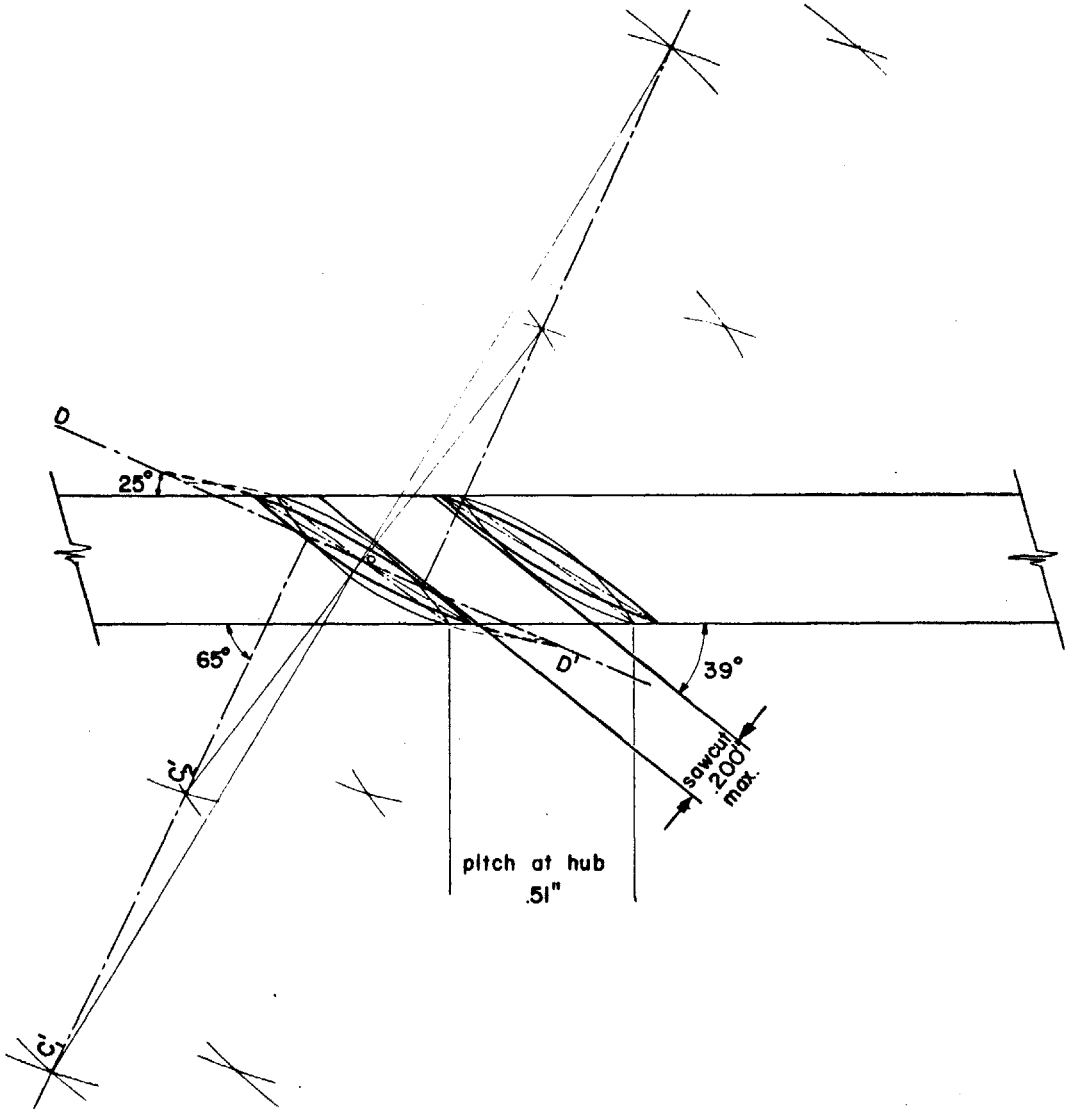

FIG. 4a: SCHEMATIC OF ROTOR CONSTRUCTION - SHOWING PROJECTION OF CONE AXIS IN THE PLANE CONTAINING RIM OF ROTOR

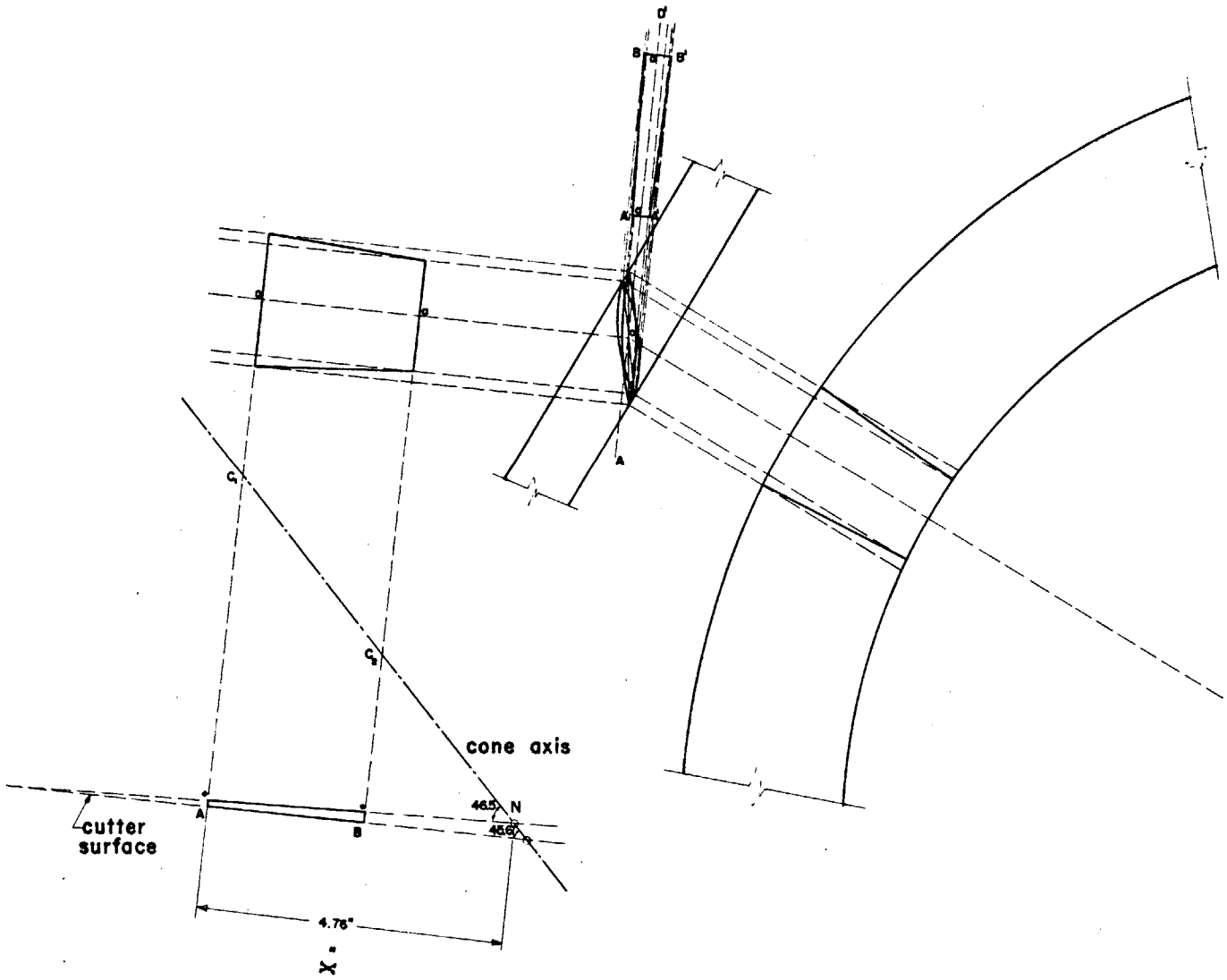

FIG. 4b: SCHEMATIC OF ROTOR CONSTRUCTION SET UP, SHOWING INCLINATION OF ROTOR AXIS TO BLADE MIDPLANE

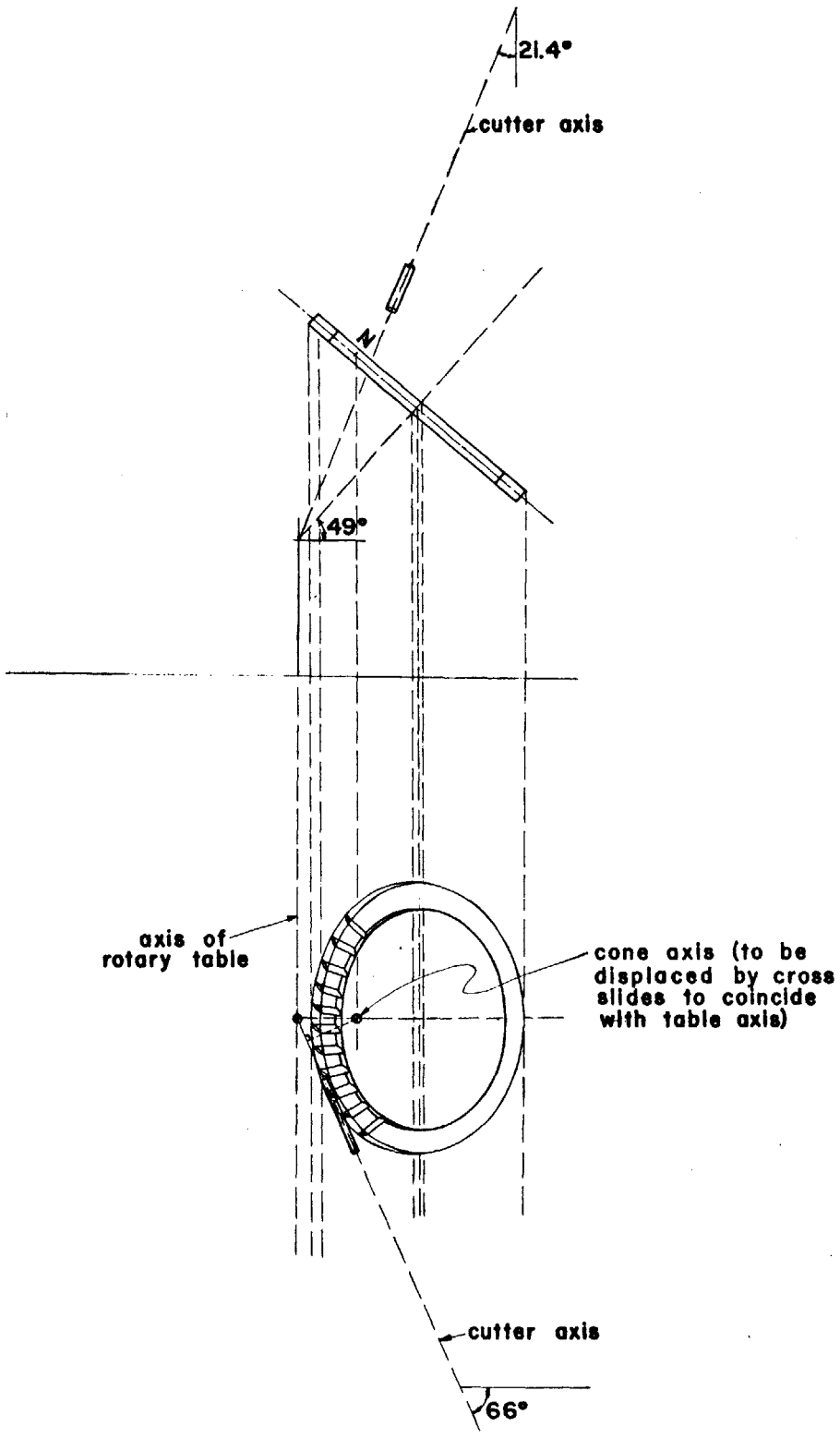

FIG. 4c: SCHEMATIC OF ROTOR CONSTRUCTION SET UP – SHOWING OFFSETS

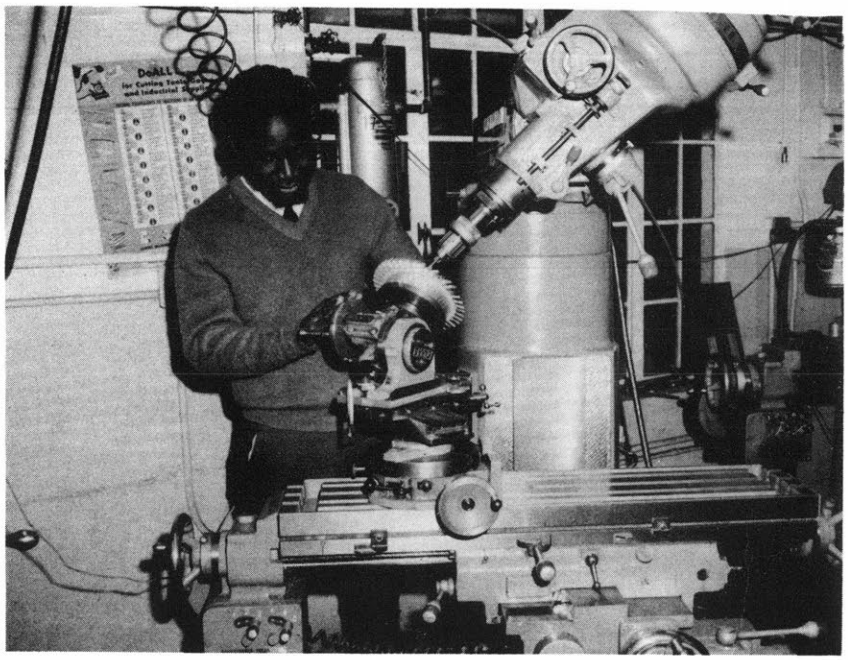

FIG. 5: SET-UP FOR ROTOR CONSTRUCTION

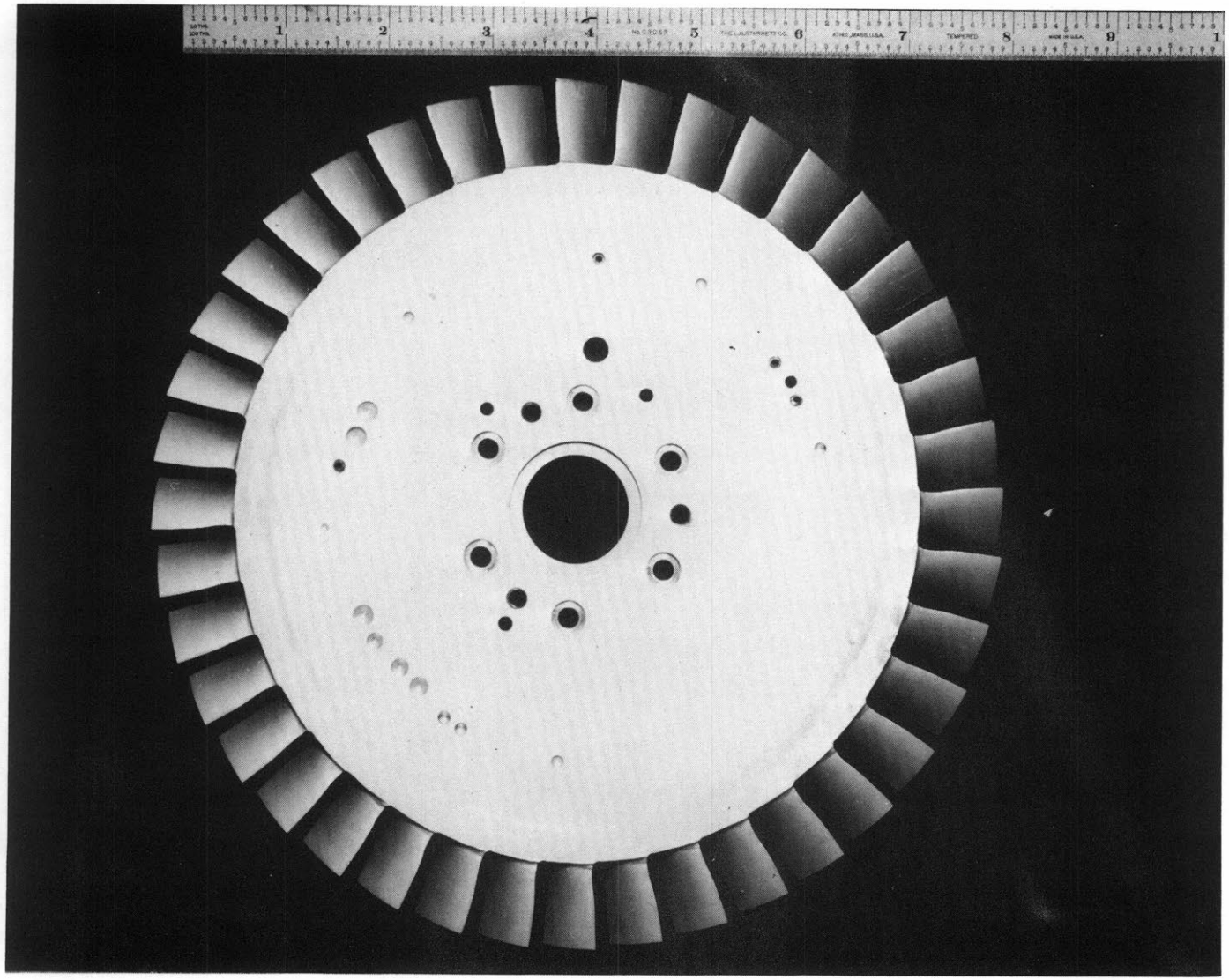

FIG. 6: FINISHED ROTOR

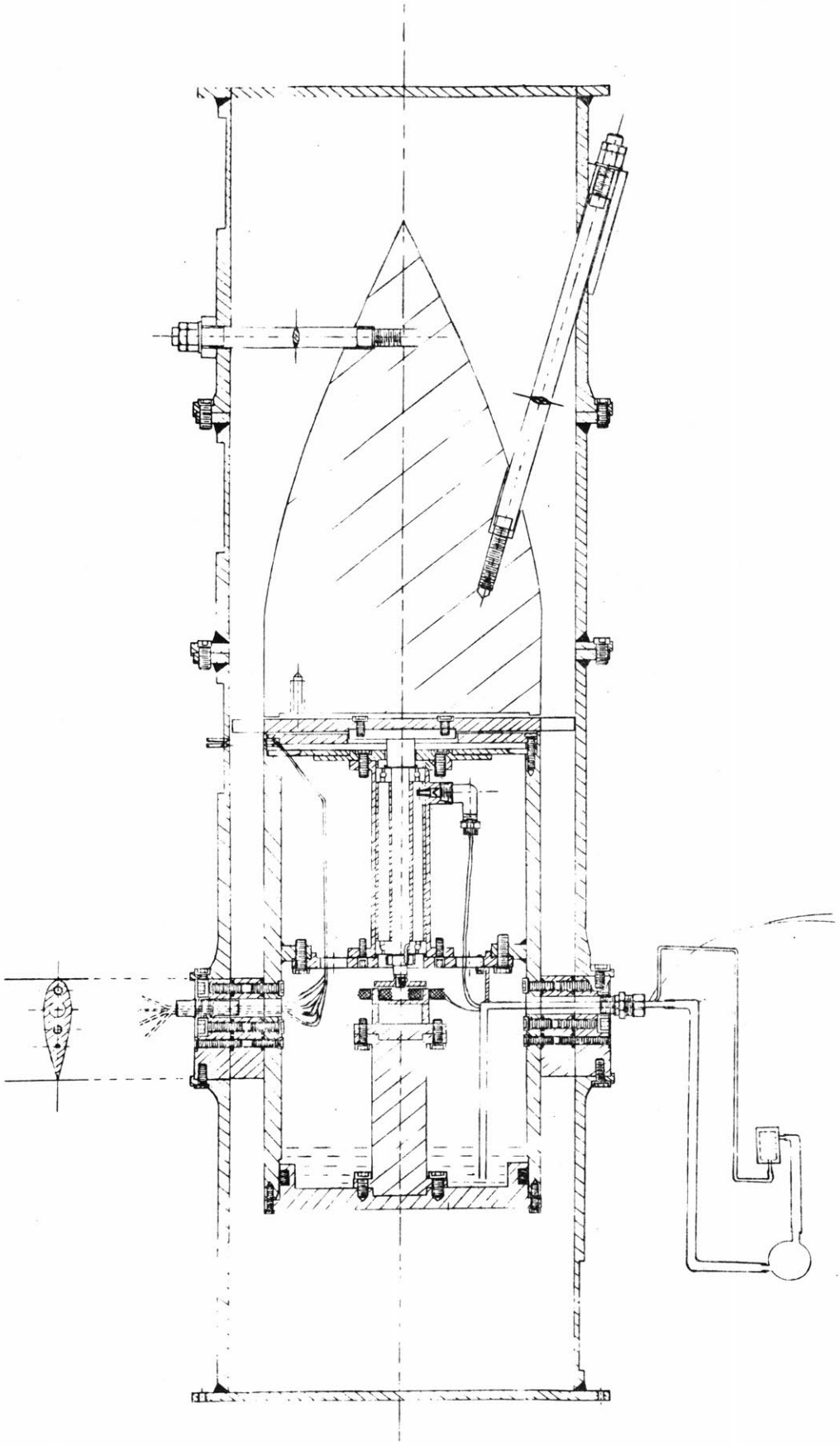

FIG. 7: SCHEMATIC OF TEST SECTION

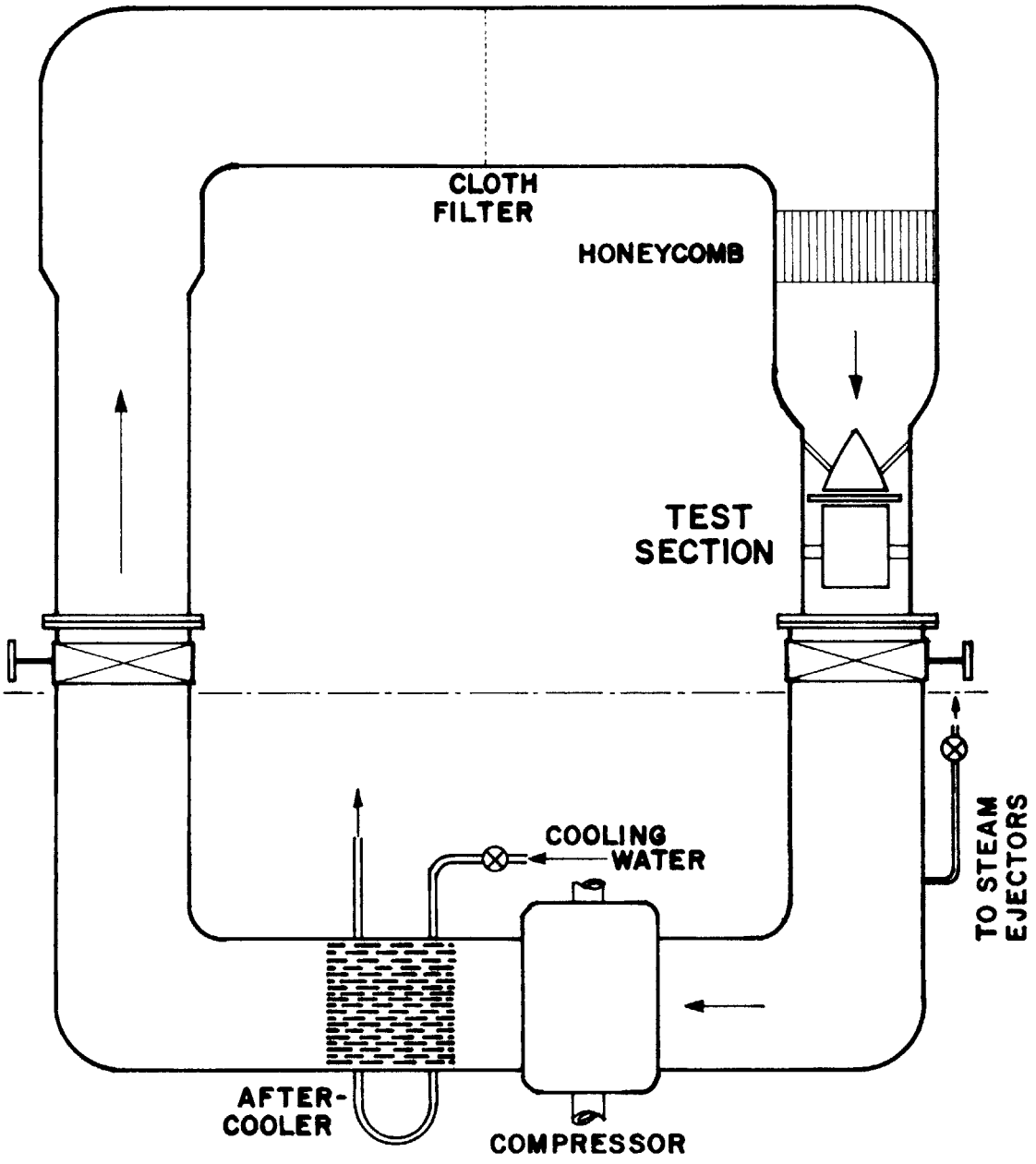

FIG. 8a: SCHEMATIC OF TEST SYSTEM

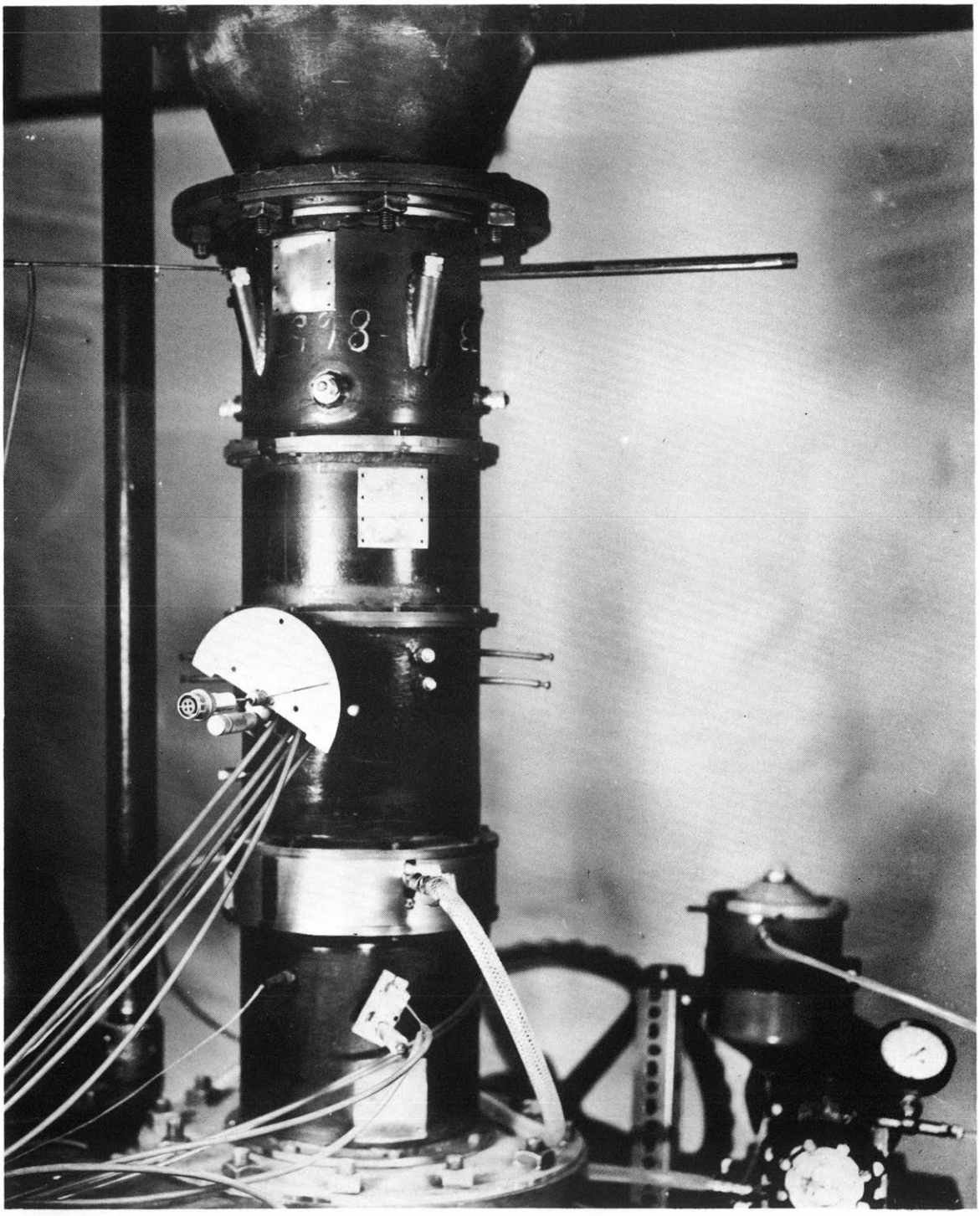

FIG. 8b: TEST SECTION ASSEMBLY

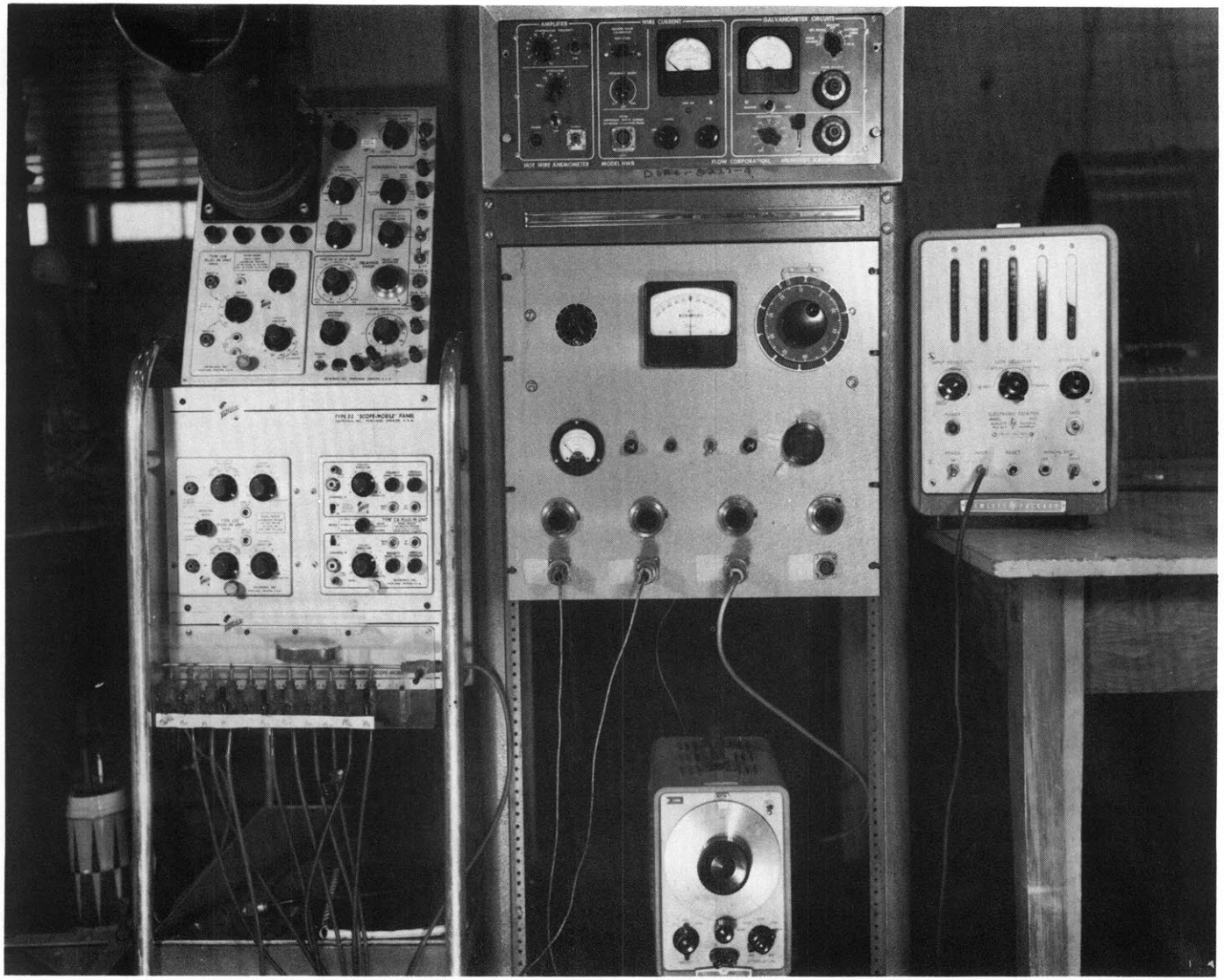

FIG. 8c: EQUIPMENT PANEL

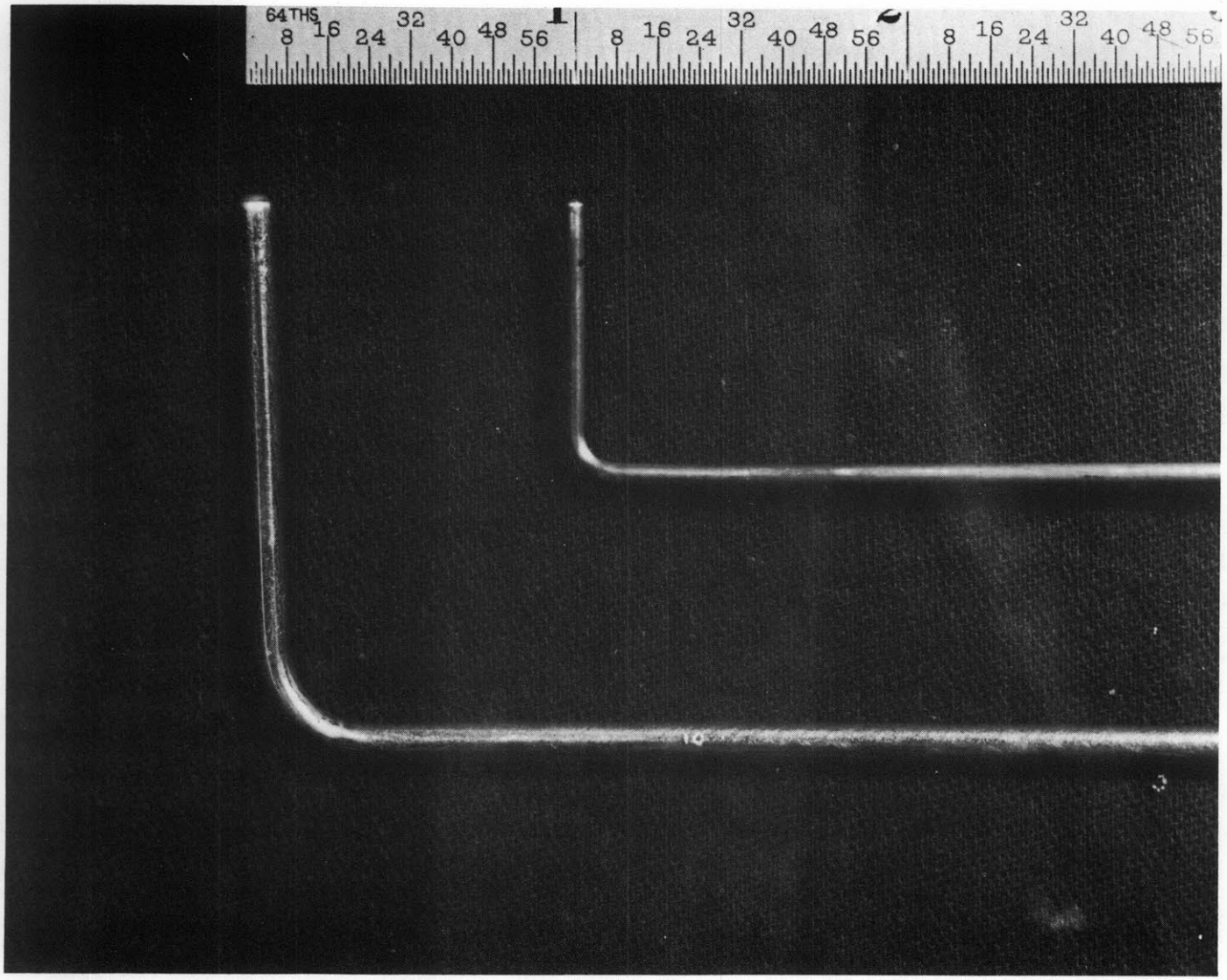

FIG. 9: PITOT - STATIC TUBES

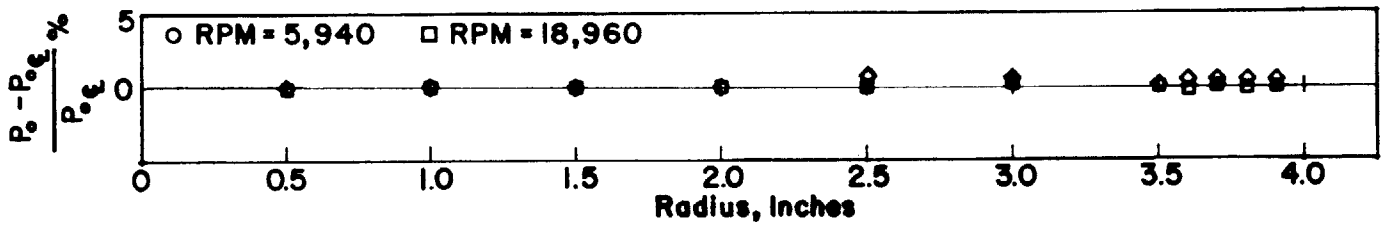

FIG. 10a: TOTAL PRESSURE DISTRIBUTION AT STATION 1

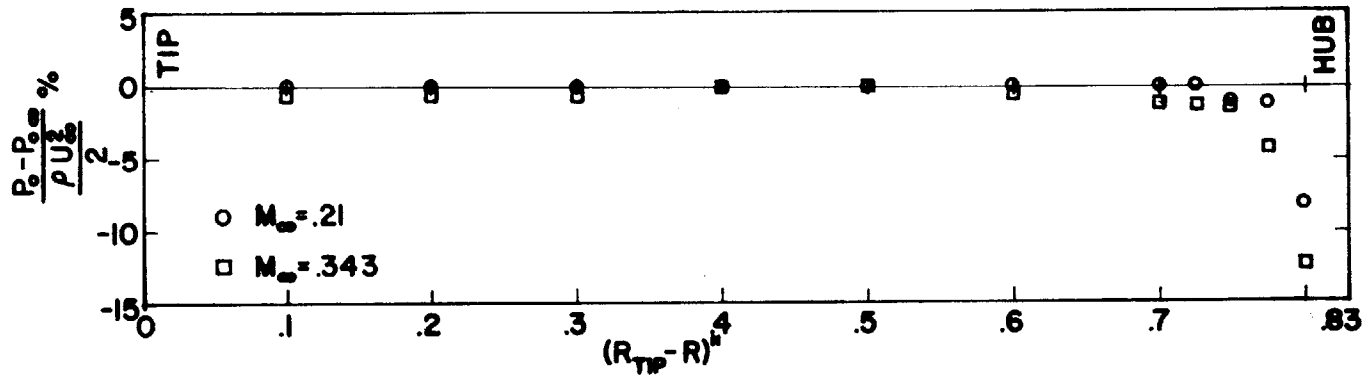

FIG. 10b: TOTAL PRESSURE DISTRIBUTION AT STATION 2

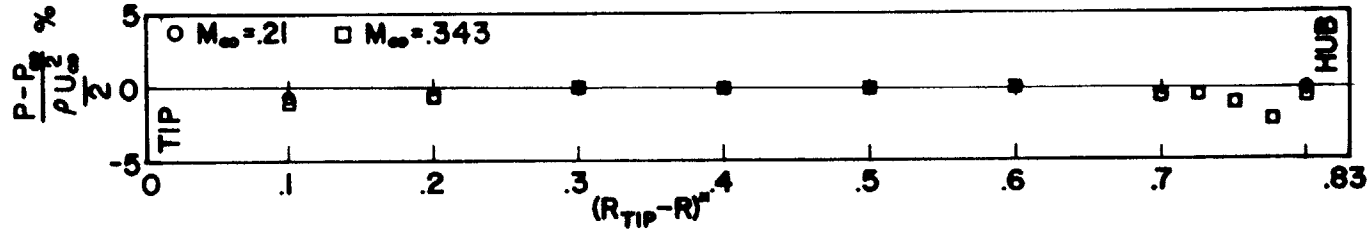

FIG: 10c. STATIC PRESSURE DISTRIBUTION AT STATION 2

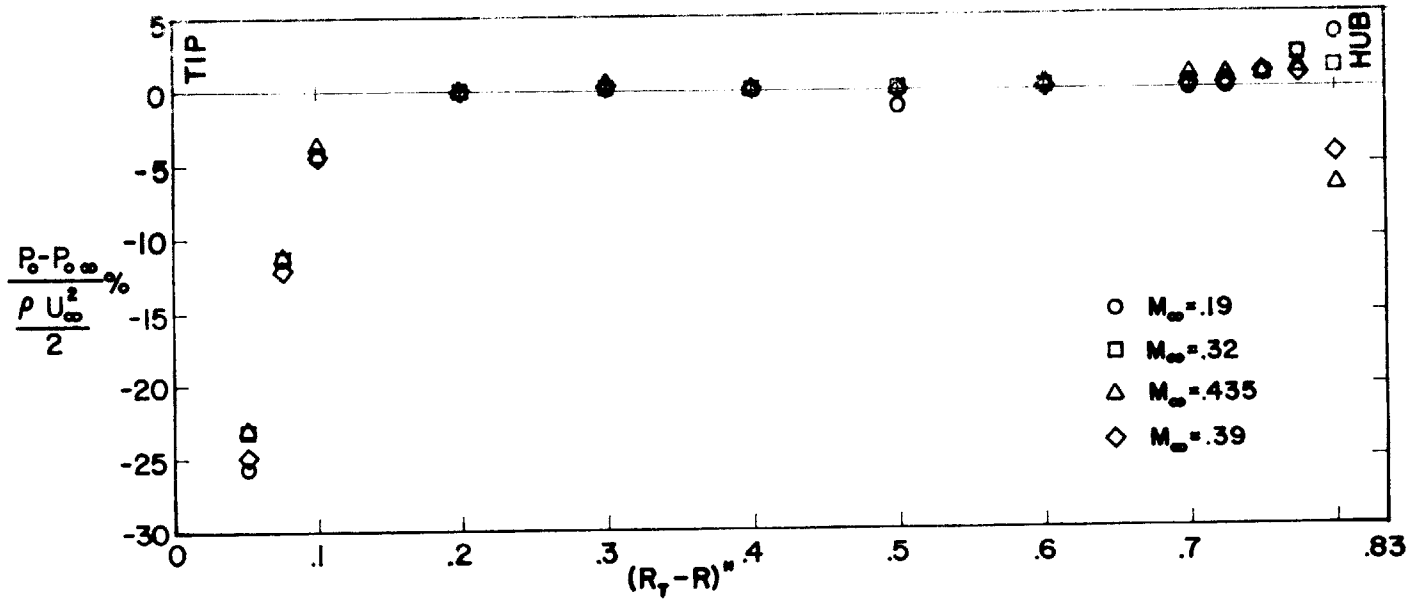

FIG. 10d: TOTAL PRESSURE DISTRIBUTION AT STATION 3 USING DIRECTION PROBE WITHOUT ROTOR

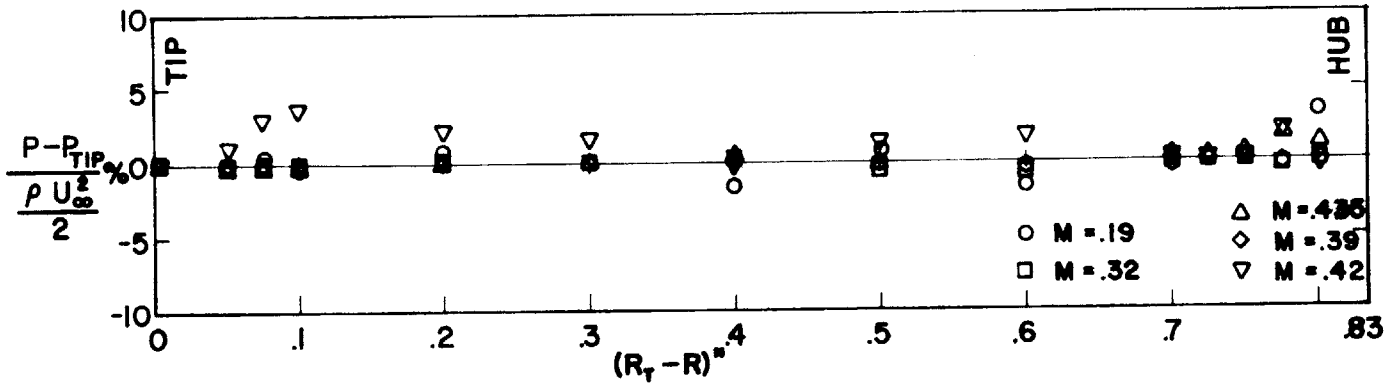

FIG. 10e: STATIC PRESSURE DISTRIBUTION AT STATION 3 USING DIRECTION PROBE WITHOUT ROTOR

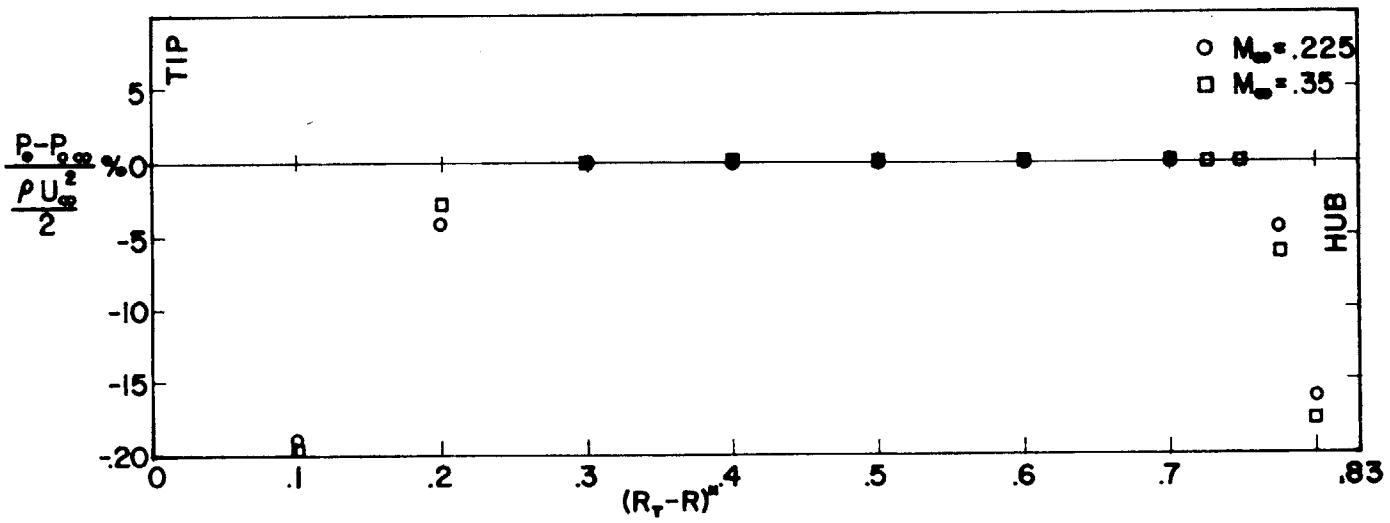

FIG. 10f: TOTAL PRESSURE DISTRIBUTION AT STATION 4, WITHOUT ROTOR

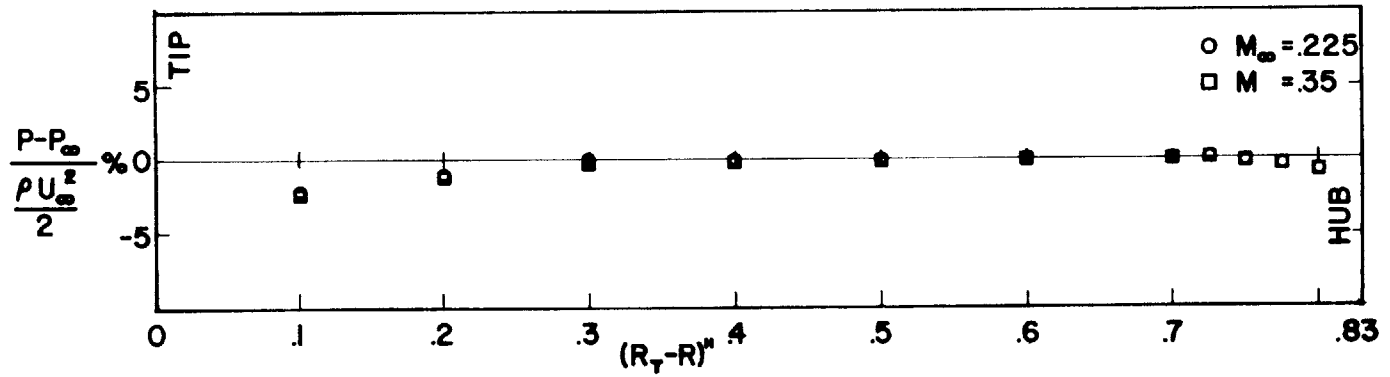

FIG. 10g: STATIC PRESSURE DISTRIBUTION AT STATION 4, WITHOUT ROTOR

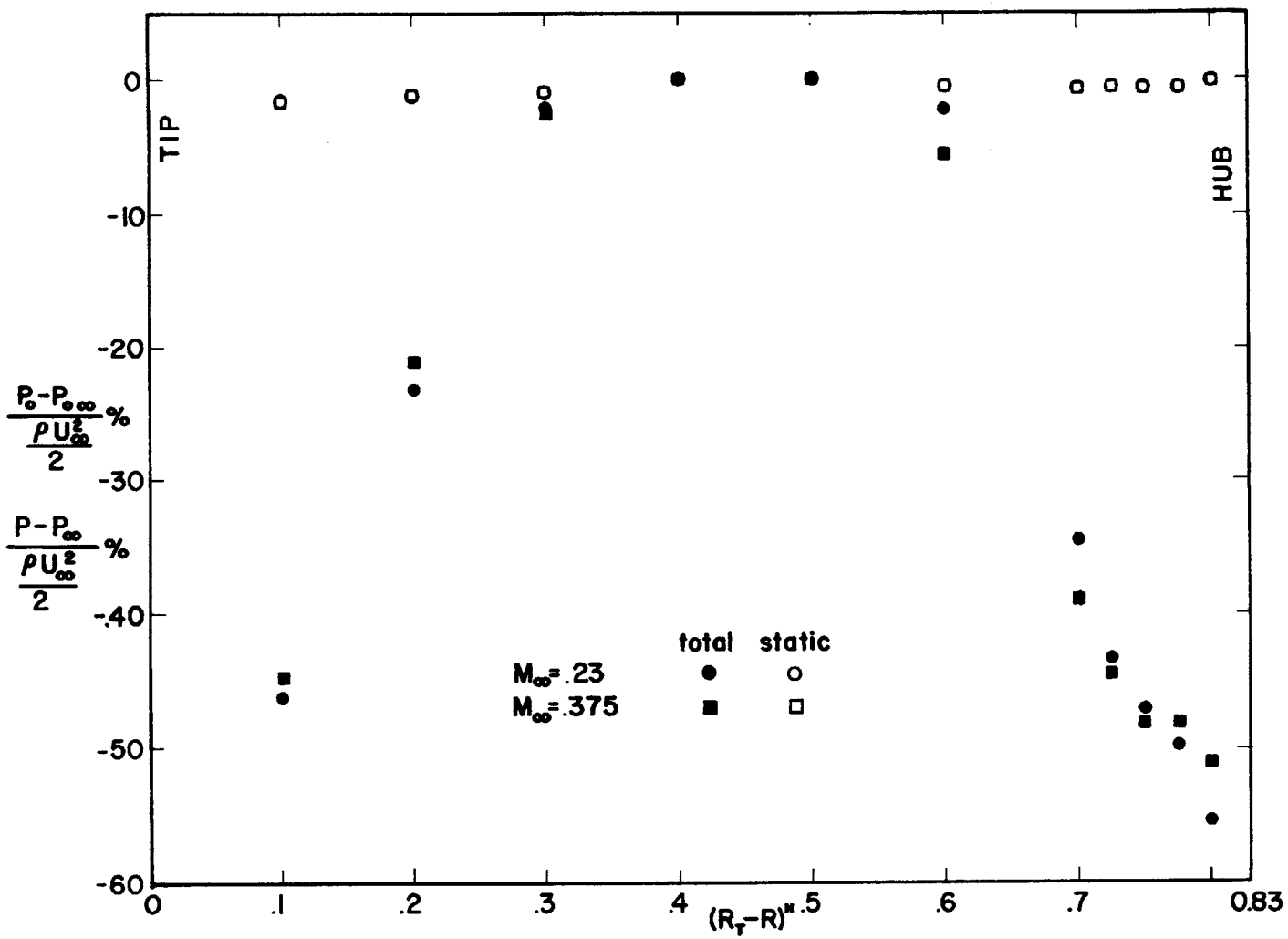

FIG. 10h: TOTAL PRESSURE DISTRIBUTION AT STATION 5, WITHOUT ROTOR
FIG. 10i: STATIC PRESSURE DISTRIBUTION AT STATION 5, WITHOUT ROTOR

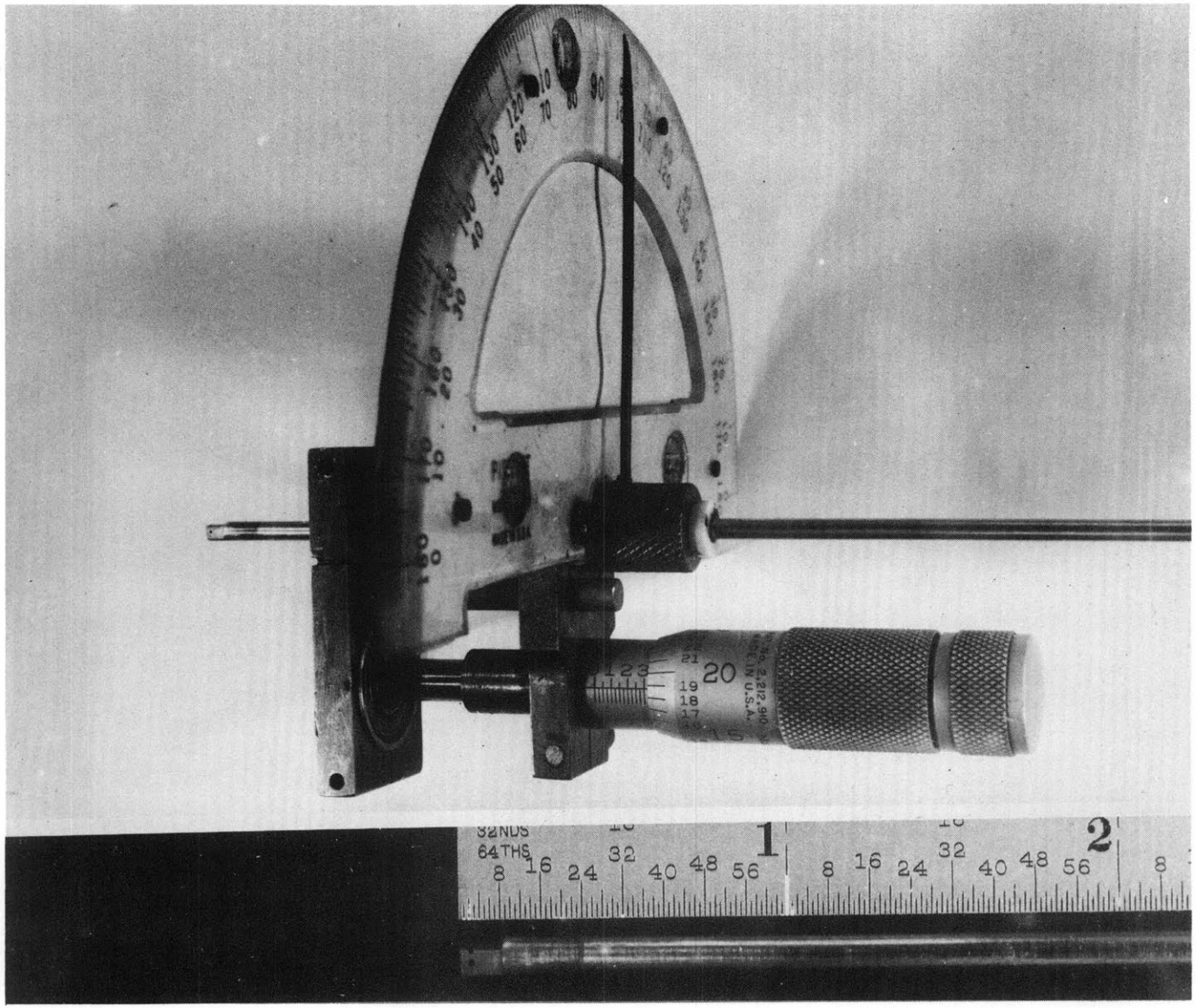

FIG. 11: 3-HOLE YAW PROBE WITH INDICATING MECHANISM

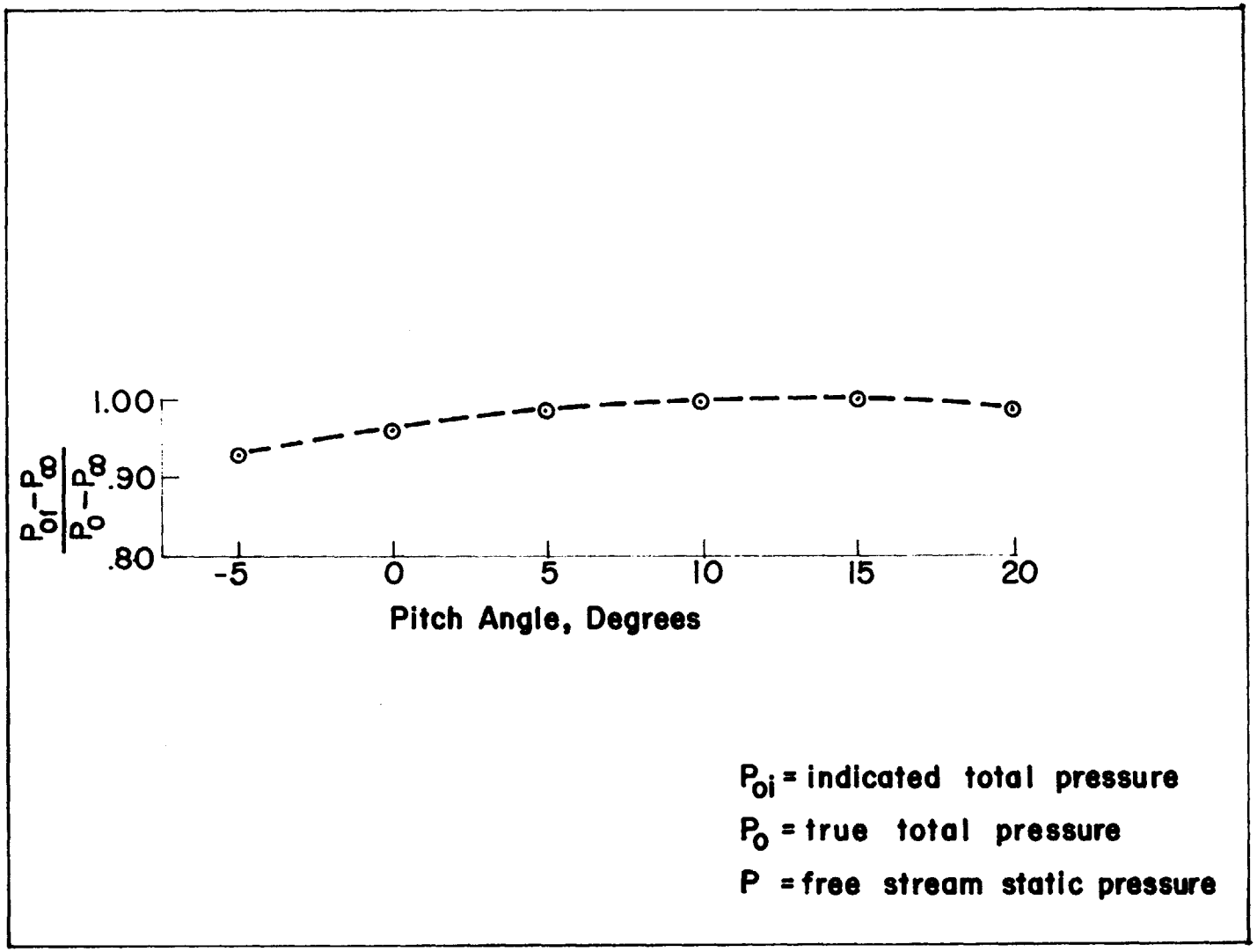

FIG. 12a: YAW PROBE ZERO PITCH CALIBRATION

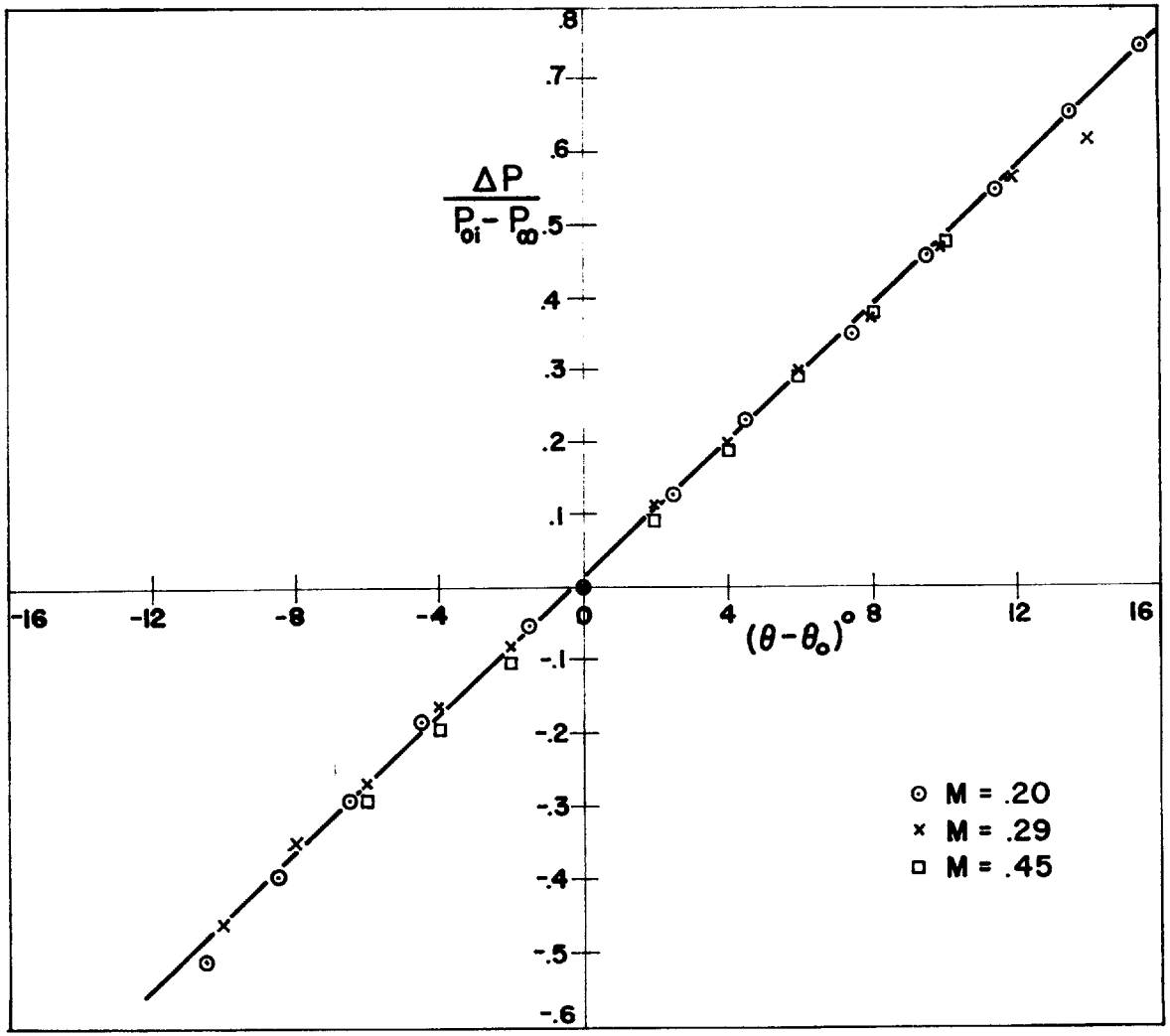

FIG. 12b: YAW PROBE DIRECTION SENSITIVITY

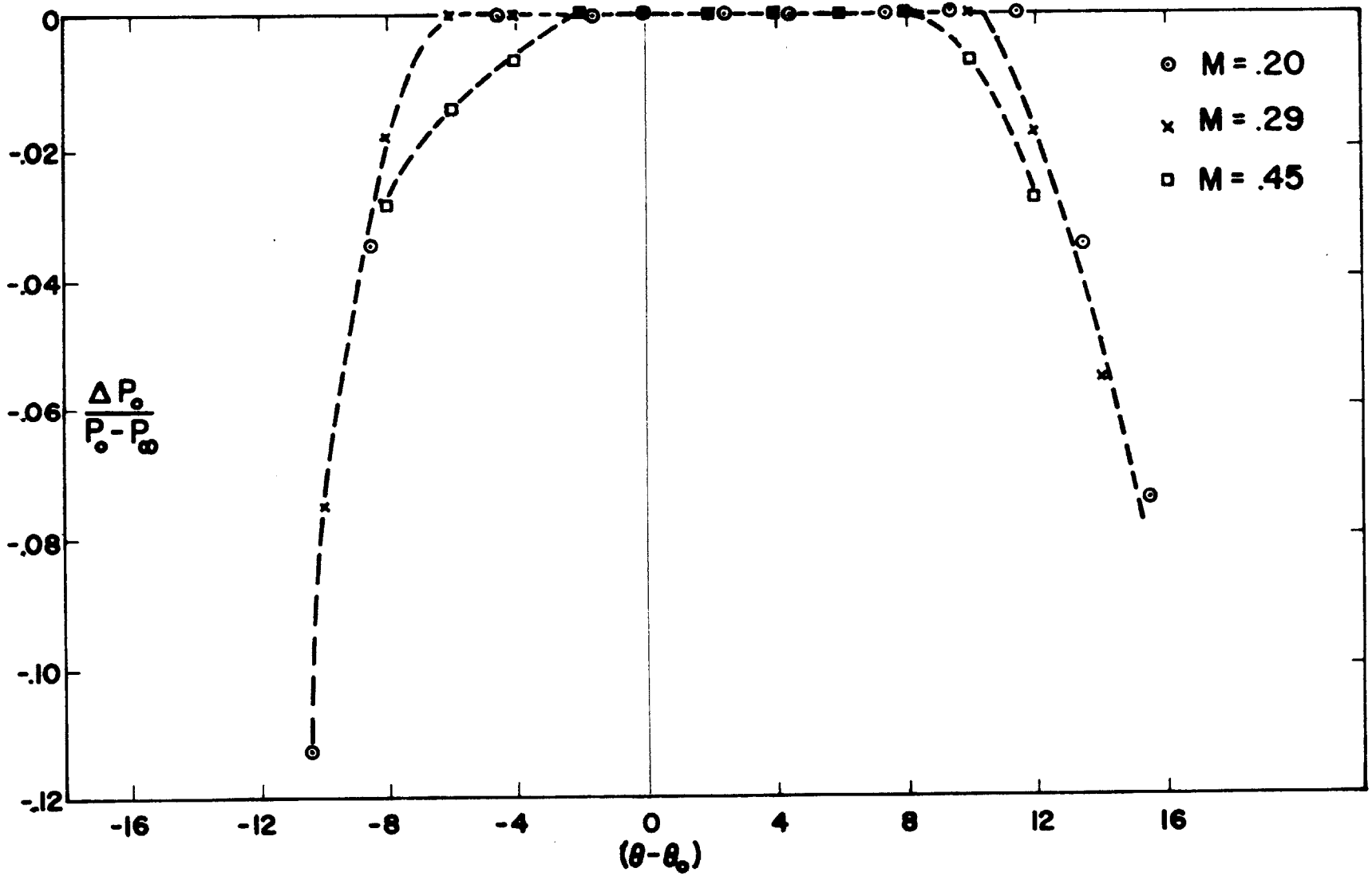

FIG. 12c: SENSITIVITY OF YAW PROBE-INDICATED TOTAL PRESSURE TO YAW ANGLE

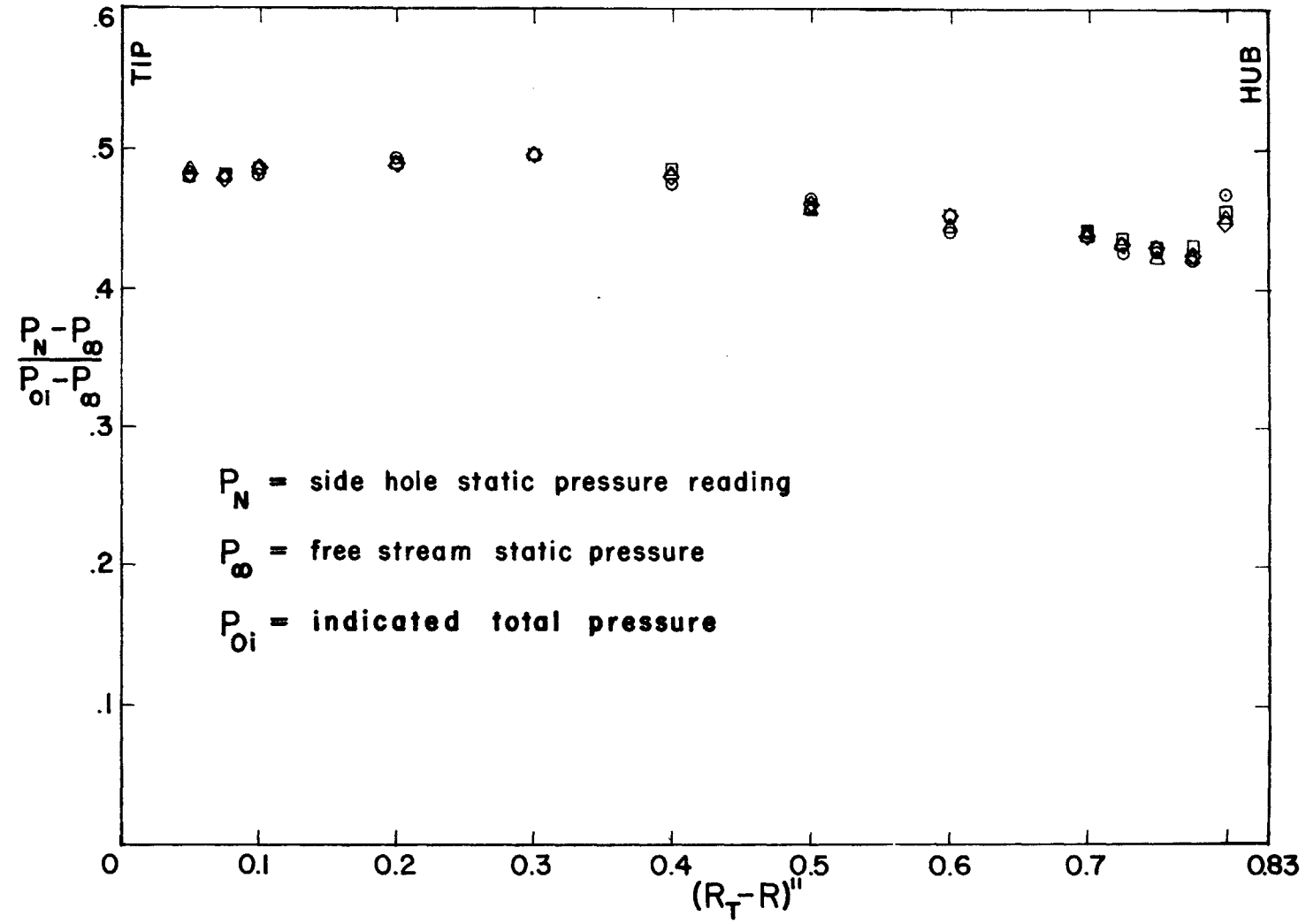

FIG. 12d: YAW PROBE CALIBRATION FOR STATIC PRESSURE MEASUREMENTS

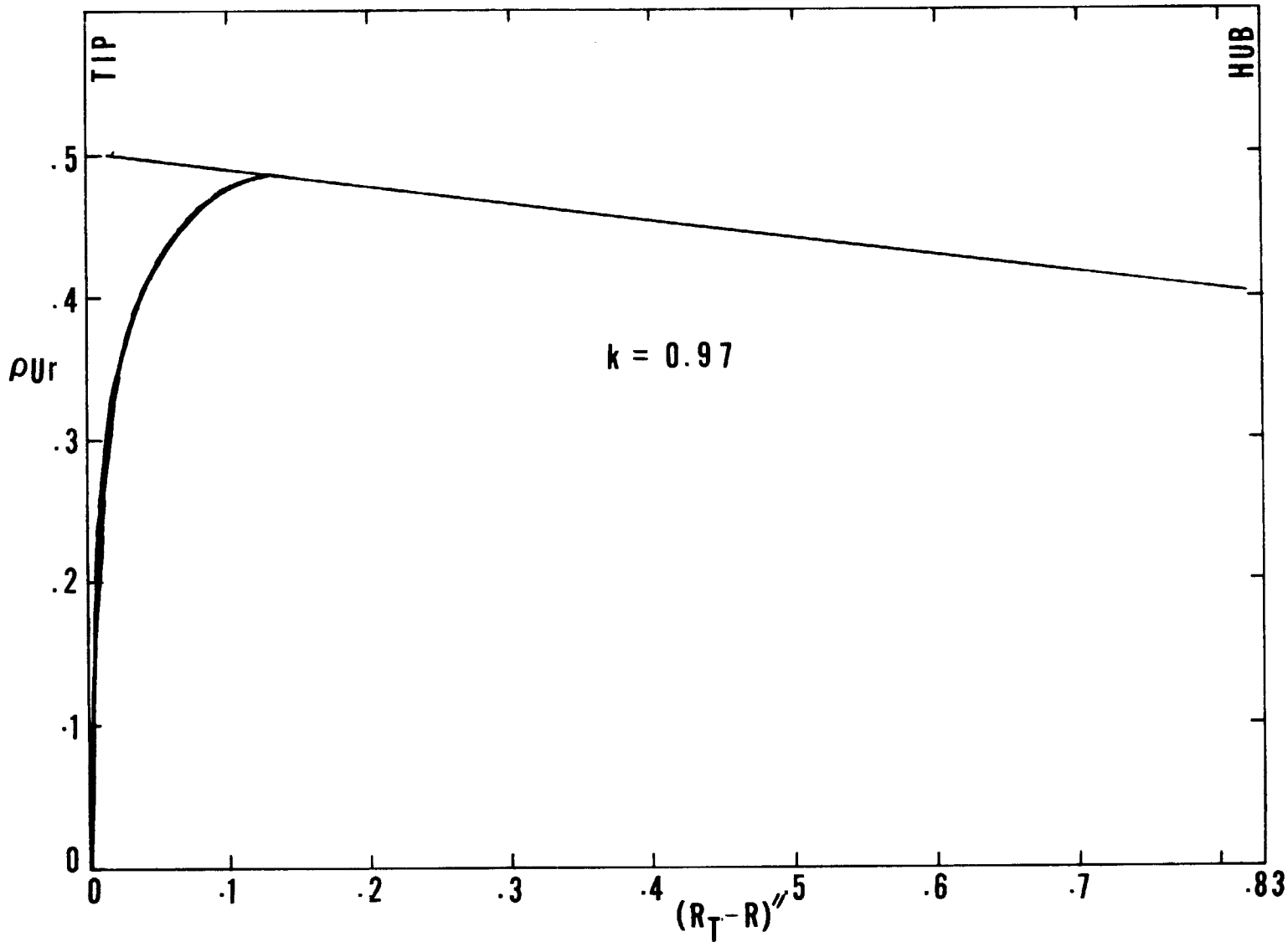

FIG. 13: EVALUATION OF "DISCHARGE COEFFICIENT"

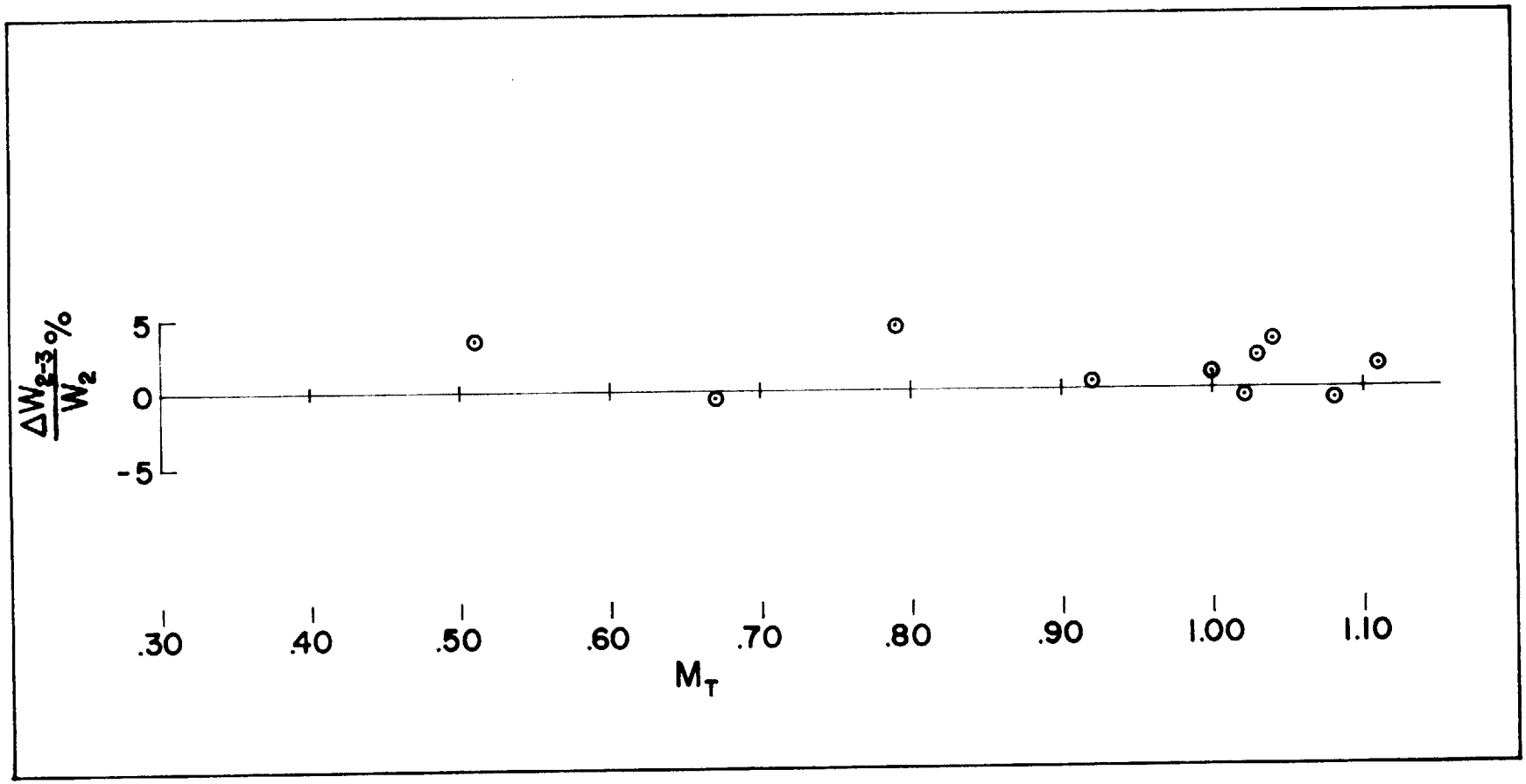

FIG. 14: COMPARISON OF INTEGRATED MASS FLOW AT STATION 3 WITH MASS FLOW AT STATION 2

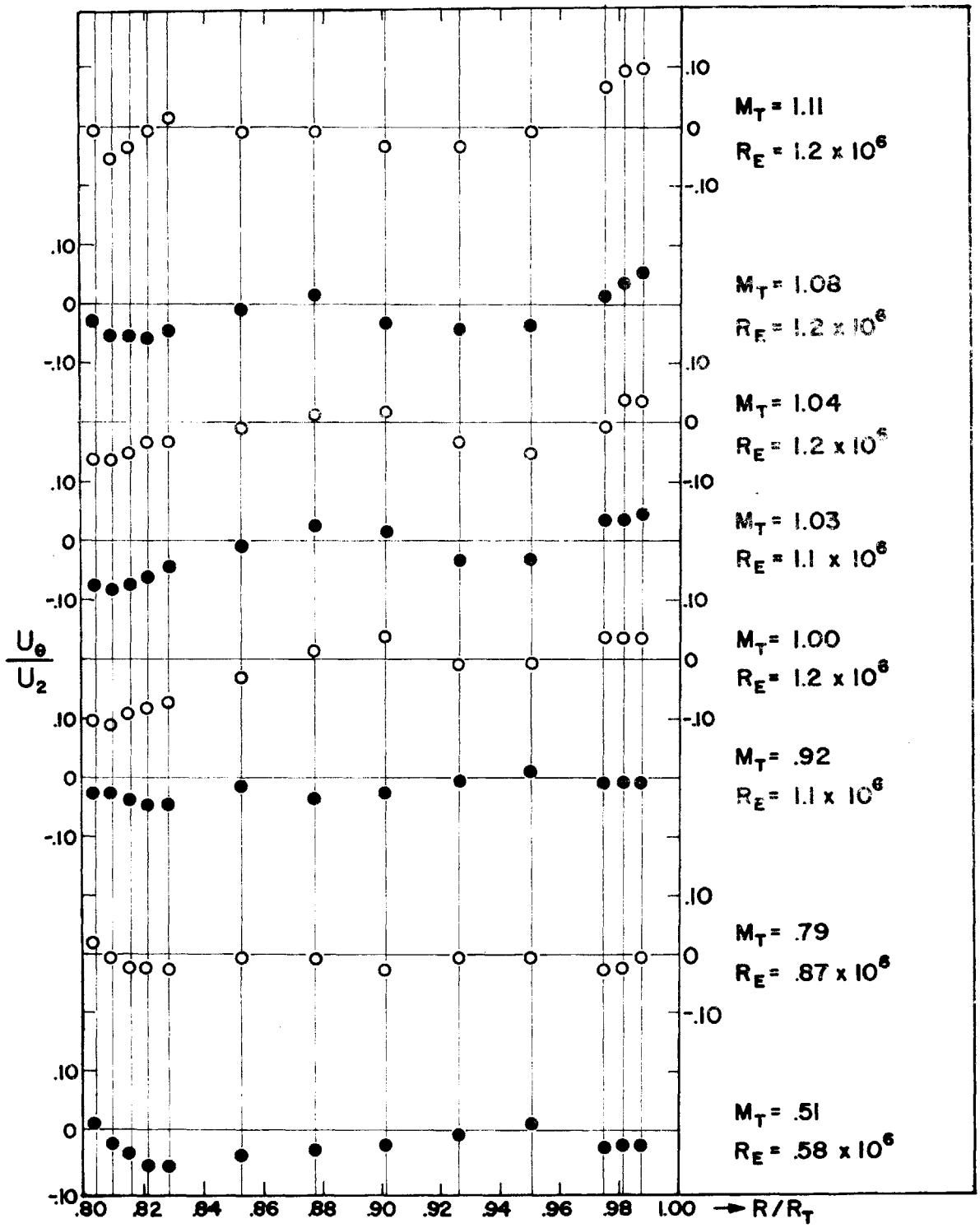

FIG. 15a: TANGENTIAL VELOCITY DISTRIBUTIONS

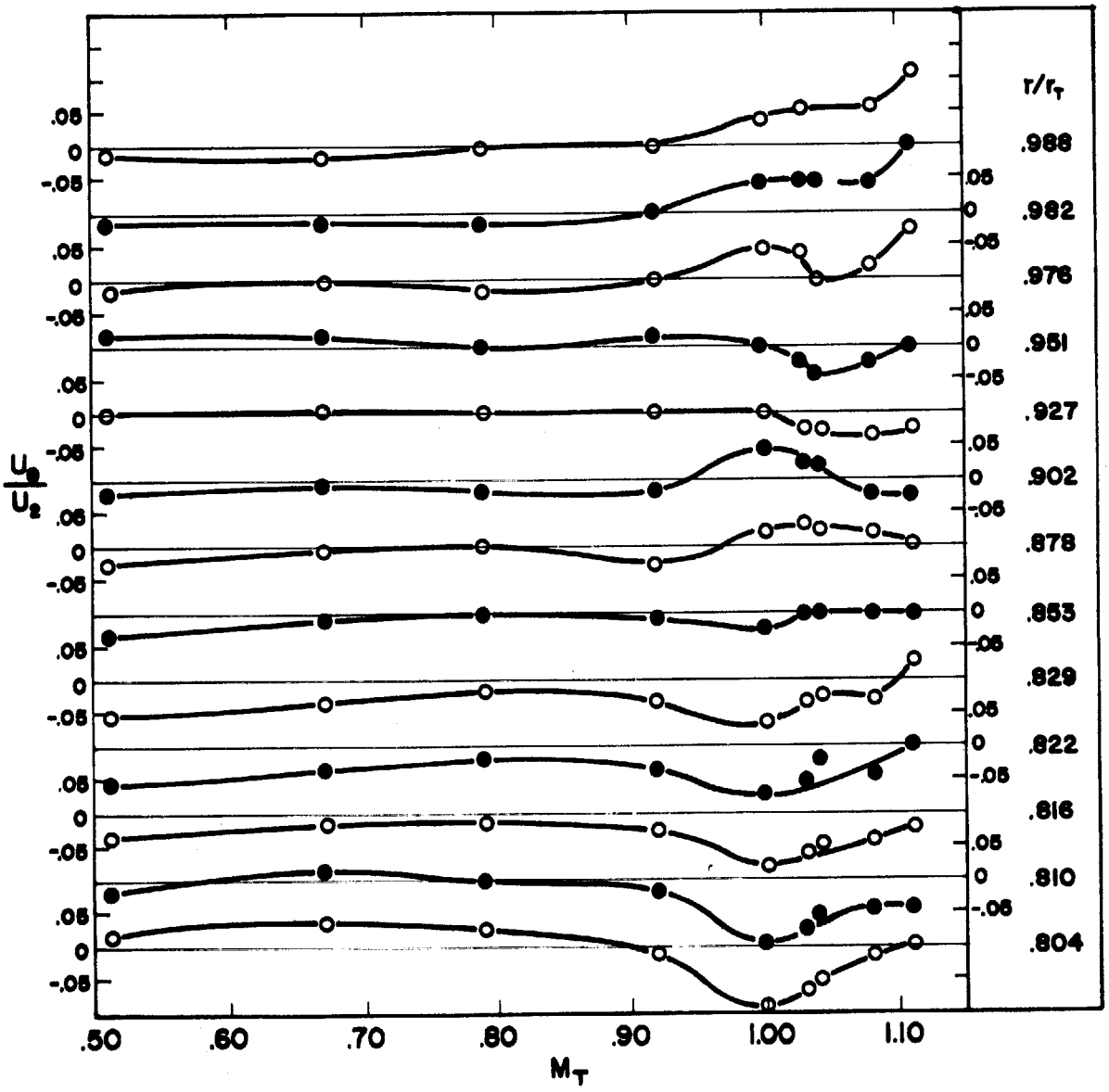

FIG. 15b: TANGENTIAL VELOCITY DISTRIBUTIONS

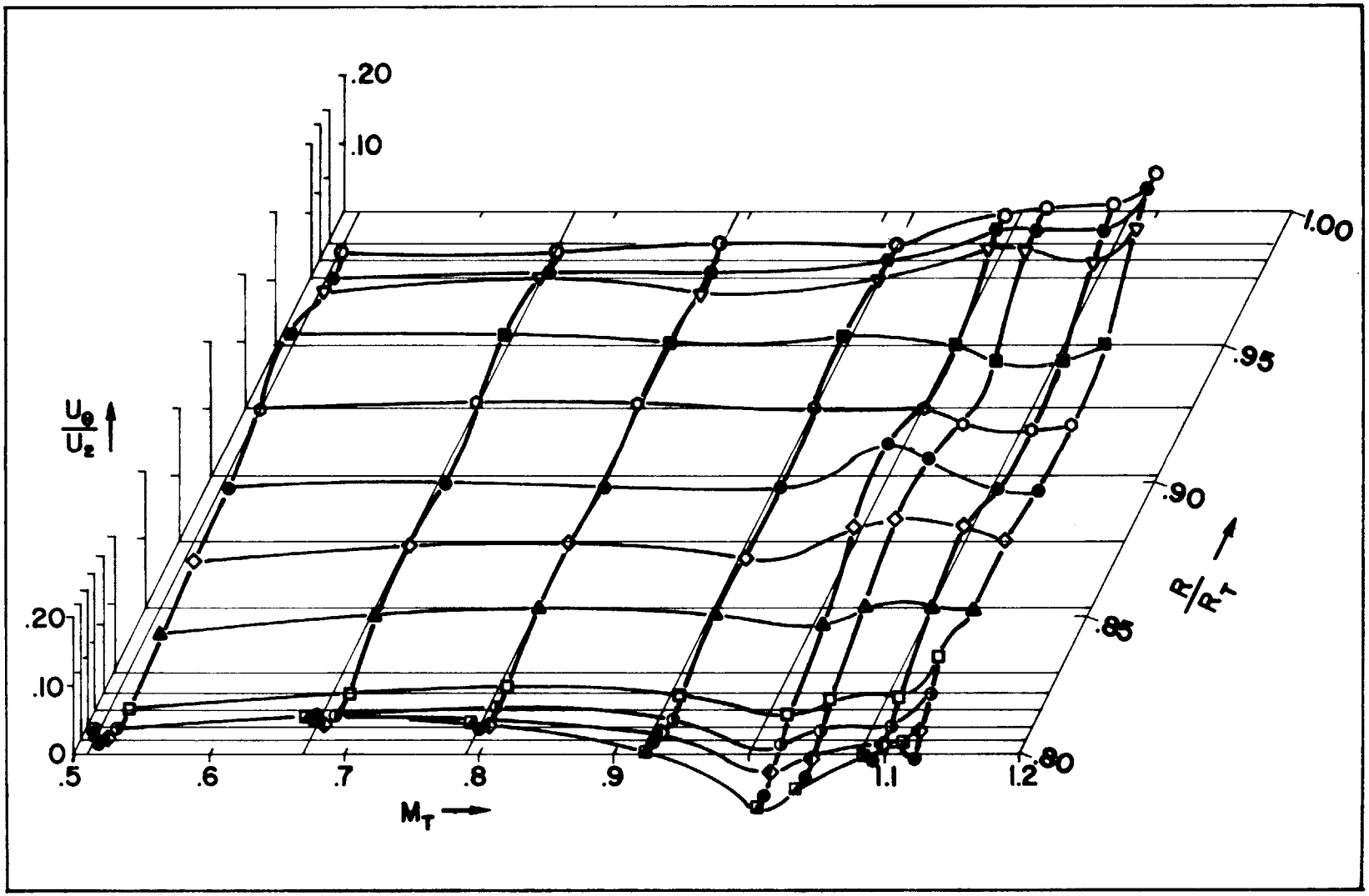

FIG. 15c: TANGENTIAL VELOCITY DISTRIBUTIONS

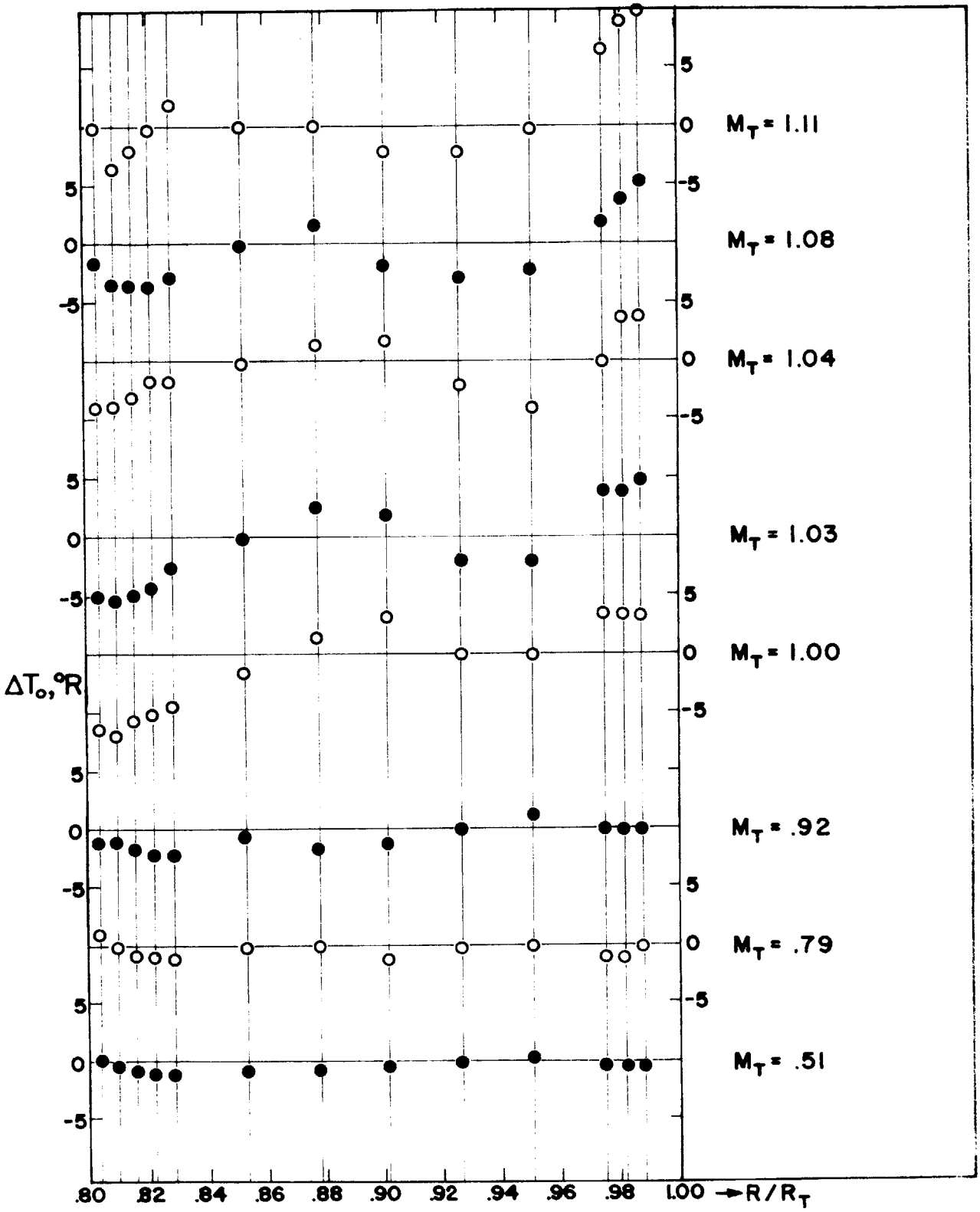

FIG. 16: TOTAL TEMPERATURE DISTRIBUTION AT STATION 3

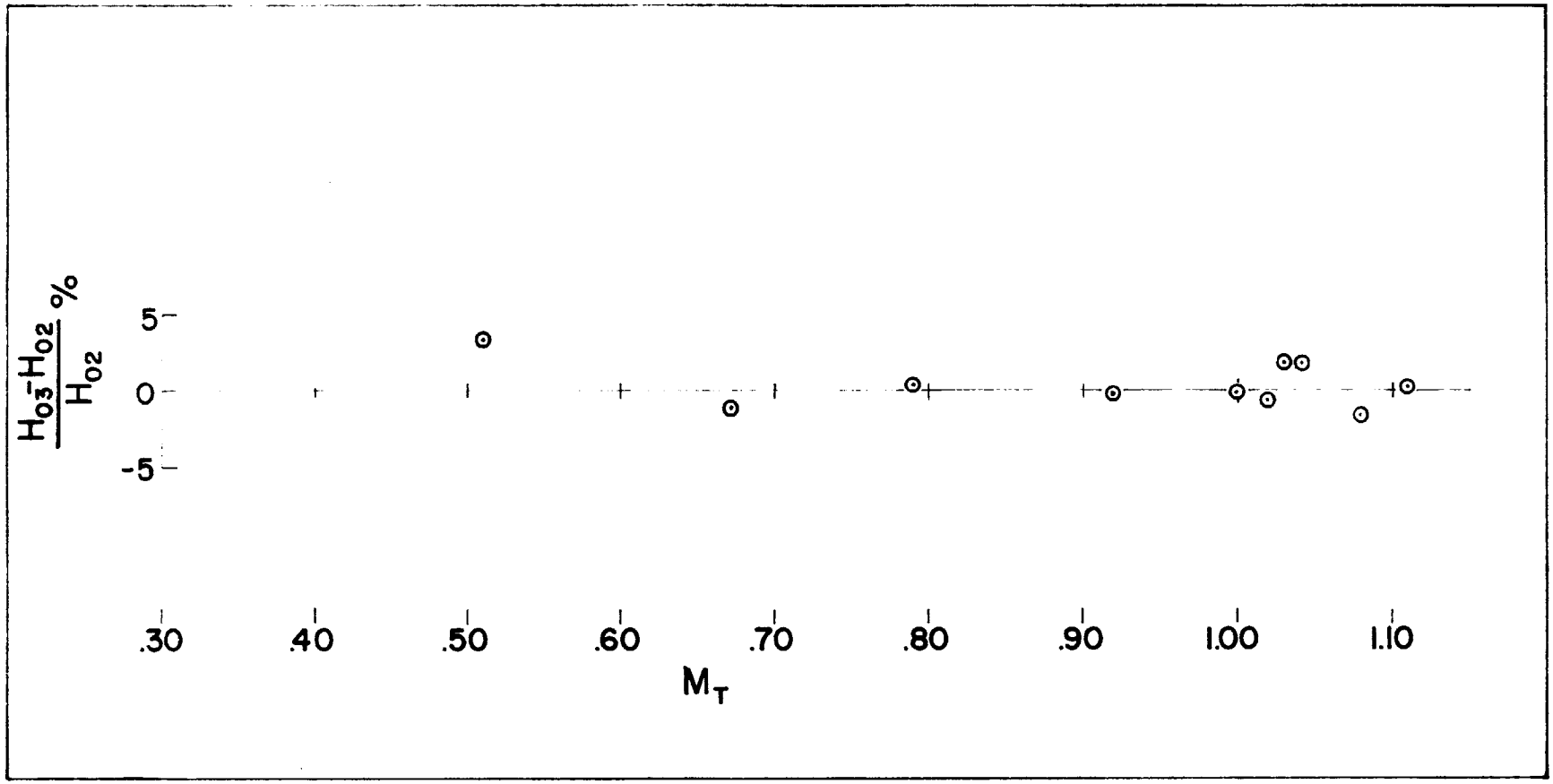

FIG. 17: STAGNATION ENTHALPY RISE ACROSS ROTOR

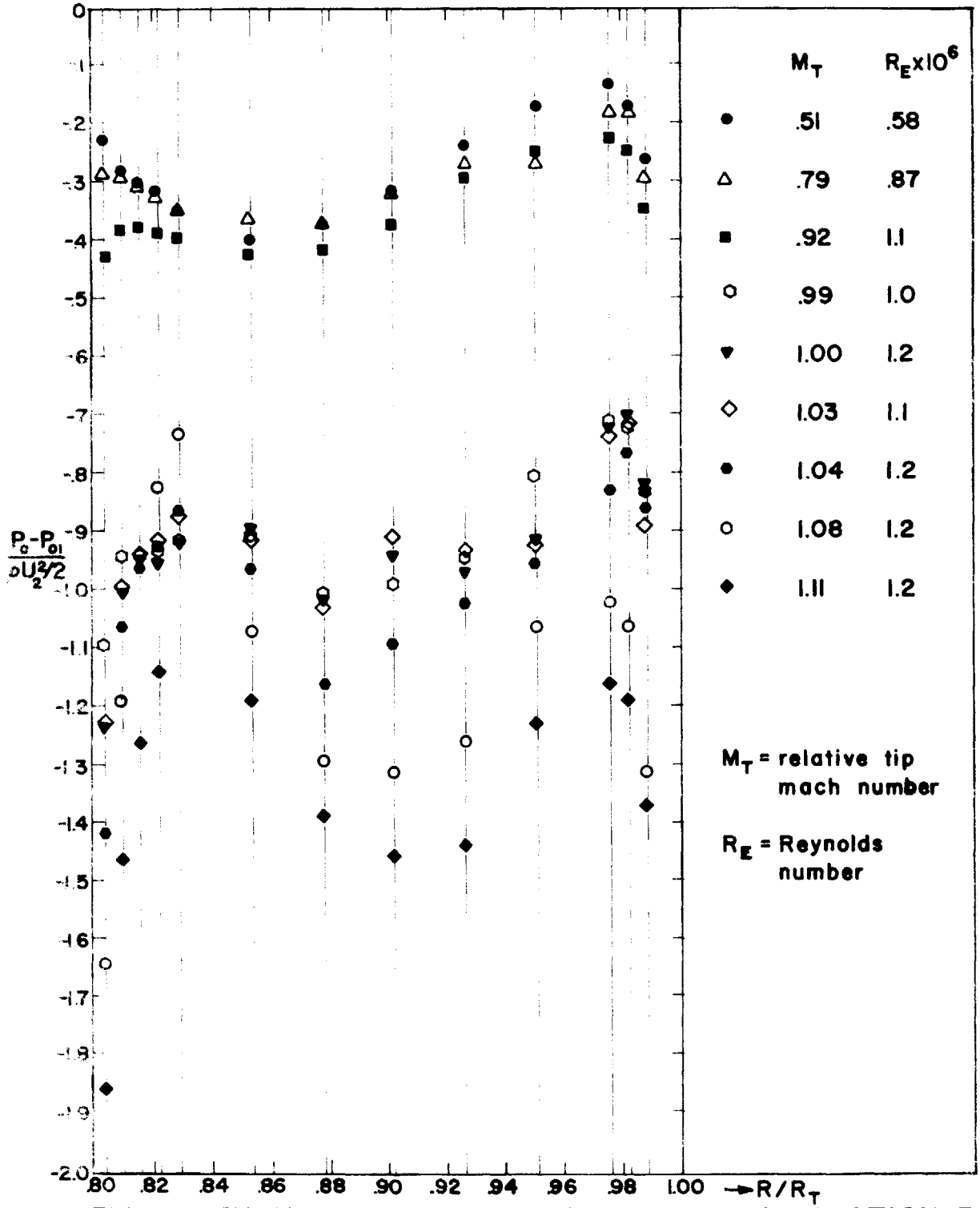

FIG. 18: TOTAL PRESSURE DISTRIBUTION AT STATION 3

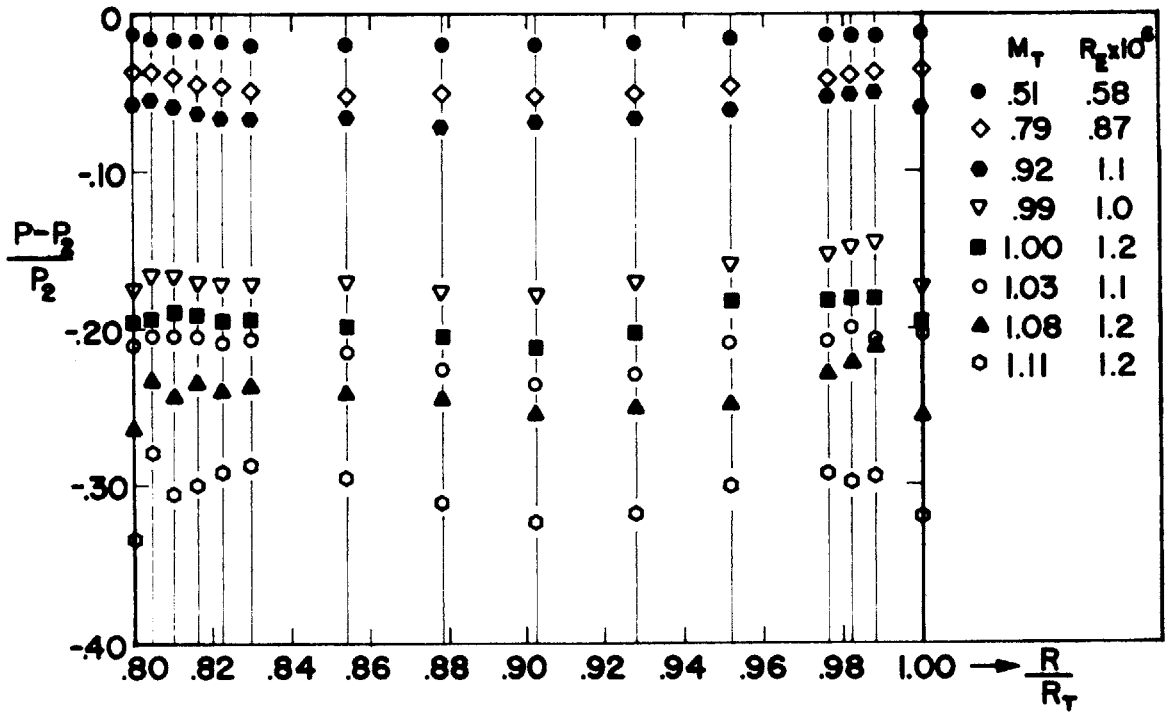

FIG. 19: STATIC PRESSURE DISTRIBUTION AT STATION 3

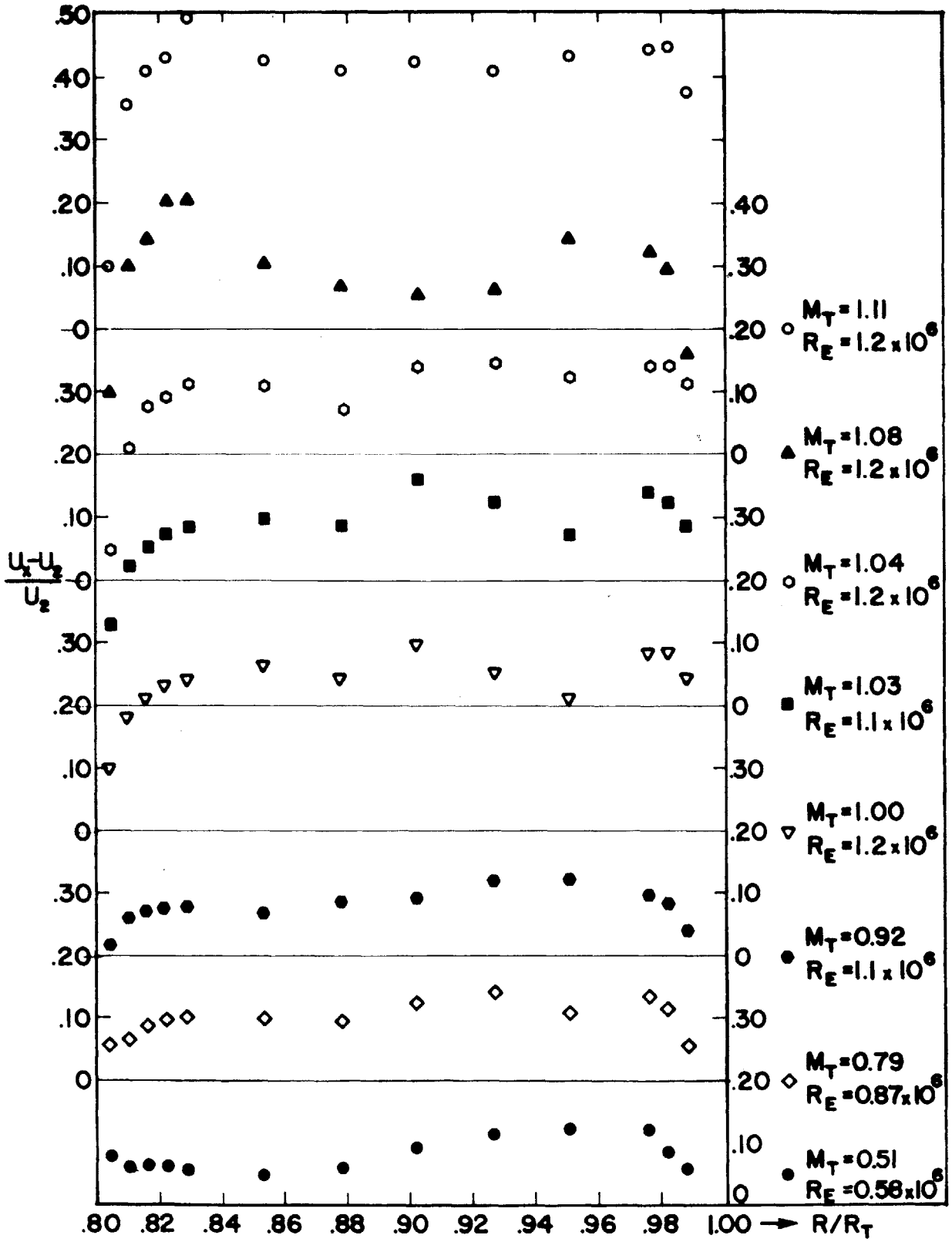

FIG. 20: AXIAL VELOCITY PROFILES AT STATION 3

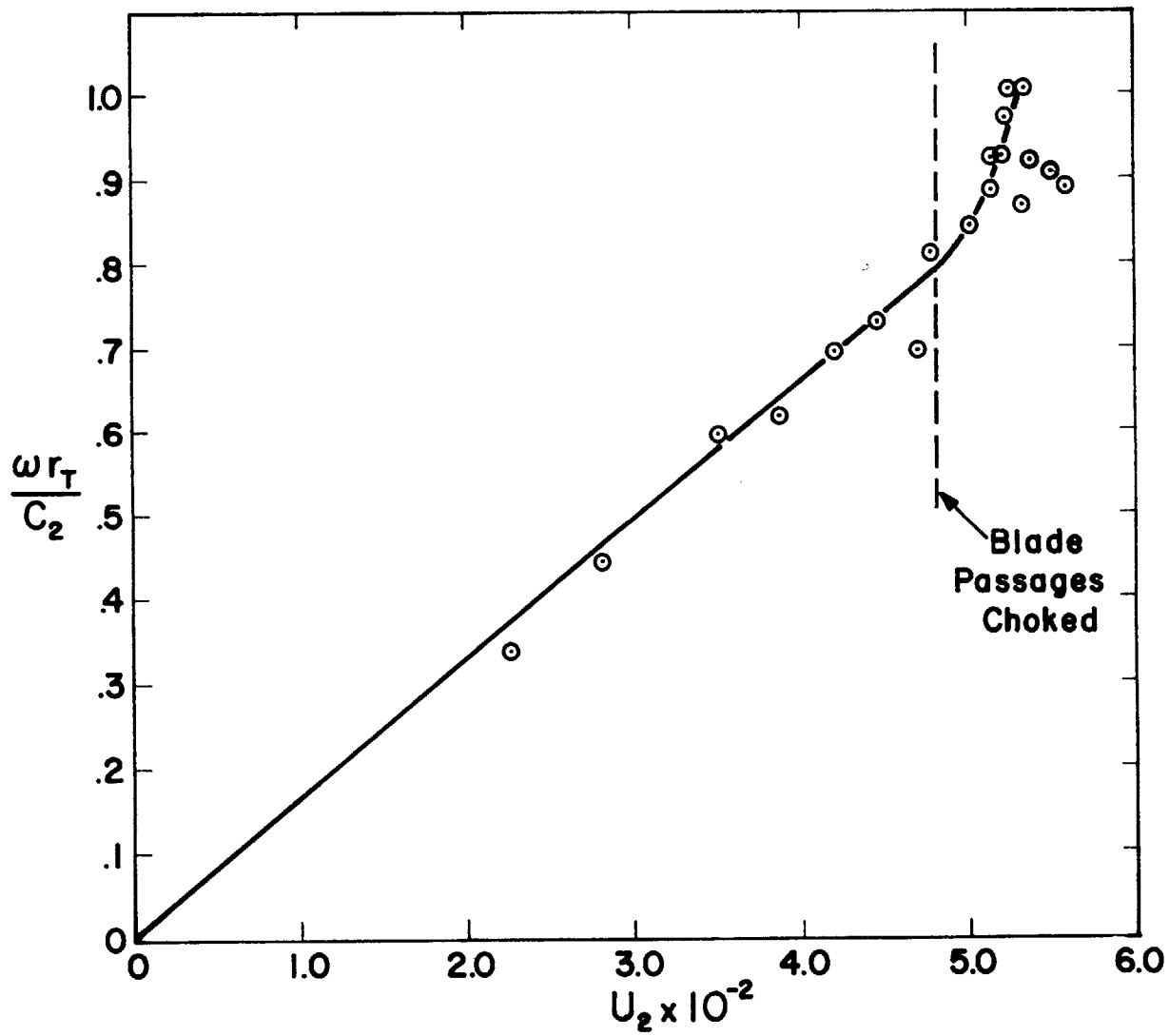

FIG. 21: VARIATION OF ROTOR TIP SPEED WITH INLET AIR AXIAL VELOCITY

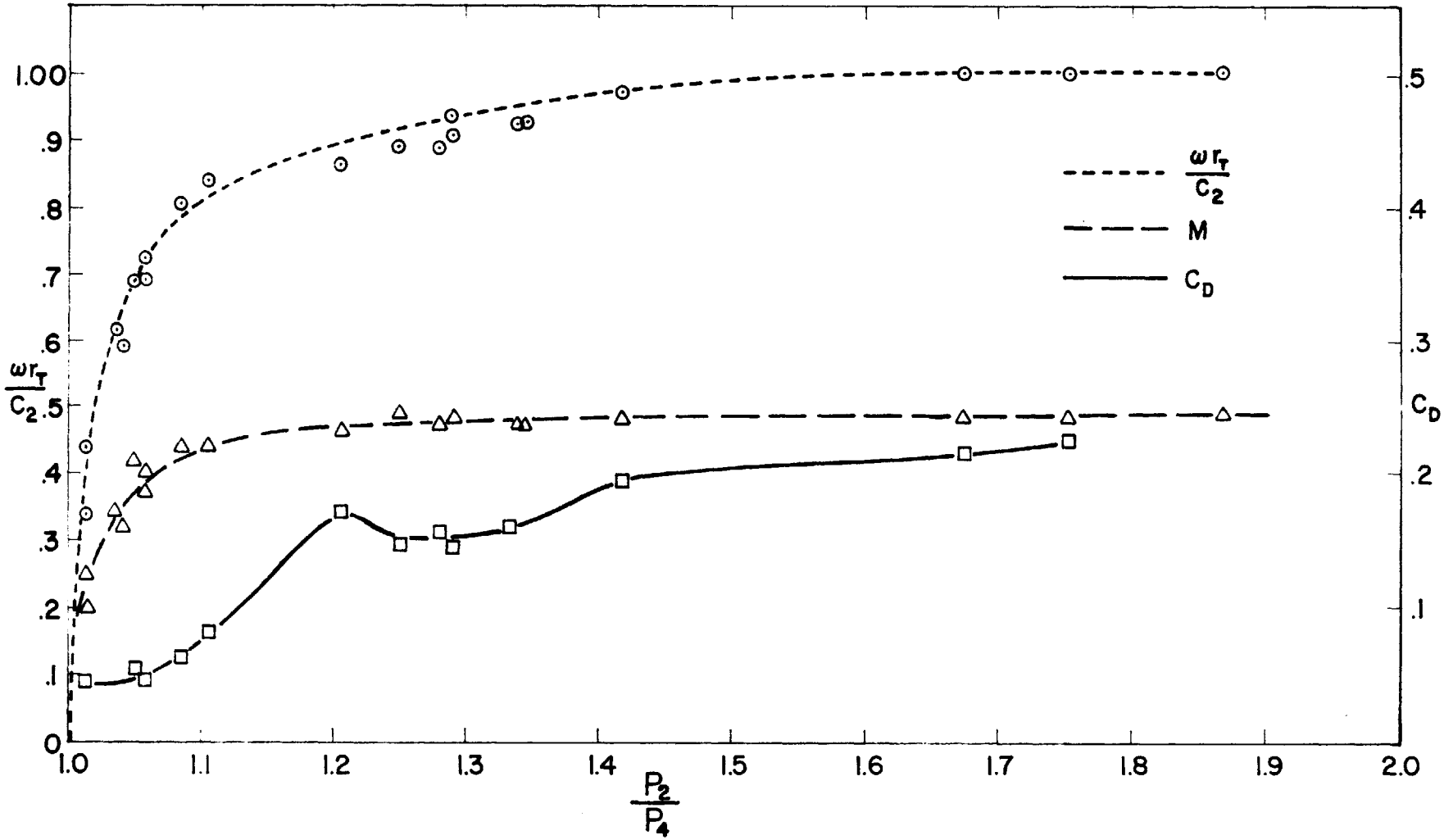

FIG. 22: ROTOR TIP SPEED, INLET MACH NUMBER AND DRAG COEFFICIENT VS. PRESSURE RATIO ACROSS ROTOR

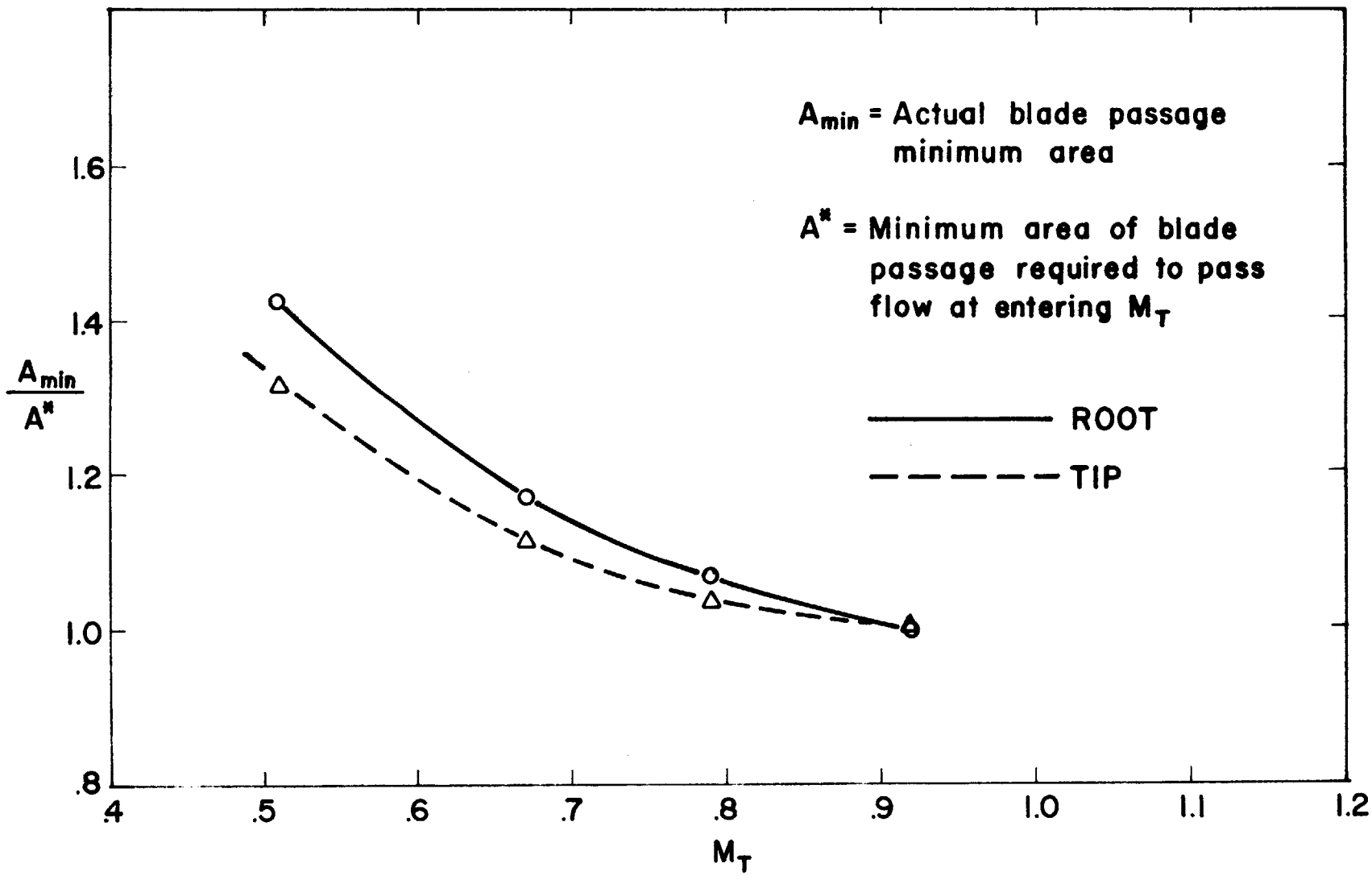

FIG. 23: BLADE PASSAGE AREA RATIO VS. TIP MACH NUMBER

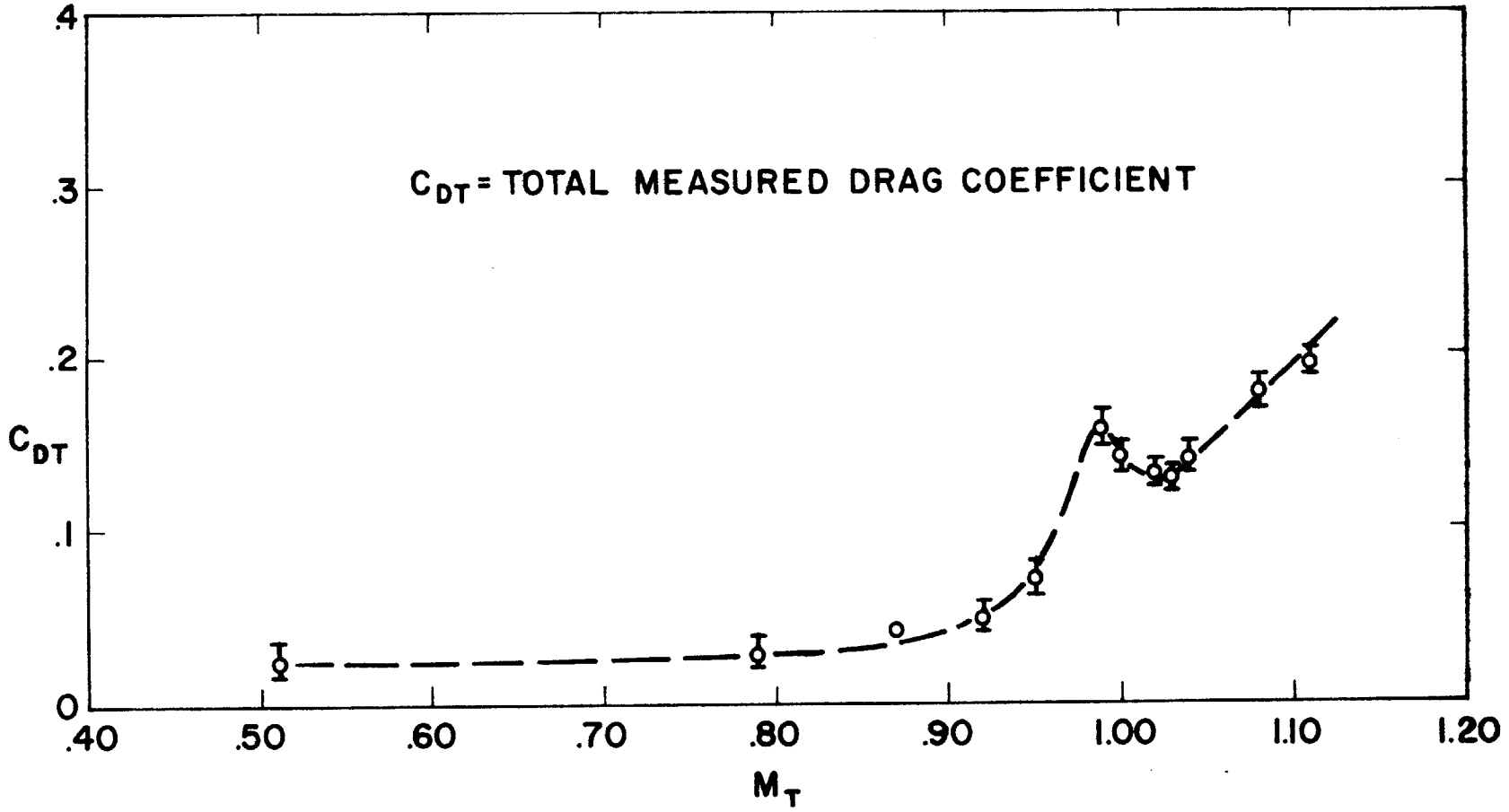

FIG. 24: TOTAL DRAG COEFFICIENT VS. TIP RELATIVE MACH NUMBER

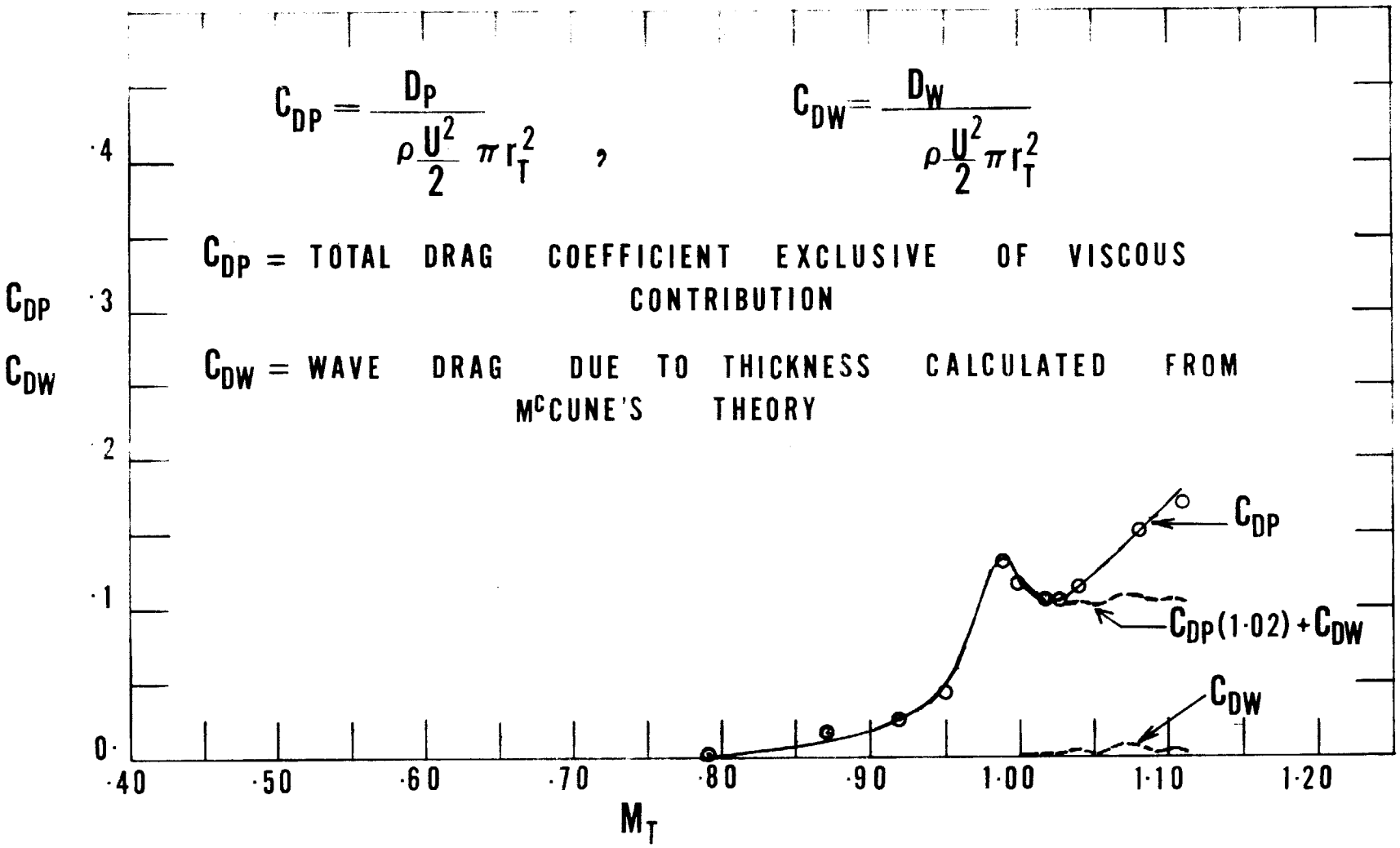

FIG. 25: PRESSURE DRAG COEFFICIENT VERSUS RELATIVE TIP MACH NUMBER.

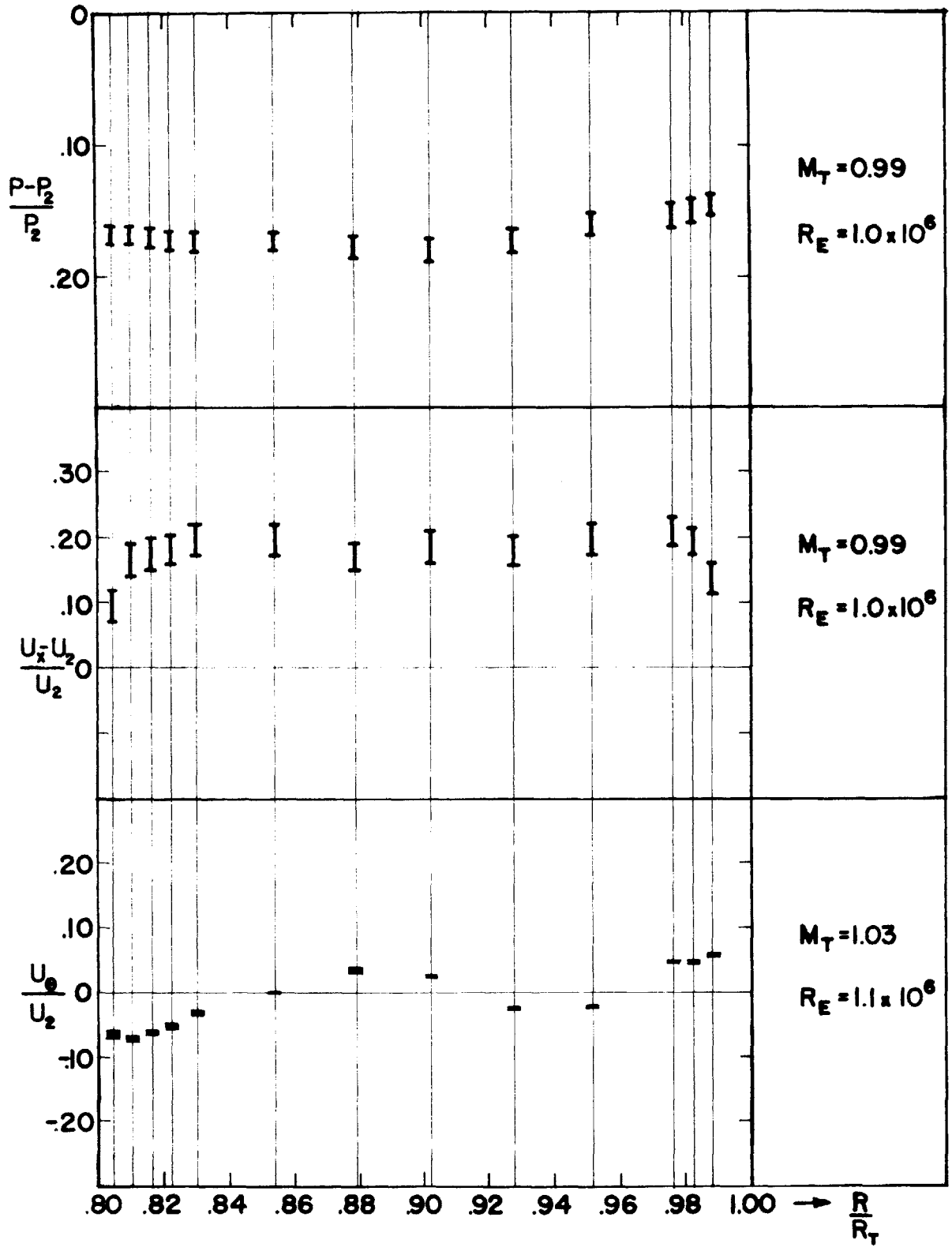

FIG. 26: POSSIBLE ERROR BOUNDS ON MEASURED PROFILES

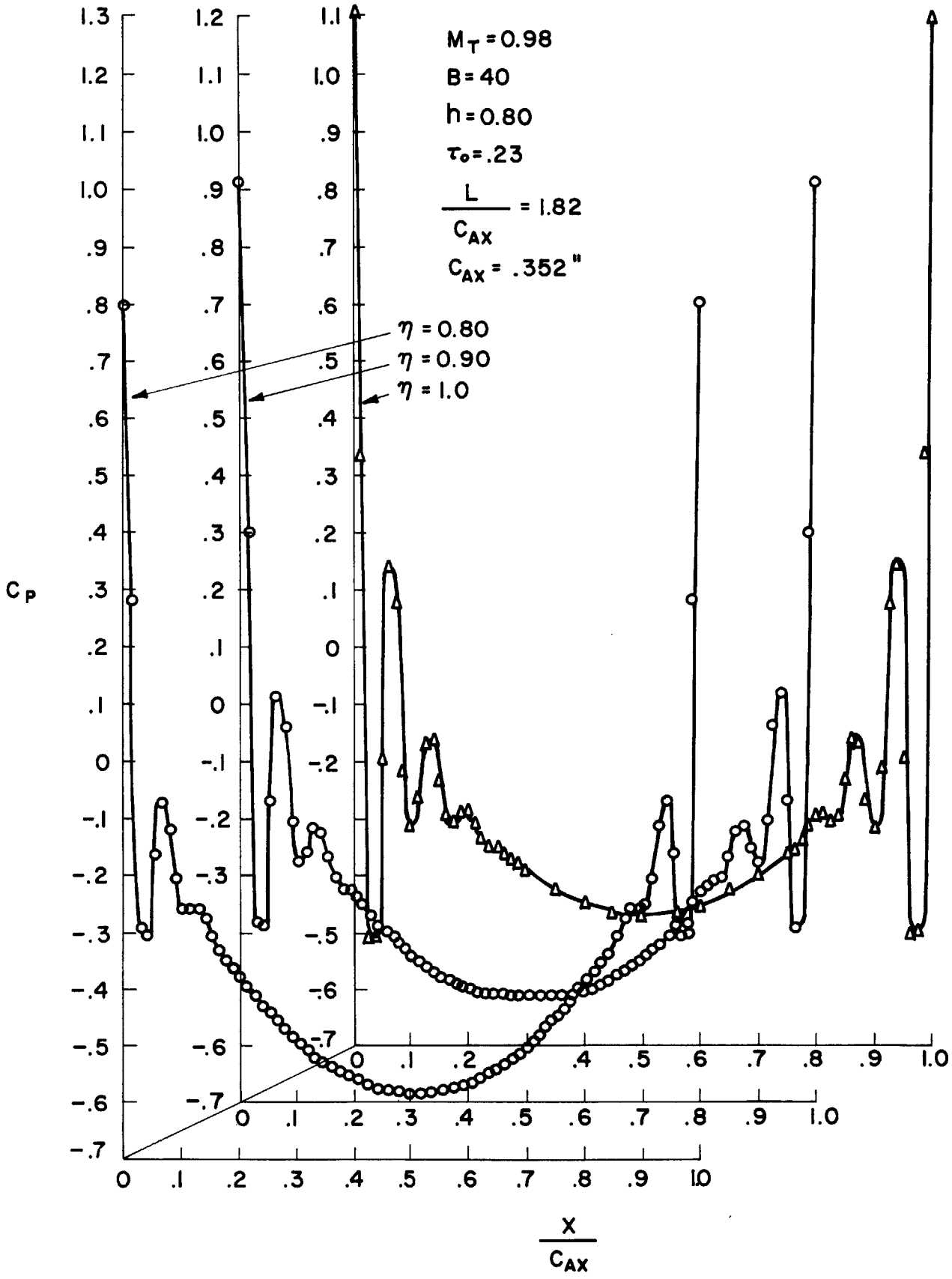

FIG. 27: TYPICAL SUBSONIC PRESSURE DISTRIBUTIONS

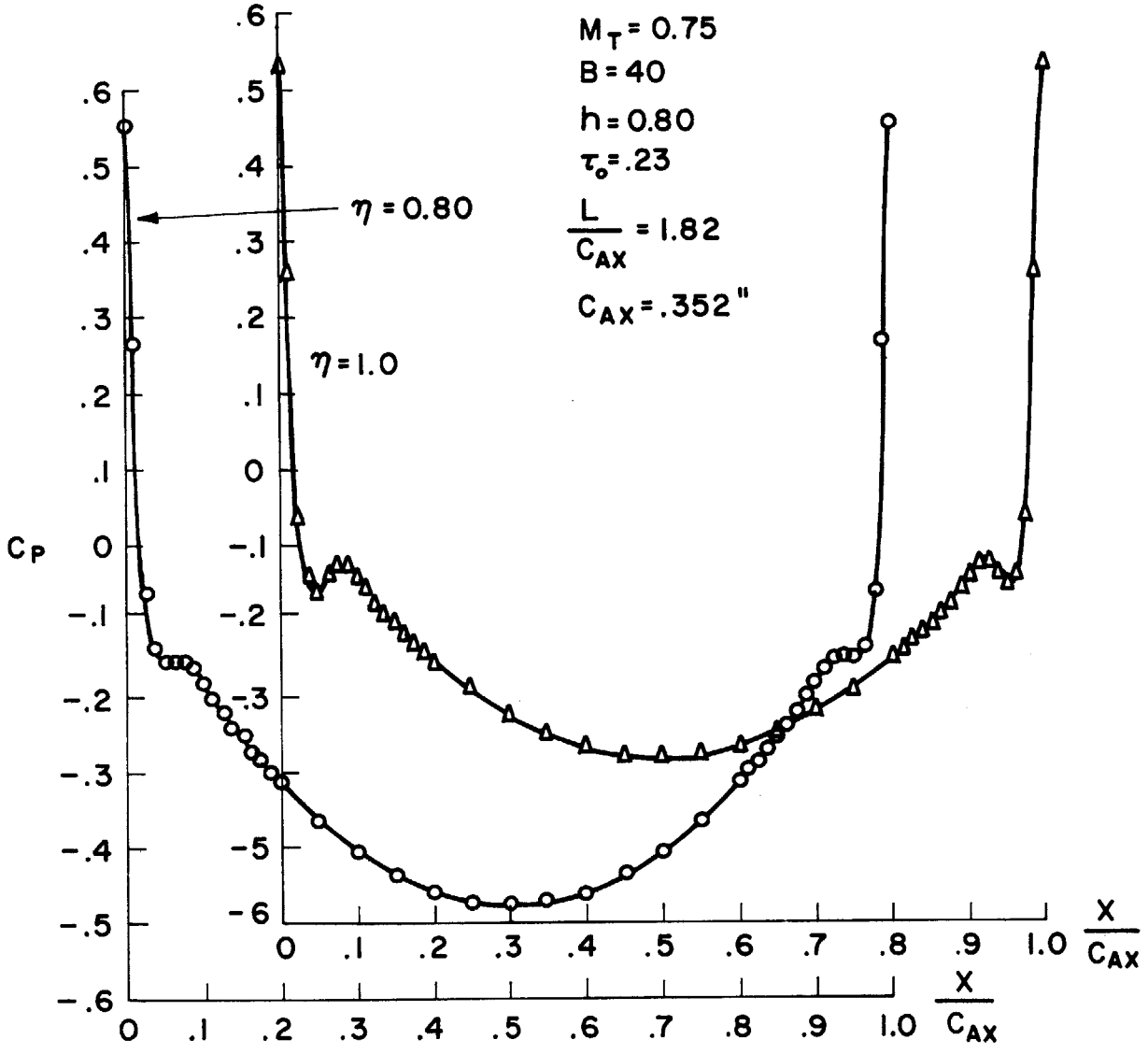

FIG. 28: PRESSURE DISTRIBUTION AT $M_T = .75$

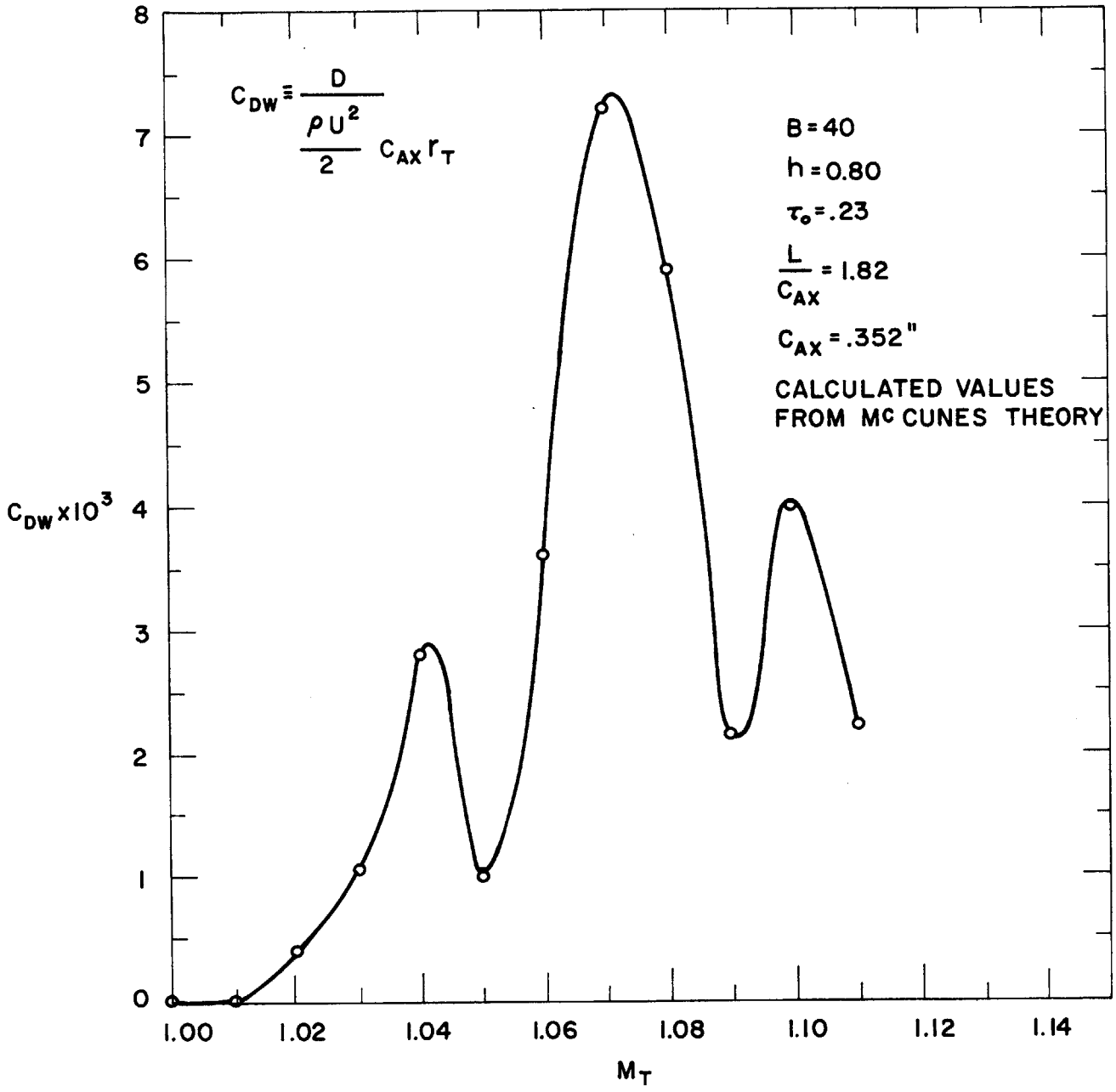

FIG. 29 : WAVE DRAG RISE WITH RELATIVE MACH NUMBER

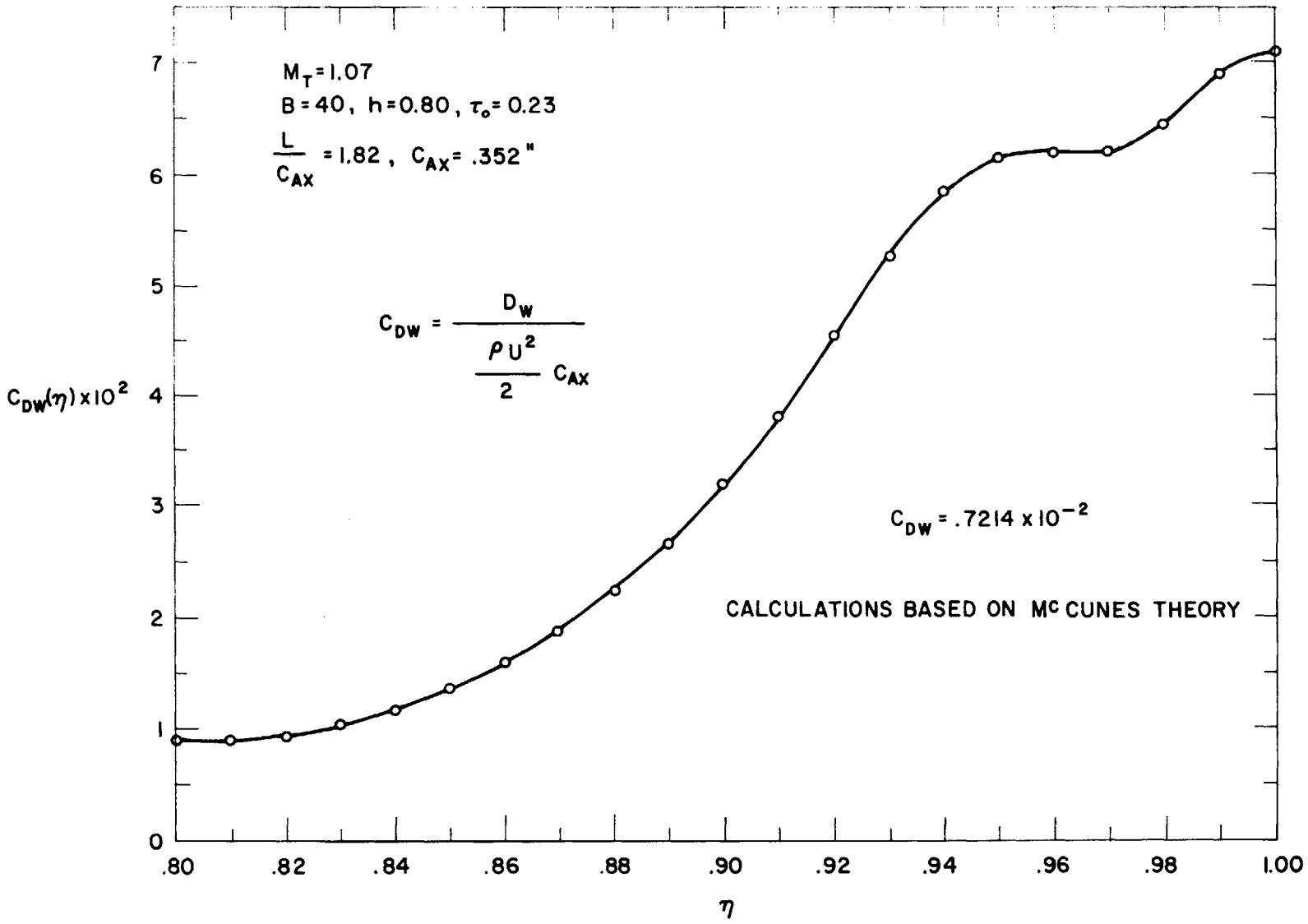

FIG. 30: RADIAL DISTRIBUTION OF C_{DW}

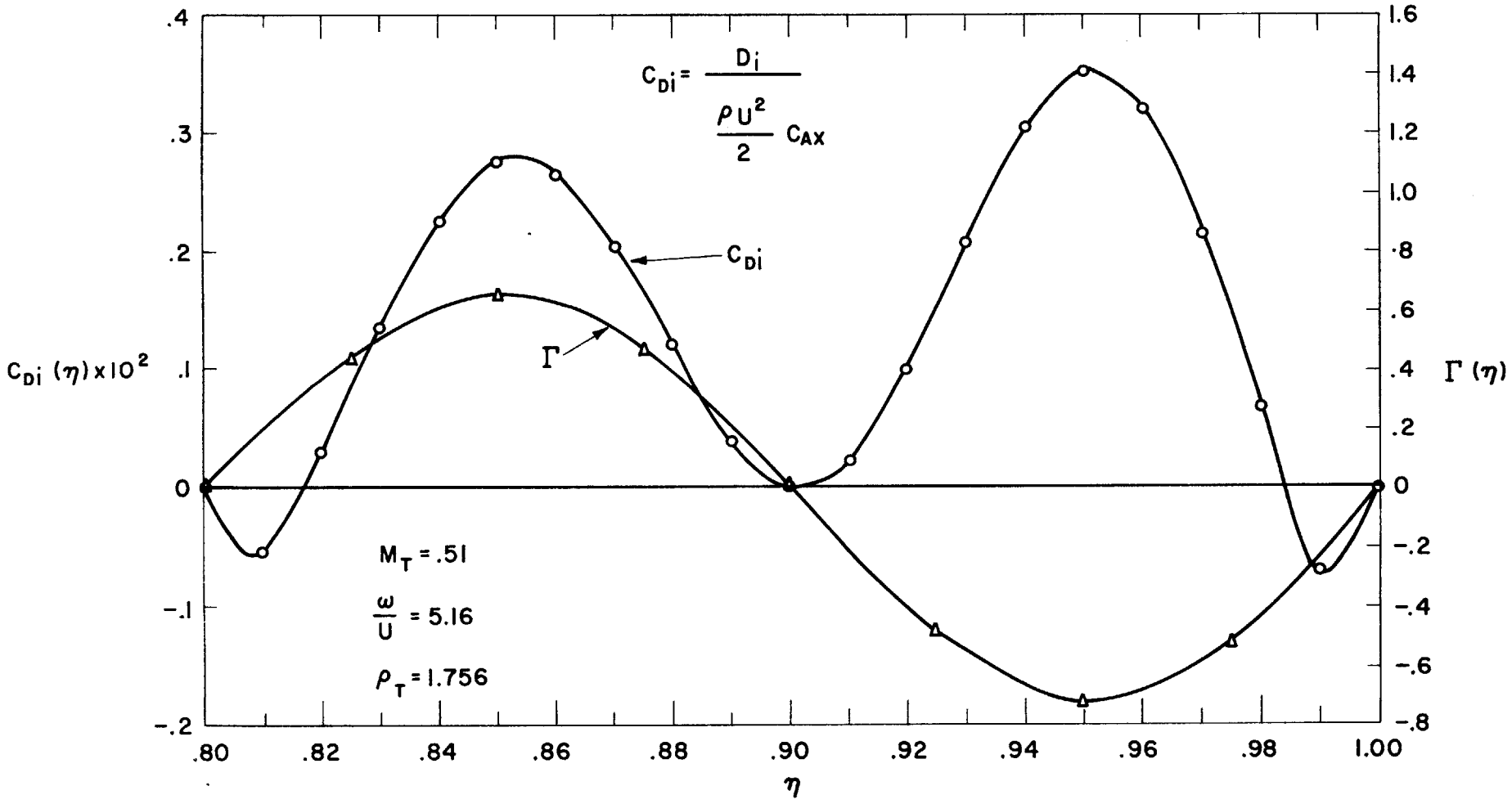

FIG. 31: RADIAL DISTRIBUTION OF C_{Di} DUE TO CIRCULATION Γ

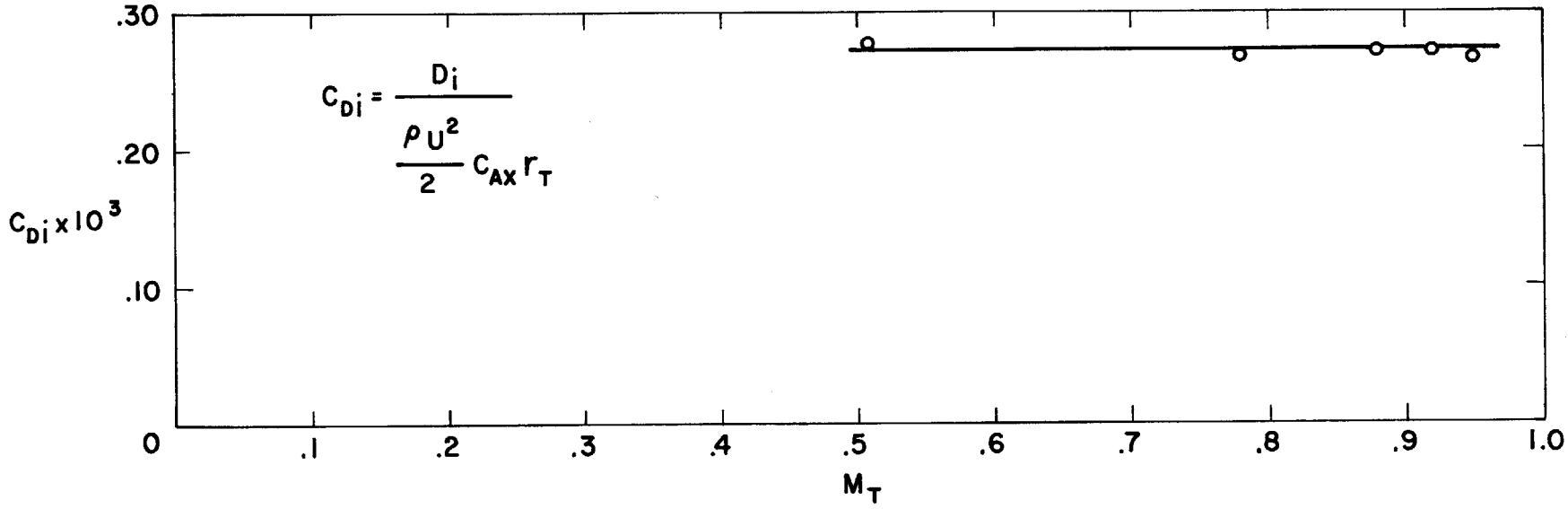

FIG. 32: DISTRIBUTION OF C_{Di} WITH M_T

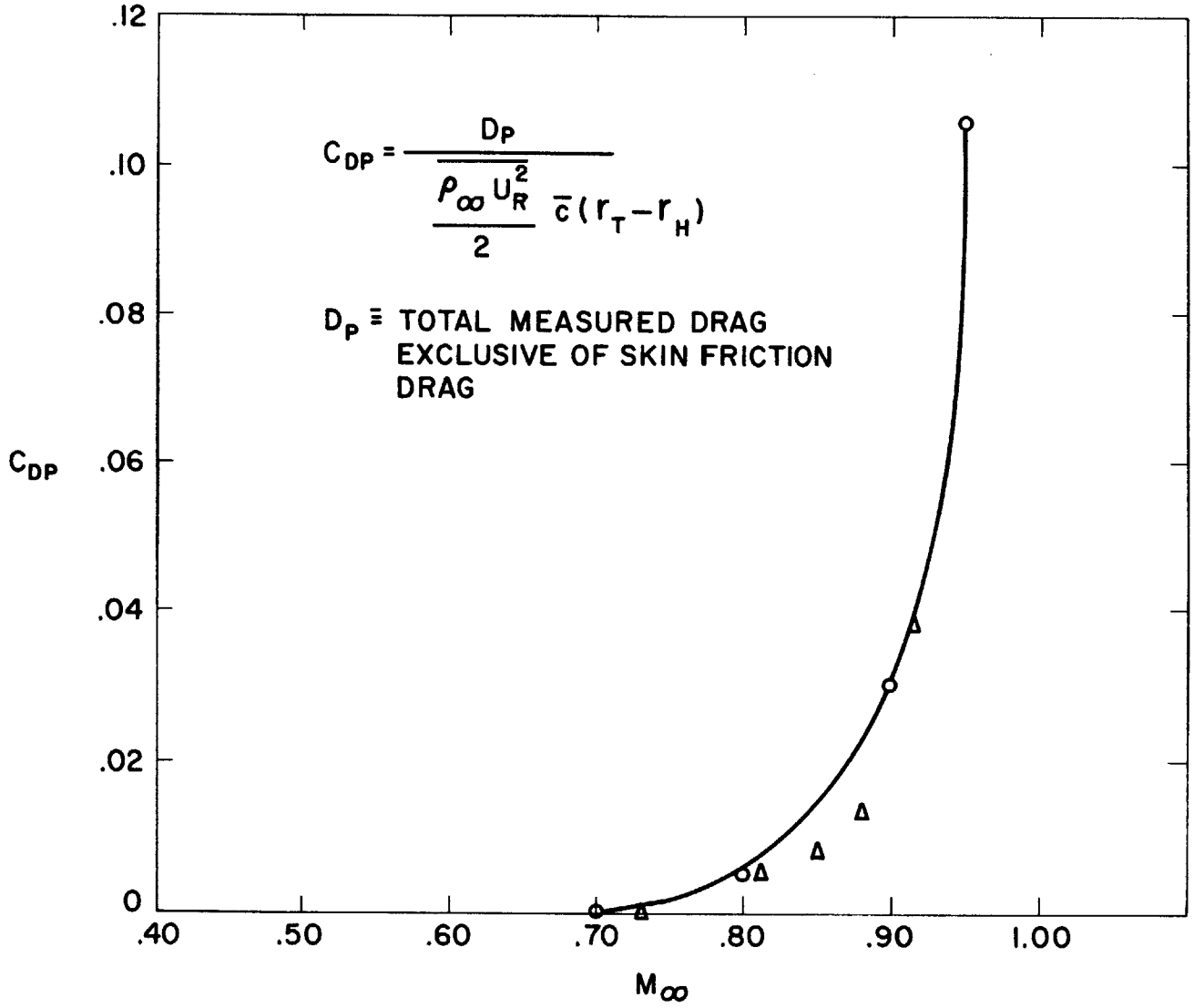

FIG. 33: SUBSONIC DRAG RISE COMPARED WITH BRYSON'S 2-D DATA